ELECTRON-PHONON INTERACTION IN TOPOLOGICAL MATERIALS

INAUGURAL-DISSERTATION

zur Erlangung des Doktorgrades
der Mathematisch-Naturwissenschaftlichen Fakultät
der Heinrich-Heine-Universität Düsseldorf

vorgelegt von

KATHRIN DORN
aus Neuss

Düsseldorf, Oktober 2021

aus dem Institut für Theoretische Physik, Lehrstuhl IV
der Heinrich-Heine-Universität Düsseldorf

Gedruckt mit der Genehmigung der
Mathematisch-Naturwissenschaftlichen Fakultät der
Heinrich-Heine-Universität Düsseldorf

Berichterstatter:

1. Prof. Dr. Reinhold Egger

2. Prof. Dr. Thomas Heinzel

Tag der mündlichen Prüfung: 07. Dezember 2021

Abstract

Topological phases opened a new field of research in condensed matter physics. Symmetries and topology that lead to states protected from disorder, thus defined new phases in materials. Within the scope of this work, the focus lies on topological insulators and Weyl semimetals. The topologically insulating phase can either follow from the quantum Hall effect, if time-reversal symmetry is broken, or spin-orbit coupling, if time-reversal symmetry is present. As a consequence, conducting surface states emerge. While topological insulators provide Dirac fermions, a Weyl semimetal has Weyl fermions that are chiral, massless particles. Weyl semimetals are topological semimetals with the Fermi energy residing at the Weyl nodes. The surface states form an arc connecting the projection of the nodes in the surface Brillouin zone. The splitting of the Weyl nodes happens due to a broken symmetry.

Within this thesis, the effects of electron-phonon interaction in nanowires made of topological insulators and Weyl semimetals are presented. The magnetic field is applied parallel to the axis of the topological insulator nanowire. A half-integer magnetic flux leads to a protected surface states. The topological insulator nanowire corresponds to a one dimensional system that allows for the approach of bosonization in order to describe interactions within the system. Electron-phonon interaction is described by deformation potential coupling in isotropic elastic continuum theory. Based on the bosonized Hamiltonian including electron-electron interactions, the effect of both interactions on the conductivity is determined by the Kubo formula. Furthermore, a zero temperature phase diagram is derived and the Boltzmann equation is used to determine the effects of electron-phonon scattering in absence of electron-electron interaction.

The Weyl semimetal band structure shows conducting surface and bulk states at the same time. In the context of this thesis, the dependence of the dispersion of a Weyl semimetal nanowire on the boundary condition and the magnetic flux parallel to the axis is studied. The boundary condition includes a parameterizing angle that preserves momentum conservation. The focus lies on the magnetoresistivity that follows from the semiclassical Boltzmann approach involving electron-phonon coupling via the deformation potential. The bands provide different shapes and intersect the Fermi energy either with one or two pairs of Fermi points. This leads to the possibility of more scattering processes and also an increase of the resistivity. Furthermore, these different bands provide interesting features regarding the zero temperature conductance and the phonon-induced resistivity.

Zusammenfassung

Topologische Phasen haben ein neues Forschungsfeld im Bereich den kondensierten Materie eröffnet. Symmetrien und Topologie, die zu geschützen Zuständen vor Störungen führen, definierten folglich neue Phasen in Materialien. Im Rahmen dieser Arbeit liegt der Fokus auf topologischen Isolatoren und Weyl Halbmetallen. Die topologische isolierende Phase kann entweder aus dem Quanten Hall Effekt folgen, wenn die Zeitumkehrinvarianz gebrochen ist, oder durch Spin-Bahn-Kopplung, wenn Zeitumkehrinvarianz präsent ist. Die Folge dessen ist das Entstehen von leitfähigen Oberflächenzuständen. Während topologische Isolatoren Dirac Fermionen haben, besitzt ein Weyl Halbmetall Weyl Fermionen, welche chirale, masselose Teilchen sind. Weyl Halbmetalle sind topologische Halbmetalle, die eine Fermi Energie auf Höhe der Weyl-Knoten besitzen. Die Oberflächenzustände formen einen Bogen, der die Projektion der Weyl-Knoten in der Oberflächenbrillouinzone verbindet. Die Teilung in zwei Weyl-Knoten geschieht durch eine gebrochene Symmetrie. In dieser Arbeit, werden die Effekte von Elektron-Phonon Wechselwirkung in Nanodrähten aus topologischen Isolatoren und Weyl Halbmetallen vorgestellt. Das Magnetfeld ist parallel zur Achse des topologischen isolierenden Nanodrahts angelegt. Ein halbzahliger magnetischer Fluss führt zu geschützen Oberflächenzuständen. Der topologische isolierende Nanodraht kann als ein eindimensionales System betrachtet werden und erlaubt die Anwendung von Bosonisierung, mittels derer die Wechselwirkungen beschrieben werden können. Elektron-Phonon Wechselwirkung wird durch die Kopplung über ein Deformationspotential in elastischer isotroper Kontinuumstheorie beschrieben. Basierend auf dem bosonisierten Hamiltonian, der Elektron-Elektron Wechselwirkungen beinhaltet, werden die Effekte beider Wechselwirkungen auf die spezifische Leitfähigkeit mithilfe der Kubo-Formel bestimmt. Zusätzlich wird ein Phasendiagramm aufgestellt und die Boltzmann-Gleichung wird zur Bestimmung der Auswirkung von Elektron-Phonon Streuung in Abwesenheit von Elektron-Elektron Wechselwirkung verwendet.

In Weyl Halbmetallen zeigt die Bandstruktur gleichzeitig leitende Oberflächen- und Bulkzustände. Im Kontext dieser Arbeit wird die Abhängigkeit der Dispersion eines Weyl Halbmetall Nanodrahtes von der Randbedingung und dem magnetischen Fluss parallel zur Achse untersucht. Die Randbedingung beinhaltet einen parametrisierenden Winkel, der den Impuls erhält. Der Fokus liegt dabei beim magnetoresistiven Effekt, der aus dem semiklassichen Boltzmann-Ansatz folgt und Elektron-Phonon-Kopplung über das Derformationspotential berücksichtigt. Die Bänder besitzen verschiedene Formen und schneiden die Fermi Energie entweder mit einem oder an zwei Paaren an Fermi Punkten. Das führt zum möglichen Auftreten mehrerer Streuungsprozesse und ebenso zu einem Anstieg des spezifischen Widerstands. Darüber hinaus zeigen die verschiedenen Bänder interessante Merkmale bezüglich der Leitähigkeit bei Temperaturen bei Null und dem Phonon-induzierten spezifischen Widerstand.

Contents

Chapter 1

Introduction

The experimental investigation of topological insulators by König *et al.* has opened a whole new field of interest [1]. As the name reveals, these materials possess topological properties and, therefore, lead to characteristic features like, for instance, the existence of topologically protected surface states.

The formulation of a relativistic, spinful particle by Paul Dirac [2] in 1928, gave a base for further theoretical investigation of particles in quantum mechanics. Only one year later Hermann Weyl [3] proposed the Weyl fermion by splitting the massless Dirac equation into the eigenstates of the chirality operator. While the Dirac fermion is a non chiral particle, splitting the Dirac cone into two cones of each chirality results in a Weyl fermion. The particularity of the Weyl fermion is given by the construction of a pair of cones with opposite chirality.

The following 70 years, studies on the Quantum Hall Effect by v.Klitzing *et al.* [4] and Thouless *et al.* [5] showed the increase of conductance in steps of conductance quanta at low temperatures. This led to the definition of topological invariants. Moreover, Kane and Mele predicted topological invariant systems with gapless surface states [6–8]. First, the two dimensional topological insulator (2DTI) was experimentally shown in HgTe quantum wells [1,9]. Then, the three dimensional topological insulator (3DTI) was discovered experimentally in $\mathrm{Bi}_{1-x}\mathrm{Sb}_x$ by the group of Hsieh *et al.* [10]. In ARPES[1] measurements they showed that this topological material has a conducting surface state and gapped bulk states. Its gapless surface state is protected by inversion- and time-reversal symmetry [11]. Furthermore, they observed Dirac particles forming the surface states. Unlike $\mathrm{Bi}_{1-x}\mathrm{Sb}_x$ where band inversion occurs for more than one band, the second generation of 3DTI, $\mathrm{Bi}_2\mathrm{Se}_3$ and $\mathrm{Bi}_2\mathrm{Te}_3$, even shows a single Dirac cone and has a large band gap [12]. Based on the existence of a topological insulator with Dirac fermions, first predictions for topological semimetals were made. The proposed materials needed a broken symmetry and the Fermi energy had to lie within the Fermi surface close to the band touching points. Burkov and Balents suggested a multilayer heterostructure of topological and ordinary insulators [13]. In 2015, the Princeton and the IOP groups discovered the Weyl semimetal TaAs [14–18]. Instead of a surface state within a single point, the two Weyl cones impose a segment of such surface state points. This alignment of surface states connects the projection of the Weyl nodes the surface Brillouin zone resulting in a Fermi surface arc. However, the Fermi arc is no longer protected by inversion- and time-reversal symmetry, as one of these symmetries needs to be broken in order to obtain Weyl fermions. Other consequences of symmetry breaking in Weyl semimetal are the chiral anomaly and the

---

[1] angle-resolved photoemission spectroscopy

Quantum Anomalous Hall Effect, which are discussed further in chapter 2.

The experimental evidence that topological states in such materials exist opened a rich field of research. In the context of this thesis, transport properties of topological insulators and Weyl semimetals in nanowire geometry are discussed which are of large interest in theoretical and experimental studies. An important feature of the nanowire-geometry in topological insulators is that a half-integer flux piercing the wire closes the gap of the lowest band [19]. Experimental and theoretical investigation showed Aharonov-Bohm oscillations of conductance with a period of flux quanta [20–23]. In Weyl semimetals, the surface states impose a Fermi arc confined by the Weyl nodes. While the existence of Weyl fermions in several materials was already known, topological Fermi arcs were discovered recently in TaAs. Their contribution to conductance has been investigated in nanowire geometry by Kaladzhyan *et al.* for surface states with a flat Fermi arc [24–26].

The consequences of electron-phonon interactions have been studied for many geometries and materials, for instance topological insulators in half-space and thin-film geometry [27, 28]. Moreover, although electron-electron interactions can increase the resistivity of a system, attractive phonon interaction can provide instabilities leading to a superconducting phase [29, 30]. The nanowire-geometry will be of large interest in this thesis since transport measurements have already shown interesting features in 3DTI nanowires that are discussed in chapter 3 [20, 21]. The geometry of a nanowire allows the system to be treated one-dimensional. Furthermore, one-dimensional systems with Dirac fermions can be described by Luttinger Liquids. The bosonization approach is a useful method to study complicated, one dimensional systems [31, 32]. Given a half-integer magnetic flux, the zero-temperature phase diagram presents order fluctuations of density waves. Away from half-integer flux, the Boltzmann approach shows, that phonon interaction provides backscattering which leads to an increase of temperature and resistivity [30, 33, 34].

In contrast to topological insulators, Weyl semimetals have a pair of cones, whose surface states form a Fermi arc. It is shown, that the choice of boundary conditions has a huge impact on the curvature of the arc [35]. The transport in Weyl semimetals is of large interest, since transport measurements have been recently studied experimentally [36, 37]. In contrast to a topological insulator nanowire, where only one band intersects the Fermi energy at one point, a Weyl semimetal can have more than only one band intersecting the Fermi energy under the same conditions. This leads to interesting features in the conductance and also in case the scattering of phonons is present. Chapter 4 presents a Weyl semimetal nanowire setup on a substrate with a magnetic flux piercing the nanowire. The focus is set on phonon-induced backscattering effects within a disorder free Weyl semimetal nanowire. Since transport in Weyl semimetal nanowires depends on the rich band structure, chapter 4 discusses the conductance at zero temperature and the corresponding effects of phonons on the magnetoresistivity.

Further, this thesis focuses on these two topological materials and examines how the differences of their topological nature affect the devices of nanowire geometry at low energy. Moreover, the effects of nonzero temperature appear in different ways and are studied according to the topological material. Chapter 5 gives a summary over this work about Dirac and Weyl fermions and their interactions in topological insulators and Weyl semimetals. These results are mapped to current topics with an outlook for future work.

If not mentioned otherwise, the constants are set $\hbar = c = e = k_B = 1$.

Chapter 2

Fundamental Principles

This chapter introduces the fundamentals on Dirac and Weyl fermions and their appearance in topological materials. These are necessary to understand the effects of interactions that are discussed in chapters 3-4. At the beginning, Dirac and Weyl fermions are introduced which are both solutions from the Dirac equation following from different conditions [2, 3]. The fermions follow from the topology of the materials they occur in. Dirac fermions appear as surface states in three dimensional topological insulators (TI) whose interesting physics will be discussed further in Sec.2.3. In order to understand the appearance of Dirac fermions, the fundamentals of TIs have to be established. Therefore, the band structure following from their topological properties has to be discussed. TIs define themselves by their topologically protected surface states. The topological invariance can for instance follow from the Quantum Hall (QH) effect. In a two dimensional system, a perpendicular external magnetic field can be responsible for the QH effect by breaking time-reversal symmetry. However, in systems with protected time-reversal symmetry, topological invariants exist due to spin-orbit interactions and are defined by the $\mathbb{Z}_2$-invariant. In three dimensions, one has four time-reversal invariant momenta. These additional invariant momenta distinguish between a "strong" and a "weak" TI [7, 8]. In 3DTI, the existence of two symmetries, for instance, time-reversal- and inversion-symmetry, protects the surface state. However, this is quite different in Weyl semimetals. As the derivation in Sec.2.1.2 will show, symmetry breaking is necessary to obtain a pair of Weyl cones. This leads to peculiar effects like chiral anomaly and the Quantum Anomalous Hall Effect (QAH), that are discussed in Sec.2.4. Therefore, the breaking of each of these symmetries will be represented. Moreover, the Weyl fermions are a solution of the Dirac equation which gives rise to the idea of creating Weyl semimetals by layers of magnetically doped TIs. In contrast to TIs, the Weyl semimetal band structure has gappless bulk and surface states at the same time. This interesting band structure will be discussed in Sec.2.4.3 with a focus on conductance effects.

Beyond the particles and materials, it is of interest in this thesis, to study the effects of electron-phonon interaction. Sec.2.7 gives an insight about electron-phonon coupling and deformations in isotropic media. The effects of electron-phonon interaction will be evaluated by the Boltzmann-equation and by the Kubo-formula. A rather new approach which is quite useful to study one-dimensional systems, is bosonization. A short introduction to this topic will be given in Sec.2.6.

2.1 Dirac and Weyl Fermions

With the interaction of fermions being the key interest in this work, the theoretical basis of Dirac and Weyl fermions is discussed in this section. Since Weyl fermions are a solution of the Dirac equation found by Hermann Weyl in 1929 [3], this section follows the derivation of Weyl fermions from the Dirac equation, proposed by Paul Dirac in 1928 [2]. The solution is followed by the massless chiral fermions leading to the Weyl equation [3, 38].

2.1.1 Dirac fermions

Dirac fermions are the solution of the Dirac equation

$$(i\gamma^\mu \partial_\mu - m)\psi(x) = 0 \tag{2.1}$$

and represent spinful, relativistic particles in μ time and space dimensions. The continuity equation gives restrictions to the properties of the Dirac matrices, which in three dimensions need at least a dimension of 4×4. Therefore, they can be defined as

$$\gamma^0 = \begin{pmatrix} \mathbb{I} & 0 \\ 0 & -\mathbb{I} \end{pmatrix} \quad \text{and} \quad \gamma^k = \begin{pmatrix} 0 & \sigma^k \\ -\sigma^k & 0 \end{pmatrix} \tag{2.2}$$

in Dirac basis where σ^k with $k = 1, 2, 3$ are the Pauli matrices and $\mathbb{I}$ is the 2×2 identity matrix. The matrix γ^0 is hermitian, while the matrices γ^k are antihermitian. The γ-matrices anticommute with each other, i.e. $\{\gamma^i, \gamma^j\} = 0$, if $i \neq j$. The result of Eq.(2.1) is the Dirac fermion. The free Dirac theory is invariant under charge conjugation, parity and time-reversal symmetry ($\mathcal{CPT}$) separately. In nature, however, these symmetries can be violated.

Invariant systems can for instance protect states and therefore lead to a certain topology. Transformation under parity is denoted by $\mathcal{P}$ and leads to inversion in spacial coordinates. Invariance under inversion (or parity) implies that $\mathcal{P}H(\mathbf{k})\mathcal{P}^{-1} = H(-\mathbf{k})$, i.e. the inverted momentum should keep the spin. The system is then even under inversion. The inversion operator $\mathcal{P}$ has the eigenvalues ± 1, where $\mathcal{P}^2 = 1$.

Time-reversal transformations reverses the time within a system. In a system with time-reversal symmetry ($\mathcal{T}$) a particle will follow the same trace back, if time goes reverse. This symmetry can be broken for instance by applying a magnetic field. A Bloch Hamiltonian $h(k)$ with momentum k is $\mathcal{T}$-invariant if $\mathcal{T}h(k)\mathcal{T}^{-1} = h(-k)$. A spinful particle obeys the $\mathcal{T}$-operator $\mathcal{T} = i\sigma^2 K$, where σ^2 (also σ_y) is the Pauli matrix for spin and K is the complex conjugation operator. Acting twice, the operator yields $\mathcal{T}^2 = -1$ for a particle with half-integer spin. Moreover, the operator of a spinful particle is odd under $\mathcal{T}$-symmetry. Kramers degenracy is given for a $\mathcal{T}$-invariant system with spin 1/2 particles that obtain the same eigenenergies while having opposite spin.

Charge conjugation implies that a fermion transforms into its antiparticle while keeping the spin. A system with such symmetry obeys $C^{-1}\gamma^\mu C = -\gamma^\mu$ where $C = i\gamma^2\gamma^0$ is the charge conjugation matrix [39–42].

Sec.2.3.1 will present how these symmetries protect the Dirac fermion in the topological insulator. In the following, the Weyl equation will be derived and one of the invariances will be lost due to neglecting the mass term.

2.1.2 Weyl fermions

One year after the proposal of the Dirac equation, Hermann Weyl derived another solution of the Dirac equation by setting the mass $m \to 0$ [3, 38]. An important condition is that the particle is massless, or at least has a very small mass compared to its momentum. Thus, the mass term can be set to $m = 0$. An example for a fermion with nearly zero mass and a half-integer spin is the neutrino [41]. In fact, $m = 0$ decouples the Dirac equation in the sense that each component of ψ becomes independent. Hence, the Dirac equation in three dimensions remains

$$\sum_{\mu=0}^{3} \gamma^{\mu} \partial_{\mu} \psi(x) = 0 \tag{2.3}$$

and therefore, one can write the Hamiltonian as

$$i\frac{\partial \psi}{\partial t} = -i\left(\gamma^0\gamma^1\frac{\partial \psi}{\partial x^1} + \gamma^0\gamma^2\frac{\partial \psi}{\partial x^2} + \gamma^0\gamma^3\frac{\partial \psi}{\partial x^3}\right) \tag{2.4}$$

since γ^0 is hermitian. Following the anti-commutation relation of Dirac-matrices one finds that the matrix

$$\gamma_5 = i\gamma_0\gamma_1\gamma_2\gamma_3 = \begin{pmatrix} 0 & \mathbb{I} \\ \mathbb{I} & 0 \end{pmatrix} \tag{2.5}$$

commutes with the helicity $\mathbf{\Sigma} \cdot \mathbf{k}$ where $\mathbf{\Sigma}$ defines the spin and $\mathbf{k}$ the momentum [41]. The γ^5-matrix has also common eigenfunctions with the helicity operator. While the helicity describes whether the spin of a particle has the same or the opposite direction as the momentum, the γ^5 matrix is responsible determining the sign of energy and therefore is also called the *chirality operator*. Hence, in case of Weyl fermions the helicity is equal to the chirality since it is massless. Splitting the chirality operator into its eigenvalues ±1, it reduces the γ-matrices to σ-matrices. Furthermore, the spinor ψ has to fulfill $\gamma^5\psi = \pm\psi$. Thus, Eq.(2.4) yields

$$i\partial_t \psi_{\pm} = \mp\vec{\sigma} \cdot \vec{p}\, \psi_{\pm} \tag{2.6}$$

resulting in two chiral fermions, one with a right-handed chirality ψ_+ and one with a left-handed chirality ψ_-. This equation describes the Weyl fermions. It is invariant under charge conjugation and parity,i.e. $\mathcal{CP}$, where the $\mathcal{CP}$ conjugate of a Weyl fermion with left-handed chirality is a Weyl fermion with right-handed chirality [43].

In condensed matter physics, the Nielsen-Ninomiya theorem states that a massless chiral fermion requires the existence of a fermion with opposite chirality in order to keep gauge invariance in an electromagnetic field. Otherwise, the gauge field is anomalous. This means that within a Brillouin zone (BZ) the number of positive and negative chiralities is equal [38].

Heretofore, Dirac and Weyl fermions have been introduced. The following section addresses the topology and thus, the reason for the appearance of Dirac and Weyl fermions in a topological system. Furthermore, the section covers the symmetries that determine the topology.

2.2 Topological invariants

As topological material is of main interest in this thesis, the concept of topological invariants is discussed in this section. The topological invariant is deduced by the Berry-connection and can be expressed by a physical quantity. This can have different consequences for the system, for instance a system imposes a topologically insulating phase with two protected gapless edge states. In 1982 Thouless *et al.* showed the Chern invariant appears within the Hall conductivity [5]. The Chern invariant follows from an analogy between condensed matter physics and topology [42]. In a 2DTI (two dimensional TI), this phase was shown to be the Quantum Spin Hall (QSH) effect by Kane and Mele [6, 8]. While the QH effect requires broken $\mathcal{T}$-symmetry, the QSH phase phase is $\mathcal{T}$-symmetric. Therefore, Moore and Balents generalized this to the $\mathbb{Z}_2$-invariant model including $\mathcal{T}$-symmetric systems. Moreover, Fu, Kane and Mele established an extended model for 3DTI systems involving four invariant momenta [8]. This section represents topological invariants and their consequences for materials and begins with the Chern invariant.

2.2.1 Berry Phase

In 1984, M. Berry pointed out, that the phase difference of wave functions has impact on adiabatic systems [44, 45]. Some years earlier, in 1959, Y. Aharonov and D. Bohm discovered that an electromagnetic potential leading to a magnetic flux has influence on charged particles, namely, the *Aharonov-Bohm-Effect* [46]. The consequences of phases that occur from potentials arise in physical properties. A system that changes adiabatically in time depends on a real phase

$$\Phi(t) = i \int_{\mathbf{r}(0)}^{\mathbf{r}(t)} \langle u(\mathbf{k}) | \nabla_{\mathbf{k}} | u(\mathbf{k}) \rangle \cdot d\mathbf{S} \tag{2.7}$$

the s.c. Berry phase and

$$\mathcal{A}(\mathbf{k}) = \langle u(\mathbf{k}) | \nabla_{\mathbf{k}} | u(\mathbf{k}) \rangle \tag{2.8}$$

is the Berry-connection where $|u(\mathbf{k})\rangle$ are the eigenstates of a Hamiltonian $H(\mathbf{k})$ and the momentum $\mathbf{k}$ is defined within a contour of path $\mathcal{C}$. The curl of the Berry-connection, the Berry curvature,

$$\Omega(\mathbf{k}) = \nabla_{\mathbf{k}} \times \mathcal{A}(\mathbf{k}) \tag{2.9}$$

solves the surface integral over a closed loop with the path $\mathcal{C}$. The importance of $\Omega(\mathbf{k})$ exists within the Chern invariant

$$n_{\mathbf{k}} = \frac{1}{2\pi} \int_{\mathcal{C}} \Omega(\mathbf{k}) \cdot d\mathbf{S} \tag{2.10}$$

where $\Omega(\mathbf{k}) \cdot d\mathbf{S}$ describes the topology of the path $\mathcal{C}$ by the sources or sinks of $\Omega(\mathbf{k})$. Hence, the Chern invariant is a topological invariant, depending on the Berry-connection. Furthermore, the Gauss-Bonnet theorem connects the Berry curvature of a given surface $d\mathbf{S}$ to the topological invariant. Moreover, the Chern invariant is the quantity that stays in systems which change adiabatically like, for instance, a Hamiltonian. Degenerate points play a huge role for the Chern-invariant since they act as monopoles in parameter space. The integration over a two-dimensional surface then leads to the integer in Eq. (2.10), the Chern number [39]. In 2004, Haldane stated that the Berry phase is a topological property [47]. The connection between the Berry phase, or the Chern number, and condensed matter physics will be discussed in the following.

2.2.2 Quantum Hall Effect

The integer Quantum Hall (IQH) state describes the conductance increase in steps of conductance quanta e^2/h, while an external magnetic field is applied. The magnetic field leads to Landau level and, furthermore, to the quantized Hall conductance. The conductance steps are defined by the carrier concentration N [4]. Based on the experimental investigation by v. Klitzing *et al.*, Thouless *et al.* showed, that topology is responsible for the difference between the QH state and an ordinary insulator [5]. The Chern invariant with integer-valued invariant

$$n_i = \frac{1}{2\pi} \int_{BZ} \nabla_{\mathbf{k}} \times \mathcal{A}(\mathbf{k}) \tag{2.11}$$

appears as the quantized Hall conductivity

$$\sigma^{xy} = \frac{Ne^2}{h} \tag{2.12}$$

with the Chern number $N = \sum_i n_i$ defined by the sum over all Chern invariants. Thus, the IQH state is of topological nature. The TKNN[1] integers N are elements of the homotopy groups $\pi(M) = 0$ or $\pi(M) = \mathbb{Z}^{n-1}$ [48, 49]. The homotopy groups describe continuous deformations between functions. An example is given by the deformation of a torus into a mug which keeps the "gap". In contrast a deformation into a sphere would close the gap since it corresponds to a different invariant [42]. The homotopy groups $\pi(M)$ represent topological manifolds M that can be obtained from a sphere S^n. In condensed matter physics, one finds the Brillouin zone is topologically equivalent to a torus and the band structure can be treated as a map to the Bloch Hamiltonian similarly [45, 49].

Another important aspect is that the Hall conductivity requires a broken $\mathcal{T}$-symmetry at zero magnetic field [47]. However, in some systems, where $\mathcal{T}$-symmetry is given, another interaction can be responsible for the topological order without even breaking $\mathcal{T}$-symmetry. Based on Haldane's model, Kane and Mele showed that spin-orbit interactions provide a topologically non trivial phase in a $\mathcal{T}$-invariant system with Dirac fermions as well [6, 8]. The $\mathcal{T}$-operator yields $\mathcal{T}^2 = -1$ for spinful particles with half-integer spin. The consequence is described by Kramers' theorem and requires at least twofold degenerate states as eigenstates of the $\mathcal{T}$-operator. Therefore, the spinful fermions yield a QSH conductivity. What distinguishes the QH and the QSH states from ordinary insulators are the gapless edge states appearing in two dimensionsional systems [50]. If spin-conservation is not given anymore, the edge states form a Kramers doublet which protects those states even, if $\mathcal{T}$-symmetry is given. Therefore, the Hall conductivity provided by broken $\mathcal{T}$-symmetry cannot be the only topological aspect which stabilizes the system. Kane and Mele showed that the $\mathbb{Z}_2$ topological invariant distinguishes the QSH insulator from an ordinary insulator analog to the TKNN invariant [51].

Experimental investigation showed that the QSH insulating state exists in quantum well structures made of stacked layers of HgTe and CdTe. These materials belong to the family of semimetals and semiconductors and provide a zinc blende lattice structure [52, 53]. The group of König *et al.* measured quantized conductance provided by the edge states [1].

---

[1] D. J. Thouless, M. Kohmoto, M. P. Nightingale and M. den Nijs [5]

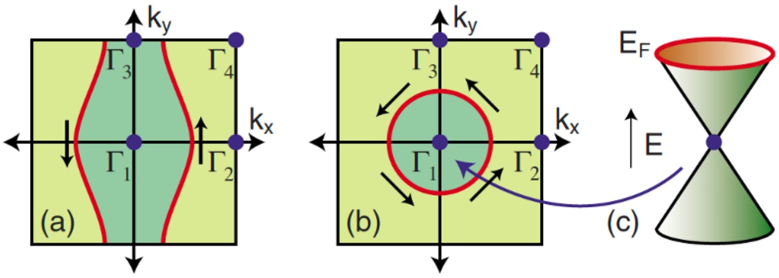

Figure 2.1: TRIM $\Gamma_{1,2,3,4}$ of (a) a weak TI (b) a strong TI. (c) Dirac cone inside the Fermi surface arc. Adapted from Ref. [53].

2.2.3 Topological invariance in three dimensions

The existence of gapless edge states in a two dimensional system was fundamental to explore the three dimensional generalization of the QSH phase. Two years after the QSH state was deduced, Moore and Balents extended the model by suggesting a three dimensional Brillouin Zone with given $\mathcal{T}$-invariance [49]. The result is a phase with four $\mathbb{Z}_2$ invariants for each pair of bands. Fu, Kane and Mele distinguished between "weak" and "strong" TI phases, based on a fourth invariant [8]. Furthermore, Roy derived the QSH effect in three dimensions [54].

In three dimensions, one has eight $\mathcal{T}$-invariant momenta (TRIM) which correspond to four $\mathbb{Z}_2$ invariants $\nu_0;(\nu_1\nu_2\nu_3)$. Three of the four invariants describe the layers of each two dimensional plane. The invariant ν_0 distinguishes between weak and strong TI phases. It is zero, if the phase is a weak TI and $\nu_0 = 1$, if the phase corresponds to a strong TI. The phases are distinguished by the number of Kramers degenerate Dirac point pairs the surface Fermi surface intersects. The degenerate Dirac points resemble the Kramers degenerate points in the surface Brillouin zone. Fig.2.1 shows the TRIM $\Gamma_{1,2,3,4}$ for a weak and strong TI phase. The weak TI behaves similar to layers of 2D QSH states. The phase is called a "weak" insulator since the band in that system intersects the Fermi energy between an even number of invariant points, for instance Γ_1 and Γ_2 as well as Γ_3 and Γ_4. Hence, the weak periodic potentials occur providing a gap and for clean surfaces one finds surface states. Nonetheless, disorders reduce topological distinction and lead to a localization of surface states [8, 53].

The strong TI phase cannot be obtained from stacking layers of 2DTIs, as the Kramers' degenerate Dirac points are confined within the Fermi surface arc. A simplified model is shown in Fig.2.1 where Γ_1 appears as a single Dirac point. What makes the strong TI unique is this single Dirac point. Although the Dirac point with a given spin appears to be a single Dirac point, the fermion doubling theorem by Nielsen and Ninomiya remains valid. The other Dirac point, however, can be found for a Dirac cone with opposite mass sign [7]. Then, the Berry phase follows from spin-momentum locking around the Fermi surface [8, 53, 55].

One proposed material was Bismuth since bilayer Bismuth imposes a QSH phase [8]. Realizations of strong TIs with Bismuth and the crystal structure will be discussed in Sec. 2.3.

2.2.4 Topological semimetals

As the name reveals, topological semimetals require the topological invariant to be connected to the Fermi arc. The Berry curvature, which is shown in Eq.(2.9), is a topological quantity. While the magnetic flux **B** is not a topological quantity, it acts as a normal flux where magnetic monopoles do not occur. The Berry curvature, however, is a topological quantity and can have magnetic monopoles. For a two dimensional Fermi surface sheet that confines the Berry curvature, a monopole will lead to the Chern number

$$C = \frac{1}{2\pi} \int \Omega(\mathbf{k}) \cdot d\mathbf{S} = \pm 1 \tag{2.13}$$

corresponding to a topological charge of ±1 depending whether it is a source or sink [56]. Weyl points can be characterized as such monopoles [57]. The Chern number can be associated with the chirality of the Weyl nodes. However, the monopoles being degenerate points of the Berry curvature require a broken inversion or $\mathcal{T}$-symmetry to lift the Kramers' degeneracy. As shown in Sec.2.1.2 the Weyl equation fulfills this requirement, since it implies a broken symmetry. This is necessary to define a topological metal. Hence, Fermi energy at the Weyl nodes has topological consequences, for instance the quantum anomalous Hall (QAH) effect. A 3DTI doped with magnetic impurities can provide broken $\mathcal{T}$-symmetry. A thin film with two dimensional Dirac surface states will then have the form

$$H_r = v_F(\hat{z} \times \vec{\sigma}) \cdot \mathbf{k} + (b + r\Delta_S)\sigma^z \tag{2.14}$$

where the Dirac fermion has the mass $m = b + r\Delta_S$ with $r = \pm$ and the tunneling amplitude Δ_S between the surfaces of the film and the exchange spin-splitting b provided by magnetic impurities. If the Fermi energy lies close to the nodes of the Dirac fermions, the Hall conductivity contributed by each fermion

$$\sigma^r_{xy} = \frac{e^2}{2h}\mathrm{sgn}(m) \tag{2.15}$$

acts anomalous as m and, therefore also σ^r_{xy}, vanishes. The Hall conductivity is exactly half of the conductivity a normal TI has and depending on the mass it imposes a critical point between a TI and an ordinary insulator [56, 58]. The idea of stacking TI layers will be discussed later leading to the Weyl semimetal heterostructure (s.Fig.2.5) proposed by Burkov and Balents in Ref. [13]. For a better understanding of the QAH effect in Weyl semimetals, the model of a Weyl semimetal has to be discussed, first. A further insight to this and the QAH effect will be given in Sec.2.4.

2.2.5 Topological superconductivity and Majorana fermions

Another topological classification, that is briefly mentioned here, are topological superconductors. Their importance lies within the Majorana fermions, named after Ettore Majorana [59]. More particularly, a qubit can be constructed by Majorana bound states. Majorana fermions are their own antiparticles and fulfill $\gamma_j = \gamma_j^\dagger$. This follows from the intrinsic particle-hole symmetry of the Bogoliubov-de Gennes Hamiltonian within the superconducting Hamiltonian [39]. Analog to the TI, the topological superconductor has egde states described by the Majorana fermions that are topologically protected [52, 53]. The $\mathcal{T}$-symmetric topologically superconducting phase refers to a $\mathbb{Z}_2$ topological quantum number [60].There are many similarities between the $\mathcal{T}$-invariant QSH states and the

$\mathcal{T}$-invariant topological superconductors. Equivalent to the QSH state, the topological superconductor provides helical edge states in form of Majorana edge states. Furthermore, a Majorana fermion can be treated as half of a Dirac fermion and similarly to the QSH state the edge states counterpropagate.

So far, the topological invariants have been discussed. The topological invariant is a mathematical description that can be utilized to define the topological equivalent characterizing the band structure. Therefore, topological phases can be defined. One of these phases, is the 3DTI. The following section describes the crystal structure of the 3DTI Bi_2Se_3 and presents the symmetries which lead to the topological protection of the surface states.

2.3 Topological insulators

Similar to the ordinary insulator, the topological insulator (TI) has an insulating bulk gap. What makes it a TI, is the topologically protected, gapless surface state. The topological protection follows from time-reversal symmetry and is discussed further in Sec.2.3.1. In a 2DTI one $\mathbb{Z}_2$ invariant momentum protects the surface state. In a 3DTI, there exist four $\mathbb{Z}_2$ invariant momenta which protect the surface state. As the 3DTI is of large interest in this thesis, the crystal structure and symmetries of Bi_2Se_3 that is part of the Bismuth-family will be represented in the following section. The symmetry is fundamental for the model Hamiltonian describing the TI in Sec.2.3.2. The effective surface Hamiltonian, defining the topological surface states follows from the model Hamiltonian.

2.3.1 Symmetries

Topological insulating phases can be found in Bismuth-alloys. While the first generation of 3DTI, $Bi_{1-x}Sb_x$, was difficult to study due to its small band gap, the group from Princeton University by Hasan showed the existence of Dirac cones in Bi_2Se_3 [12]. The crystal structure belongs to the $D^5_{3d}(R\bar{3}m)$ space group and is composed of s.c. quintuple-layers. Furthermore, Bi_2Te_3 belongs to the same space group and has an equivalent rhombohedral crystal structure [52]. Since chapter 3 focuses on a bulk-insulating TI as well, for a better understanding of the symmetries in 3DTI, the Bismuth-family is discussed, first. It will be shown later that HgTe, known as a 2DTI, imposes a bulk-insulating TI, when it is strained [20].

The crystal structure of Bi_2Se_3 is shown Fig.2.2. A gap of $\approx 0.3\,\mathrm{eV}$ of the lowest band makes Bi_2Se_3 a bulk insulator. The two lattice constants a and c are defined in the x-y-plane and in z-direction, respectively. Furthermore, the primitive lattice vectors are given by $\mathbf{t}_1 = (\sqrt{3}a/3, 0, c/3)$, $\mathbf{t}_2 = (-\sqrt{3}a/6, a/2, c/3)$ and $\mathbf{t}_3 = (-\sqrt{3}a/6, -a/2, c/3)$.
Inversion symmetry of the Se2 site with respect to the center appears at first sight, while Bi1 and Se1 have their inversion center in the Se2 site. For instance, the Bi1 (Se1) atoms impose inversion symmetry with the Se2 atoms being the center of inversion. Two- and threefold rotation symmetries exist along the x- and the z-direction. $\mathcal{T}$-invariance is represented in Fig.2.3, where the red points show the $\mathcal{T}$-invariant momenta. As already stated, the $\mathcal{T}$-operator for a spinful particle is $\mathcal{T} = i\sigma_y K$.

As discussed in the previous section, spin-orbit interaction can lead to the QSH effect and further to the $\mathcal{T}$-invariant momenta. The $\mathcal{T}$-invariant momenta Γ, F, L and Z are presented in Fig.2.3 and lead to four $\mathbb{Z}_2$-invariants classifying the TI. Turning on spin-orbit coupling (SOC), band inversion close to the Γ-point arises and changes the parity

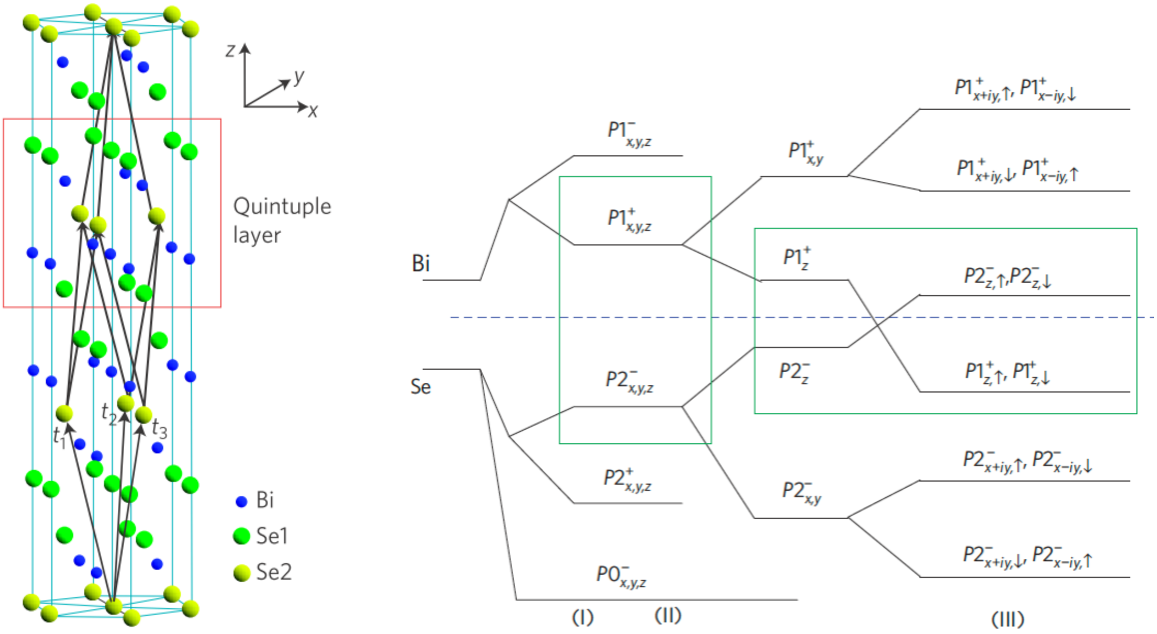

Figure 2.2: Left: The red box shows the quintuple layer structure of Bi_2Se_3. The primitive lattice vectors are labeled $\mathbf{t}_{1,2,3}$. Right: SOC acting on the states of Bi and Se leading to inversion of the states. The Fermi energy is set on the blue line. The horizontal green box represents the basis states. Both figures are adapted from Ref. [61].

of an occupied band [61]. The states of Bi and Se are pushed into opposite directions due to chemical bonds and their orbitals are split into two perpendicular directions. This is shown in Fig.2.2 and follows from crystal structure. Crystal-field splitting then provides a repulsion between these perpendicular states (II) and beyond a critical value of SOC their energies become inverted (III). Furthermore, these states are now doubly degenerate [52, 61, 62].

Fig.2.3 shows a high-resolution ARPES measurement of the second generation 3DTI Bi_2Se_3. The method of ARPES implies measuring the energy of electrons. Those occur from the photoelectric effect provided by a radiation beam on the sample. ARPES measurement is a technique which is used often to study topological material since it allows for the distinction between bulk and surface states [11, 63]. A photon energy of about 22 eV was used in this measurement along the 2D BZ momenta represented in Fig.2.3. The measurements show a single Dirac cone. Bi_2Se_3 is stochiometric and, therefore, it can have a high purity. Including the large band gap of $\sim 0.3\,\mathrm{eV}$ of Bi_2Se_3, TI states at room temperature are possible. Furthermore, the topological states are protected by $\mathcal{T}$-symmetry. Nonetheless, a gap within the surface spectrum can appear due to magnetic impurities breaking the symmetry [53, 64]. TI nanoribbons of Bi_2Se_3 showed Aharonov-Bohm oscillations at low temperatures. Also, a quantized conductance e^2/h was estimated in the experiments of Ref. [21]. The effects of an applied magnetic field on the conductance oscillations will be further discussed in Sec.2.3.3.

The model Hamiltonian has to obey the symmetries in order to fulfill the topology of a 3DTI. In the following section, the corresponding model Hamiltonian will be evaluated.

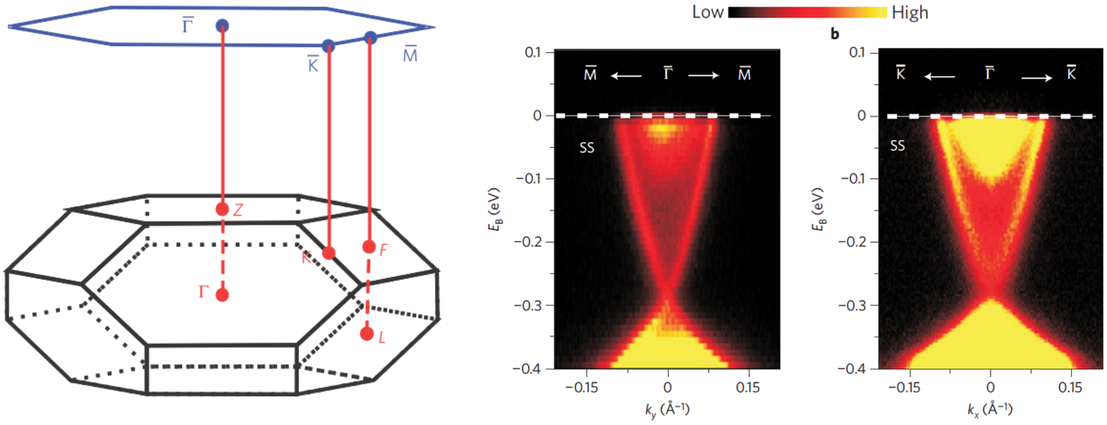

Figure 2.3: Left: Brillouin Zone of Bi_2Se_3. The $\mathcal{T}$-invariant momenta are represented by the red points. The high-symmetry momenta are indicated by the blue points in the 2D BZ. Adapted from Ref. [61]. Right: ARPES measurements representing the surface band dispersion of the 3DTI Bi_2Se_3 (111) close to the Γ-point along the 2D BZ momenta $\bar{\Gamma} - \bar{M}$ and $\bar{\Gamma} - \bar{K}$. Adapted from Ref. [12].

2.3.2 Band structure and surface states

The model Hamiltonian was derived in two different steps, first by exploiting the crystal structure and atomic orbitals, second by symmetry principles. In both cases the previously mentioned symmetries and spin-orbit coupling play an important role. This section represents the properties of the model Hamiltonian and the resulting band structure. Topology as well as the ARPES measurements showed that the system can be represented by low-energy physics close to the Γ-point. The basis describing the conduction and valence band consists of four states. The parameters of the system were determined by fitting the bands onto *ab initio* calculations. Moreover, the basis can be represented by the symmetries which were discussed in the previous section. The low-energy Hamiltonian can be obtained from expansion to the order of $\mathcal{O}(\mathbf{k}^2)$ of a 4×4-Dirac Hamiltonian. Thus, a model Hamiltonian which obeys the topology of a 3DTI with a single Dirac cone can be represented by

$$H_{eff} = \begin{pmatrix} \epsilon_0(\mathbf{k}) + \mathcal{M}(\mathbf{k}) & \mathcal{A}_1 k_z & 0 & \mathcal{A}_2 k_- \\ \mathcal{A}_1 k_z & \epsilon_0(\mathbf{k}) - \mathcal{M}(\mathbf{k}) & \mathcal{A}_2 k_- & 0 \\ 0 & \mathcal{A}_2 k_+ & \epsilon_0(\mathbf{k}) + \mathcal{M}(\mathbf{k}) & -\mathcal{A}_1 k_z \\ \mathcal{A}_2 k_+ & 0 & -\mathcal{A}_1 k_z & \epsilon_0(\mathbf{k}) - \mathcal{M}(\mathbf{k}) \end{pmatrix} + \mathcal{O}(\mathbf{k}^2) \tag{2.16}$$

where the energies are given by $\epsilon_0(\mathbf{k}) = C + D_1 k_z^2 + D_2 k_\perp^2$ and $\mathcal{M}(\mathbf{k}) = M - B_1 k_z^2 - B_2 k_\perp^2$ with $k_\pm = k_x \pm i k_y$ and $k_\perp = \sqrt{k_x^2 + k_y^2}$. The parameters are shown in the App.A.1 Tab.A.1. Furthermore, one finds band inversion near $\mathbf{k} = 0$ representing the topology [61].This model Hamiltonian is fundamental to the following discussion and the topic of chapter 3, where a system with a single Dirac cone is considered.

Surface states in half-space geometry

Characterizing the topology, surface states are a very interesting aspect in the TI. The density of states can be obtained by *ab initio* calculations. These calculations also showed a higher density of states near the Γ-point representing the surface states. Moreover, a surface Hamiltonian can give information about the connection between the bulk-Hamiltonian and the topology of surface states. In order to obtain surface states in half-space geometry, i.e. imposing open boundary conditions for $z > 0$, the Hamiltonian can be written as $H = H_0 + H_1$, where one part depends only on momenta in z-direction. The first part is

$$H_0 = \begin{pmatrix} \tilde{\epsilon}(k_z) + \tilde{\mathcal{M}}(k_z) & \mathcal{A}_1 k_z & 0 & 0 \\ \mathcal{A}_1 k_z & \tilde{\epsilon}(k_z) - \tilde{\mathcal{M}}(k_z) & 0 & 0 \\ 0 & 0 & \tilde{\epsilon}(k_z) + \tilde{\mathcal{M}}(k_z) & -\mathcal{A}_1 k_z \\ 0 & 0 & -\mathcal{A}_1 k_z & \tilde{\epsilon}(k_z) - \tilde{\mathcal{M}}(k_z) \end{pmatrix} \tag{2.17}$$

of order k_z^2 where $\tilde{\epsilon}(k_z) = C + D_1 k_z^2$ and $\tilde{\mathcal{M}}(k_z) = M - B_1 k_z^2$ the second part

$$H_1 = \begin{pmatrix} -B_2 k_\perp^2 & 0 & 0 & \mathcal{A}_2 k_- \\ 0 & B_2 k_\perp^2 & \mathcal{A}_2 k_- & 0 \\ 0 & \mathcal{A}_2 k_+ & -B_2 k_\perp^2 & 0 \\ \mathcal{A}_2 k_+ & 0 & 0 & B_2 k_\perp^2 \end{pmatrix} \tag{2.18}$$

of order $k_\perp^2$ [52, 62]. Moreover, according to half-space geometry, one can now solve the Schrödinger equation. The block diagonal Hamiltonian allows for eigenstates of two two-component spinors $\Psi_\uparrow = (\phi(z), \vec{0})^T$ and $\Psi_\downarrow = (\vec{0}, \phi(z))^T$ where the function $\phi(z) = \tilde{\phi} e^{\lambda z}$ includes a two-component wave function $\tilde{\phi}$ with eigenstates $\varphi_\pm$ [52, 62]. Moreover, the wave function yields

$$\phi(z) = \begin{cases} a\left(e^{\lambda_1 z} - e^{\lambda_2 z}\right)\varphi_+ & \text{, for } \mathcal{A}_1/B_1 > 0 \\ c\left(e^{-\lambda_1 z} - e^{-\lambda_2 z}\right)\varphi_- & \text{, for } \mathcal{A}_1/B_1 < 0 \end{cases} \tag{2.19}$$

with

$$\lambda_{1,2} = \frac{1}{2B_1}\left(-\mathcal{A}_1 \pm \sqrt{4MB_1 + \mathcal{A}_1^2}\right)$$

where the sign of $\mathcal{A}_1/B_1$ defines the helicity [52,62]. Furthermore, projecting the states in the subspace of the eigenstates denoting the surface states, one finds the surface Hamiltonian

$$H_{surf}(k_x, k_y) = C + \mathcal{A}_2(\sigma_x k_y + \sigma_y k_x) \tag{2.20}$$

where $C \ll \mathcal{A}_2$. Thus, the surface Hamiltonian describes a Dirac fermion. Hence, one obtains a Fermi velocity of $\mathcal{A}_2/\hbar \sim 6.2 \times 10^5$m/s for the surface states (s.App.A.1, Tab.A.1). The effective surface state Hamiltonian allows for further investigation of surface states, for instance electron-phonon interaction [27,28,65]. Considering electron-phonon interaction in a TI with open boundary conditions, one finds a Bloch-Grüneinsen temperature of $T_{BG} = 3.9\,\mathrm{K}$ referring to Rayleigh surface modes which propagate along the surface and dominate at low-temperatures [27,66]. The consequence of electron-phonon scattering is a resistivity with a temperature dependence of $\rho \propto T^5$ for $T \to 0$. At high temperatures the resistivity scales with $\rho \propto T$ with a dominant contribution from longitudinal modes [27]. A general insight about phonon modes and their interaction with electrons will be given in Sec.2.7.

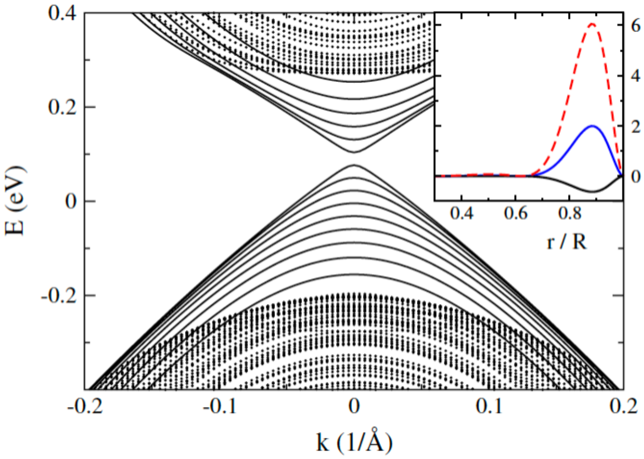

Figure 2.4: Numerically estimated band structure of a $\mathrm{Bi_2Se_3}$ nanowire with radius $R = 15\,\mathrm{nm}$. The bulk states are represented by the dots and surface states by lines. The inset shows the charge density (red dashed line), the angular spin density s_ϕ (blue line) and spin density along the wire s_z (black line) with respect to the radius of a state with momentum $k = 0.02\,\text{Å}$ along the wire and angular momentum $j = 1/2$. The densities increase near the surface indicating surface states. Adapted from Ref. [19].

Surface states in a topological insulator nanowire

The model of an infinitely long nanowire can be considered as a cylinder along the z-direction with a radius R. The total angular momentum operator $J_z = -i\partial_\phi + \sigma_z/2$ is conserved and its eigenvalues are given by half-integer values j. Solving the model Hamiltonian in Eq.(2.16) with respect to radial coordinates, one finds orthonormal radial eigenfunctions

$$\psi_{j\mp 1/2,n}(r < R) = \frac{\sqrt{2}}{RJ_{j\mp 3/2}(\gamma_{j\mp 1/2,n})} J_{j\mp 1/2}\left(\gamma_{j\mp 1/2,n}\frac{r}{R}\right) \tag{2.21}$$

where ± corresponds to the spin and $\gamma_{p,n}$ is the pth zero of the nth Bessel function $J_n(z)$ of the first kind. The boundary condition for an infinite long nanowire requires that the wave functions vanish at the boundary $r = R$. The band structure then follows from the model Hamiltonian and provides a gapped surface state. Fig.2.4 presents the numerically derived band structure in a TI nanowire based on the diagonalized Hamiltonian [19]. One observes the bulk gap of $\sim 0.3\,\mathrm{eV}$ and the surface state gap for the given radius is $\sim 30\,\mathrm{meV}$. The fermion moves with a momentum k along the cylinder and has an angular momentum j perpendicular to the momentum. One can obtain the surface states in a nanowire geometry by wrapping the surface Hamiltonian on a cylindrical surface. Thus, the Hamiltonian described in Eq.(2.20) can be expressed as a curved surface. A Dirac fermion can in general be described by $H = \mathbf{n}\cdot(\mathbf{p}\times\vec{\sigma})$, if the spin is perpendicular to the momentum. This is the case in a TI nanowire. The effective Hamiltonian of a curved surface is then defined by $H = \sigma_\phi p_z - \sigma_z p_\phi$ where

$$\sigma_{r,\phi} = U^\dagger(\phi)\sigma_{x,y}U(\phi) \tag{2.22}$$

are "cylindrical" Pauli matrices with $U(\phi) = e^{i\phi\sigma_z/2}$, $p_z = -i\partial_z$ and $p_\phi = -i/R\ \partial_\phi$ [65]. Moreover, the effective Hamiltonian can be written in terms of a unitary transformation.

Assuming a magnetic flux Φ_B piercing the nanowire, the effective Hamiltonian describing the cylindrical surface with radius R yields

$$\mathcal{H}_{\mathrm{el}}(k) = e^{-i\phi\sigma_z/2}\left(v_1 k\sigma_y - \frac{v_2}{R}(-i\partial_\phi + \Phi_B)\sigma_z\right)e^{i\phi\sigma_z/2}, \tag{2.23}$$

where the Fermi velocities are $v_{1,2} = \mathcal{A}_{1,2}\sqrt{1-(D_2/B_2)^2}$ [19, 65]. $\mathcal{T}$-symmetry is responsible for certain topological aspects in the nanowire. First, the gap closes as the flux reaches a half-integer value and prohibits spin-conserving single-particle backscattering processes. Degenerate states exist for integer flux where elastic scattering between Kramers pairs is forbidden. The degeneracy is lifted, if the flux is noninteger [19, 67]. Nanowires and nanoribbons have already been synthesized. Experiments on transport properties in nanoribbons and nanowires have shown, that the conductance correction of surface states in Bi_2Se_3 and strained HgTe TI nanowires shows Aharonov-Bohm-type oscillations [20, 21]. The presented model of Ref. [19] will be utilized in chapter 3 to study the electron-phonon interaction in a TI nanowire [67].

2.3.3 Aharonov-Bohm oscillations in a TI nanowire

So far, the band structure of a TI nanowire surface state has been established. An interesting feature that has been observed for Bi_2Se_3 and HgTe nanowires are Aharonov-Bohm oscillations due to a magnetic field piercing the nanowire. One of the earliest observations was made by Peng *et al.* (Ref. [21]) where Aharonov-Bohm oscillations of the order h/e occured within the low-temperature resistivity of the nanoribbons. These nanoribbons were synthesized with layers of Bi_2Se_3 and a magnetic field was applied in direction of the ribbon length. The resistance was observed to oscillate in periods of an integer flux quantum. However, the surface states were expected to impose a closed gap at half-integer flux. Theoretical investigation in Ref. [22] by Bardason, Brouwer and Moore showed that these oscillations depend on the strength of the disorder as well as the location of the Fermi level. At small doping, near the Dirac point, one finds that the conductance maximum is given for half-integer flux. For larger doping the conductance oscillates with a period of integer flux and has a maximum either at zero or half-integer flux depending on the doping level.

Although HgTe is a semimetal it turns into a 3DTI when the tetragonal unit cell experiences a strain and the bulk states become gapped [68, 69]. The Dirac point in strained HgTe lies in the valence band and therefore cannot be accessed directly. Ziegler *et al.* (Ref. [20]) studied the conductance oscillations in strained HgTe in order to investigate the distinction between topological and trivial states in a 3DTI without an accessible Dirac point. Detecting the Aharonov-Bohm oscillations, conductance correction measurement was used to determine topological features. The gate voltage for instance gives information about the subband spacing as well as it responds to the spin degeneracy which allows the distinction between topological and trivial states. Moreover, their experiments showed that the transport in strained HgTe nanowires can reach a ballistic transport regime.

Chapter 3 discusses the ballistic transport in a TI nanowire with a magnetic field applied along the wire that is described as a Luttinger liquid [19]. A Luttinger liquid allows the description of quasiparticles in 1D that cannot be described by Fermi-Liquid theory anymore. Sec.2.6 presents the advantages of the Tomonaga-Luttinger liquid model and gives an overview about the method of bosonization.

2.4 Weyl semimetals

The existence of Weyl nodes in materials is not uncommon. However, a material with Fermi energy set at the Weyl nodes becomes interesting. Topology has consequences like the appearance of surface states as the Fermi arc and the QAH. Predictions for possible materials were made involving also TI layers with Fermi energy set at the Weyl nodes. The analogy from TIs with broken $\mathcal{T}$-symmetry gave large insight about the topology of Weyl semimetals (WSM). The WSM requires a broken symmetry. This can be either $\mathcal{T}$-symmetry or inversion symmetry ($\mathcal{P}$-symmetry). A material which imposes those states was recently discovered by the Princeton University group by Xu *et al.* (s.Ref [14]) and independently the same year by the IOP group by Lv *et al.* (s.Ref [16]). Experimental investigations showed topological Fermi arcs with nonvanishing Chern number in TaAs. ARPES measurements confirmed the coexistence of bulk Weyl cones and Fermi arcs.
In the following section, transport properties of WSMs will be discussed including important topological features like chiral anomaly.

2.4.1 Weyl semimetals from topological insulators

One proposal for a WSM was made by Burkov and Balents in 2011 [13]. Based on the idea of 3DTI films with magnetic impurities, they proposed a multilayer heterostructure of TIs and ordinary insulators. The proposed heterostructure is shown in Fig.2.5 with TI layers in orange and layers of the ordinary insulator in between. Δ_S defines the tunneling amplitude between the surfaces of each layer and Δ_D represents the tunneling through the ordinary TI, for instance between adjacent surfaces of TI layers. A simplified version of that model can be obtained by canonical transformation and yields

$$H(\mathbf{k}) = v_F(k_y\sigma^x - k_x\sigma^y) + (m \pm \Delta(k_z))\sigma^z \tag{2.24}$$

for each block of the diagonalized Hamiltonian with $\Delta(k_z) = \sqrt{\Delta_S^2 + \Delta_D^2 + 2\Delta_S\Delta_D\cos(k_z d)}$ and superlattice period d. If the mass m vanishes, Dirac nodes emerge for $\Delta_S/\Delta_D = \pm 1$ at $k_z = \pi/d$ or $k_z = 0$, otherwise the system is gapped [56, 57]. However, block-diagonalization shows, that these nodes are actually two Weyl nodes at the same momentum. Since they are topologically unstable, m must not vanish, such that the Weyl nodes are separated in momentum-space and $\mathcal{T}$-symmetry is broken. Then, one finds two separated nodes at

$$k_z^{\pm} = \pi/d \pm k_0 = \pi/d \pm \frac{1}{d}\arccos\left(1 - \frac{[m^2 - (\Delta_S - \Delta_D)^2]}{2\Delta_S\Delta_D}\right) . \tag{2.25}$$

The phase diagram in Fig. 2.5 shows the different phases which occur for a given relation of m, Δ_S and Δ_D. If the mass $|m|$ is smaller than $m_1 = |\Delta_S - \Delta_D|$ the phase represents an ordinary insulator. When the mass surpasses this critical value and stays smaller than $m_2 = |\Delta_S + \Delta_D|$, where the phase turns into the 3D QAH insulator, the WSM phase is reached. At the lower critical mass m_1 two Weyl nodes at the edge of the BZ move towards each other until they annihilate at the upper critical mass m_2. These non-degenerate Weyl nodes originate from a degenerate Dirac node. The anomalous Hall conductivity of a 3D WSM depends on the separation k_0 of the nodes. As shown in Fig.2.5, these nodes arise from a QAH insulating phase which has an integer Hall conductivity. On the other hand, the mass vanishes at the Dirac nodes. Therefore, the contribution of a 2D Hall

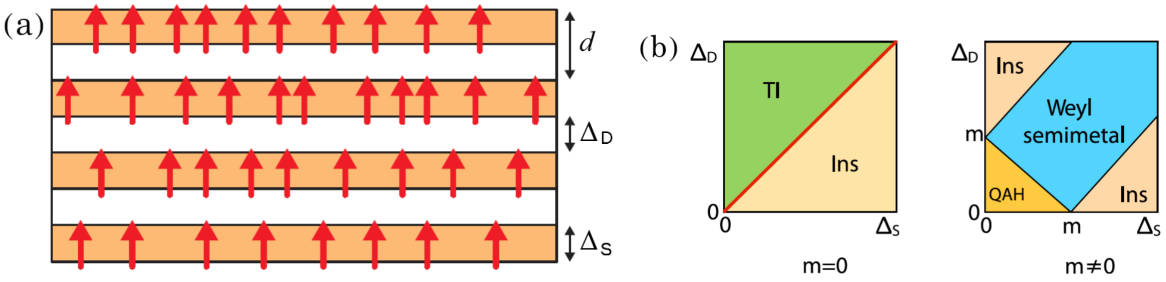

Figure 2.5: (a) WSM heterostructure composed of TI layers (orange) with tunneling Δ_S and ordinary insulator layers with tunneling strength Δ_D. The superlattice period is given by d. Adapted from Ref. [56]. (b) Phase diagrams with $m = 0$ and $m \neq 0$. Adapted from Ref. [13].

conductivity must contribute whenever the momentum k_z in Eq.(2.25) is between the Weyl nodes. Hence, the anomalous Hall conductivity yields

$$\sigma^{xy} = \frac{e^2 k_0}{\pi h} \tag{2.26}$$

and one finds $k_0 = \pi/d$ at the critical mass m_2 where the phase changes into the QAH insulator.

Toy model

A Hamiltonian describing a WSM requires a broken symmetry. Hence, $\mathcal{T}$- or $\mathcal{P}$-symmetry are broken. While $\mathcal{T}$-symmetry implies that a Dirac cone splits into at least two Weyl cones of opposite chirality, a WSM with broken $\mathcal{P}$-symmetry will provide at least four Weyl points. Since inversion only reverses the momentum but keeps the chirality, two Weyl cones with opposite chirality are needed to fulfill the Nielsen-Ninomiya theorem [55]. Therefore, a WSM with broken $\mathcal{P}$-symmetry will appear with a number of Weyl cones that is a multiple of four. A Hamiltonian which preserves $\mathcal{P}$-symmetry, yields

$$H(\mathbf{k}) = t_z(2 - \cos(k_x a) - \cos(k_y a) + \gamma - \cos(k_z a))\tau_z + t_x \sin(k_x a)\tau_x + t_y \sin(k_y a)\tau_y \tag{2.27}$$

where $t_{x,y,z}$ are the hopping amplitudes and $\tau_{x,y,z}$ are defined for the pseudospin orbital degrees of freedom and τ_z keeps the $\mathcal{P}$-symmetry. If $\cos(k_z a) = \gamma$ with $\gamma = \pm 1$, one finds Weyl nodes at the momentum $\pm\mathbf{k}_0 = (0, 0, \pm k_0)$. The Chern number which is $N = 1$ at $k_z = 0$ vanishes as the Weyl nodes move towards each other and annihilate. This happens at $\gamma = -1$, i.e. at the boundary of the BZ where $k_z = \pi/a$. Thus, the Weyl nodes occur at $\gamma = -1$ and annihilate again $\gamma = +1$ [57, 70, 71].

Based on the model of Fu, Kane and Mele describing a 3DTI, a $\mathcal{P}$-breaking WSM can be considered as a phase transition between weak and strong TIs. In a $\mathcal{T}$-symmetric WSM Kramers' degeneracy is lifted since the level-repulsion is reduced. Hence, the band inversion in a 3DTI at the Dirac point is not given anymore. On the other hand, the nodes move apart as a pair of monopoles and antimonopoles. Changing parameters, these two can be brought together again [72].

2.4.2 Chiral anomaly

One of the interesting consequences of the WSM topology is the chiral anomaly. Massless relativistic fermions obey the conservation of chiral charge which follows from the massless Hamiltonian that commutes with the γ_5 matrix. As discussed in Sec.2.1.2, the γ_5 matrix acts as a chirality operator and the chirality is an eigenvalue of the γ_5 matrix. However, the chiral charge is not conserved anymore, as an electromagnetic field is applied to the system. Classically, the chiral current is expected to vanish in such that the difference of the number of right- and left-moving fermions vanishes [40]. The violation of the conservation law which requires the electric and the chiral charge to be conserved both, corresponds to the Adler-Bell-Jackiw anomaly. It implies that in a gauge invariant system the axial current is not conserved [73–75]. The anomalous nonconservation leads to the axial current

$$\partial_\mu j_5^\mu = \frac{e^2}{16\pi^2}\epsilon^{\mu\nu\alpha\beta}F_{\mu\nu}F_{\alpha\beta} = \frac{e^2}{2\pi^2}\mathbf{E}\cdot\mathbf{B} \tag{2.28}$$

where $F_{\mu\nu}$ and $F_{\alpha\beta}$ represent electromagnetic tensors [56]. Furthermore, it also appears in the Landau level. Thus, it can be shown, that the difference of right- and left-moving fermions will lead to the same anomaly [56,75]. Moreover, the chiral anomaly contribution to the charge current yields

$$j^\nu = \frac{e^2}{2\pi^2}b_\mu\epsilon^{\mu\nu\alpha\beta}\partial_\alpha A_\beta \tag{2.29}$$

with electromagnetic gauge field A_μ, $\epsilon^{\mu\nu\alpha\beta}$ is the totally antisymmetric tensor with $\epsilon^{0,1,2,3} = +1$ and the chiral gauge field is given by $b_\mu = (b_0, -\mathbf{b})$. Even though the total charge is conserved in the system, imbalance of chirality can provide that the electric charge is not conserved. In the following, the two topological effects that follow from Eq.(2.29) will be discussed. The one, that depends on the spacial components of the gauge field, is the QAH effect which was already mentioned above. The second one is the chiral magnetic effect and depends on the temporal part b_0.

Quantum anomalous Hall effect

A 3D QAH insulator occurs from stacking layers of 2DTIs [58]. A 2DTI has broken $\mathcal{T}$-symmetry which is given in the WSM as well. Eq.(2.14) represents a two dimensional Dirac Hamiltonian with a half-integer quantum Hall conductance. The anomaly occurs, when the mass vanishes. Chiral massless fermions obey the previously presented chiral anomaly which leads to a chiral current contribution. The charge contribution in Eq.(2.29), follows from the action

$$S_\theta = -\frac{e^2}{8\pi^2}\int dtd^3r\ \partial_\mu\theta\epsilon^{\mu\nu\alpha\beta}A_\nu\partial_\alpha A_\beta \tag{2.30}$$

where $\partial_\mu\theta$ corresponds to the chiral gauge field $-b_\mu$ with $\mu = 1,2,3$. The current in Eq.(2.29) is nonconserved and follows from the chiral anomaly. This current, however, leads to the anomalous Hall effect (AHE) with conductivity

$$\sigma^{xy} = \frac{e^2|\mathbf{b}|}{\pi h} \tag{2.31}$$

which for $|\mathbf{b}| = k_0$ equals Eq.(2.26). This equation states that the chiral anomaly has an impact on the Hall conductivity. Therefore, the AHE has a topological origin.

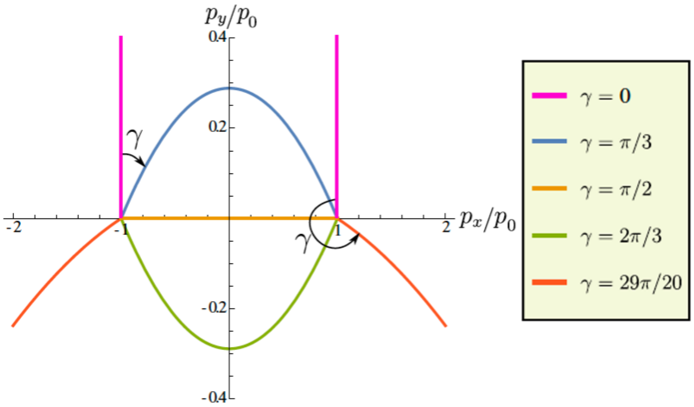

Figure 2.6: Fermi arc in WSM for half space geometry for different parameterizing angle γ. A flat surface arc exists for $\gamma = \pi/2$. This figure is adapted from Ref. [35].

Chiral magnetic effect

Another peculiar aspect that follows from chiral anomaly is the chiral magnetic effect (CME). The CME arises from an energy difference between the Weyl nodes. This energy difference can be provided by an external magnetic field which can be applied for instance according to the multilayerstrucure in Fig.2.5 perpendicular to the layers. In linear response theory the order of taking the limits can lead to different results. A further discussion will be given in Sec.2.8.1. The CME arises if the limit of small momenta of the response function that results from the action in Eq.(2.30) is taken first. The limit of small momenta corresponds to a time-dependent magnetic field which leads to a non vanishing response in the low-frequency limit. Changing the order of the limits, the current will vanish. This response, however, implies a static vector potential and additional contributions from intra-Landau-level processes let the response vanish. Hence, the CME can be interpreted as an response to a time-dependent magnetic field in dc limit [76].

2.4.3 Fermi arcs

The most interesting aspect about WSMs is the existence of the Fermi arc states, although the WSM has gapless bulk states. In Sec.2.3, the surface states of band insulators were discussed. To get a better understanding of surface states in a WSM, one can define a surface BZ (sBZ) which implies translational invariance and one assumes surface states are well defined everywhere except at the Weyl points. As mentioned the Weyl nodes act as monopoles to the Berry flux. Integration over a surface will then yield a Chern number. As long as the momenta are in between the Weyl nodes at Fermi energy $E_F = 0$, the Chern number of the 2D plane yields $C = 1$. Another interesting aspect is that, if the surface is parallel to the Weyl node separation in the sBZ, the Fermi arc imposes a flat line at $E_F = 0$ [57].

Witten proposed another boundary condition for Weyl fermions [35,38]. While the Dirac fermion imposes both helicities, the Weyl fermion has only one. Therefore, the angular momentum in general is not conserved at the boundary. Witten considered a boundary condition with a rotation matrix taking into account an angle γ. The angle γ ensures a vanishing current at the boundary and depends on the band structure as well as the material [35]. Hence, the set of wave functions will impose edge localized states decaying

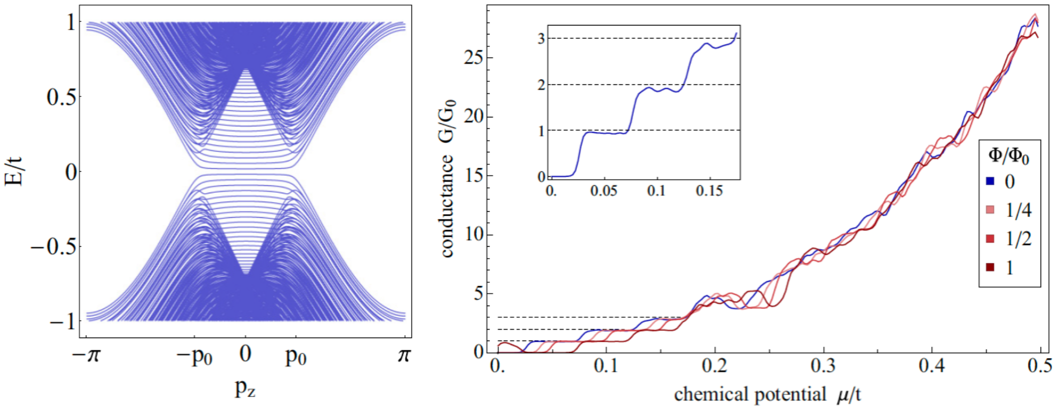

Figure 2.7: Left: Band structure of a cylindrical WSM nanowire with infinite mass boundary condition, i.e. open boundary condition, and energy in units of the hopping amplitude t. Right: Numerical conductance in dependence of the chemical potential μ/t of a Weyl semimetal nanowire with a magnetic field treading the wire. Thermal broadening with $T = 23\,\mathrm{K}$ was included. The inset represents a close up of the conductance steps at low chemical potential. Both figures are adapted from Ref. [24].

at the boundary. Moreover, these states form a Fermi arc. The Fermi arc breaks down at the Weyl nodes. However, the Nielsen-Ninomiya theorem implies that the Fermi arc has two endings of opposite chirality, if the Weyl nodes do not project to same momentum in the sBZ. A further insight to the boundary condition for a nanowire will be given in chapter 4.

The latter boundary condition in half space geometry was studied by Burrello *et al.* [35]. Therefore the eigenstates $\psi(\mathbf{r})$ have to fulfill

$$(\sigma_x \cos\gamma + \sigma_y \sin\gamma)\psi(\mathbf{r})|_{z=0} = \psi(\mathbf{r})|_{z=0} \tag{2.32}$$

with a parameterizing angle γ. The $\mathcal{T}$-breaking model Hamiltonian similarly to Eq.(2.27) contains Weyl nodes split in p_x-direction and located at $\pm p_0 \hat{e}_x$. As mentioned, the boundary condition defined at $z = 0$ preserves a vanishing current at the boundary. Fig.2.6 shows the Fermi arc form for different angle γ with respect to the distance p_x between the Weyl nodes. An important feature are the flat Fermi arcs, that appear at $\gamma = \pi/2$. This represents the infinite mass boundary condition which assumes that the mass becomes infinitely large beyond the boundary of the system. The boundary at $\gamma = \pi/2$ also corresponds to the minimum length of Fermi arcs. The rich band structure of WSM, especially regarding the Fermi arcs, leads to interesting consequences in transport properties that are presented in the following.

Transport in Weyl semimetals

In WSM nanowires, infinite mass boundary condition provides the flat Fermi surface arcs [24, 25]. Furthermore, a small surface gap of size $\sim v/(2\pi R)$ and a bulk gap with $\sim v/(2R)$ exist for a cylindrical nanowire. Fig. 2.7 shows the band structure in a cylindrical nanowire. For very low energies, one finds only surface states. Increasing $|E|$, bulk and surface states coexist. Thus, the fact that bulk and surface states can coexist has an impact on the conductance which increases in steps of conductance quanta, first. Reaching the bulk states, the conductance steps vary. This behavior is represented in Fig.

2.7. The numerical evaluation was done applying the KWANT-package[2] and the chemical potential is given in units of the hopping amplitude. Thus, the interest arises how the parameterized boundary condition affects the band structure of a nanowire. Chapter 4 addresses a nanowire under the boundary condition by Witten and presents the effect on transport for certain forms of the Fermi arc.

The direction of the magnetic field with respect to a WSM nanowire affects the conductance. This has been studied in Ref. [26] for nanowires with Weyl-node dispersion perpendicular to the direction of the wire length. While the conductance corresponds to the Landauer-Büttiker conductance (s.Sec.2.8.3) for zero magnetic field, an applied magnetic field parallel to the wire leads to the emergence of the zeroth Landau level. This results in an increase of the conductance. However, the surface states are perpendicular to the wire length as well as the magnetic field and thus barely affected. This is different for a magnetic field applied perpendicular to the wire axis and the separation of the Weyl nodes. There, the conductance reduces due to the flat-bands occurring from the increase of the magnetic field and hybridization of the surface modes.

The surface states act different to the bulk states on the dc-conductivity.The longitudinal dc-conductivity in WSM nanowires has been determined by Kubo linear response theory (s.Sec.2.8.1) in Ref. [25] for a Weyl-node separation parallel to the wire axis. The band structure follows from the infinite-mass boundary condition leading to the flat bands. The electric charge density shows that the flat-band provides a diverging charge density at the boundary of the wire, where $r \to R$. Bands with two local extrema presented a larger density near the origin of the wire. Similar results are obtained for the dc-conductivity, i.e. the contributions by flat bands dominate at the boundary, while the bands with local extrema contribute mainly at the origin.

The interesting band structure of WSMs allows for the study of the band shapes according to the parameterized boundary condition. Further, the two types of states affect the conductance in different ways. Hence, the question arises, whether and how different shapes of Fermi arcs act on the conductance. This case will be presented in chapter 4. Chapter 4 presents the study of the magnetoresistivity applying the parameterized boundary condition to a WSM nanowire according to Ref. [78].

2.4.4 Materials

The search for materials imposing WSM phases was cumbersome. The realization of $\mathcal{P}$-symmetry breaking candidates seemed more likely since *ab initio* calculations were much easier. Also, earlier research served a huge groundwork of experiments where inversion breaking materials were found [15]. Although $\mathcal{P}$-symmetry breaking materials were more likely to be found, the first proposed materials were presented by Wan *et al.* who suggested magnetic pyrochlore iridates $R_2Ir_2O_7$. These $\mathcal{T}$-breaking materials were composed of tetrahedral Iridium sublattices and a rare-earth-element R.

Nonetheless, their realization was difficult, especially since the crystal growth was challenging. The next proposal was the multilayer heterostructure by Burkov and Balents [13]. However, difficulties arose in preparation of the layers which had to be very thin. The multilayer structure was followed by the well known topological insulator, HgTe. The idea of Bulmash *et al.* was doping the 3DTI with Cd in order to provide magnetic order. Also, Xu *et al.* proposed $HgCr_2Se_4$ with magnetic order provided by Cr. Both proposals

---

[2] s.Ref. [77]

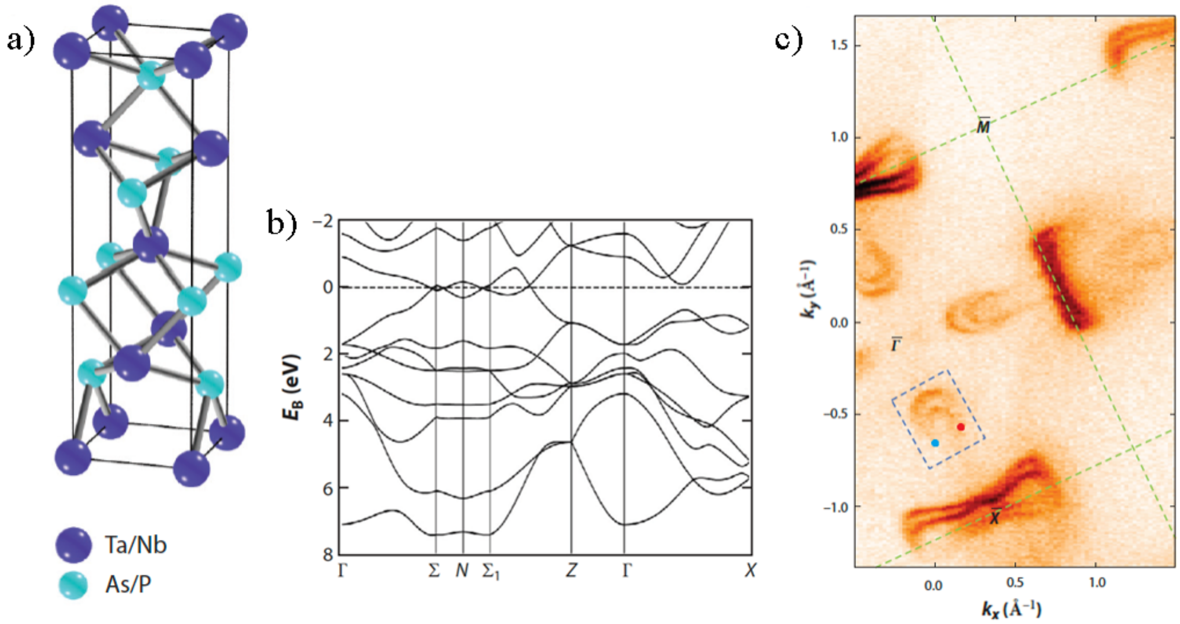

Figure 2.8: (a) WSM TaAs with lattice constants $a = 3.437$ Å and $c = 11.656$ Å. Adapted from Ref. [79]. (b) Band structure obtained by first-principle calculations. At $E_B = 0$ two crossings appear. Adapted from Ref. [15]. (c) Surface-sensitive ARPES measurements showing Fermi arc states. Adapted from [15].

had inefficient ARPES measurements.

In 2014, the Princeton group and the IOP group independently discovered the WSM structure in TaAs [14–17, 80]. ARPES measurements confirmed the existence of Fermi arcs and the nonzero Chern number. TaAs is an $\mathcal{P}$-symmetry breaking WSM with a body-centered tetragonal lattice structure and belongs to the $I4_1md$ (109) space group. Fig.2.8 shows the first-principle band structure of TaAs where due to the breaking of $\mathcal{P}$-symmetry the bands are degenerate at the Kramers points, if SOC is turned on [15]. Using soft X-ray measurements the bulk states were observed to disperse linearly at specific points. These points are the Weyl nodes. Surface sensitive ARPES measurements showed the bowtie-shaped structure in Fig.2.8 which represents a Fermi arc and agrees with the *ab initio* calculations. The Chern number can also be defined by Fig.2.8. The red and blue dot represent the edge states. There are two of each chirality at the Fermi level which corresponds to a net chirality of +2 and stays in agreement with the Chern number for a tube which encloses two points of same chirality [15].

The two sections have shown that although TIs and WSMs have common topological background, their topological properties and thus also their band structure are of different nature. This of course has impact on transport properties, like for instance the coexistence of bulk and surface states in a WSM nanowire. The following sections discuss the mathematical methods that are applied in the following chapters. Beyond mathematical methods, the following sections also address phonons and electron-phonon interaction. Electron-phonon interaction at low-temperature implies the excitation of low-energy phonons affecting the system. This is of large interest considering transport properties. Therefore, two ways of deriving the conductance of a system are represented in the last section of this chapter.

2.5 Green's functions

2.5.1 Time-ordered Green's Functions

For a better understanding of the electron-phonon coupling, the electron Hamiltonian will be discussed first. Based on the Hamiltonian, the particles can be described by Green's functions. Green's functions are useful to solve problems involving a perturbation, like for instance phonon-interaction. It is proportional to the inverse of the Hamiltonian including perturbations and can be utilized to solve the Schrödinger equation. Moreover, there are different types of Green's functions. Retarded and advanced Green's functions describe particles in a later or earlier state respectively. Green's functions at nonzero temperature can be computed in imaginary time very well, since one can introduce the perturbation together with the Hamiltonian. This type is called the Matsubara Green's function. In the following, the non-interacting electron Hamiltonian and the Green's function will be presented. Based on the single particle Green's function the two-particle correlation function will be defined.

The behavior of a non-interacting free electron can be described by

$$H = \sum_{\lambda} \epsilon_{\lambda} c_{\lambda}^{\dagger} c_{\lambda} \tag{2.33}$$

where λ denotes the quantum numbers, like for instance a momentum $\mathbf{k}$ and ϵ_{λ} is the energy in momentum space. The fermion operators describe the creation (annihilation) of a fermion $c_{\lambda}^{\dagger}$ (c_{λ}) with anti-commutation relation $[c_{\lambda_\mu}, c_{\lambda_\nu}^{\dagger}]_{+} = \left\{c_{\lambda_\mu}, c_{\lambda_\nu}^{\dagger}\right\} = \delta_{\lambda_\mu,\lambda_\nu}$ [30]. Then, the retarded Green's function describing a fermion yields

$$G_{\mathrm{ret}}(\lambda, t - t') = -i\Theta(t - t') \left\langle [c_{\lambda}(t) c_{\lambda}^{\dagger}(t')]_{+} \right\rangle \tag{2.34}$$

with time t where t' denotes system in the earlier and t the later time. At $V = 0$ one finds the unperturbed Green's function $G^{(0)}(\lambda, t - t')$. Fourier transformation leads to

$$G^{(0)}(\lambda, E) = \frac{1}{E - \epsilon_{\lambda} + i\delta} \tag{2.35}$$

where $i\delta$ is infinitesimal and prevents divergence in case that $E \to \epsilon_{\lambda}$ [30, 34]. Temperature dependence is included within the correlation of free fermions that corresponds to the Fermi-Dirac distribution, i.e. $\left\langle c_{\lambda}^{\dagger} c_{\lambda} \right\rangle = n_F(\epsilon_{\lambda})$. A perturbation can affect the temperature. However, introducing a perturbation for instance as a scalar potential into the Green's function becomes more convenient, switching to imaginary time $t \to i\tau$. The temperature dependence T in $\beta = 1/T$ can be treated as imaginary time defining the range of τ, where $-\beta < \tau < \beta$. For fermions, the Mastubara frequency is $\omega_n = (2n + 1)\pi/\beta$ following from the poles of the Fermi-Dirac distribution. The Matsubara Green's functions are defined as

$$\mathcal{G}_0(\mathbf{k}, i\omega_n) = \frac{1}{i\omega_n - \epsilon_{\mathbf{k}}} \tag{2.36}$$

where $\mathbf{k}$ is the momentum and $i\omega_n$ the Matsubara frequency [30, 34]. The connection between real and complex Green's functions lies within the Matsubara frequency $i\omega_n$, where analytic continuation yields $i\omega_n \to E + i\delta$. Thus, one returns back to the retarded Green's function. For $i\omega_n \to E - i\delta$ one obtains the advanced Green's function.

The correlation between two particles can be described by the correlation function. The correlation function is basically a two-particle Green's function. However, instead of observing single points one observes the correlation within a range [81]. It is fundamental for the Kubo formula in Sec.2.8.1. The two-particle correlation function consists of two-particle operators, for instance a charge operators. A correlation function in imaginary time is defined as

$$\mathcal{C}_{AB}(\tau,\tau') = -\left\langle \mathcal{T}_\tau[A(\tau)B(\tau')]\right\rangle \tag{2.37}$$

where $A(t)$ and $B(t)$ are fermionic two-particle operators with imaginary time-ordering operator $\mathcal{T}_\tau$

$$\mathcal{T}_\tau[A(\tau)B(\tau')] = \theta(\tau-\tau')A(\tau)B(\tau') - \theta(\tau'-\tau)B(\tau')A(\tau) \tag{2.38}$$

which sets the time τ on the left side, if $\tau - \tau' > 0$. As the name reveals, the time-ordering operator arranges the fermions with respect to time. Therefore, the sooner time is sorted to the right side. Furthermore, regarding Wick's theorem, each paring of creation and annihilation operators has to fulfill the ordering. The Matsubara Green's function is periodic in β. Fourier transformation changes the time-dependence into a frequency dependence. As mentioned, the Matsubara frequency is connected to the frequency in real correlation functions. Moreover, the Matsubara frequency is defined as $\omega_n = (2n+1)\pi/\beta$ for fermions and depends on temperature itself.

A huge advantage of the Matsubara Green's function is that computation of interactions by summing over frequencies becomes much easier in complex analysis. A frequency sum can be described as a contour integral. Then, integration over a contour with poles given by the Green's function, will yield a sum of residues. One can consider a charge-charge correlation function involving two many-particle operators $c^\dagger_{\mathbf{k}+\mathbf{q}}(\tau)c_{\mathbf{k}}(\tau)$ and $c^\dagger_{\mathbf{k}'}(0)c_{\mathbf{k}'-\mathbf{q}}(0)$ with momentum $\mathbf{k}$. The time-ordering operator will move all fermions with $\tau' = 0$ to the right hand side and according to Wick's theorem the fermions will split into pairings. Each pairing will then correspond to a single-particle Green's function. The result is a sum over a product of Green's functions that can be solved in frequency space by the residue theorem leading to

$$\frac{1}{\beta}\sum_{ik_n}\mathcal{G}_0(\mathbf{k}+\mathbf{q}, ik_n + i\omega_n)\mathcal{G}_0(\mathbf{k}, ik_n) = \frac{n_F(\epsilon_{\mathbf{k}}) - n_F(\epsilon_{\mathbf{k}+\mathbf{q}})}{i\omega_n + \epsilon_{\mathbf{k}} - \epsilon_{\mathbf{k}+\mathbf{q}}} \tag{2.39}$$

where $n_F(\xi_{\mathbf{p}})$ is the Fermi-Dirac distribution [30, 34].

2.5.2 Path Integral

The path integral connects classical physics to quantum mechanics. Its origin lies within the Gauss-integral derived by J. Gauss [81]. The idea is to integrate an exponential function with quadratic argument. This can also be done in more than one dimension. The generalized complex multidimensional integral then takes the form

$$\int d\left(\mathbf{v}^\dagger, \mathbf{v}\right) e^{-\mathbf{v}^\dagger \mathbf{A}\mathbf{v} + \mathbf{w}^\dagger\cdot\mathbf{v} + \mathbf{v}^\dagger\cdot\mathbf{w}'} = \pi^N \det \mathbf{A}^{-1} e^{\mathbf{w}^\dagger \mathbf{A}^{-1}\mathbf{w}'} \tag{2.40}$$

where $\mathbf{A}$ is a complex matrix and $\mathbf{v}$, $\mathbf{w}$ and $\mathbf{w}'$ are complex N-component vectors. The differential is a product over N-dimensions with $\int d\left(\mathbf{v}^\dagger, \mathbf{v}\right) = \prod_{i=1}^N d\mathrm{Re}v_i\, d\mathrm{Im}v_i$. The Gaussian functional integral can be evaluated similarly. Therefore, the differential denotes a functional and the elements of **A** become propagators. The connection between classical and quantum mechanics appears solving the partition function. Switching to imaginary time $t \to -i\tau$, one finds analogies between the partition function and the path integral. The Feynman path integral follows the idea to integrate an amplitude over N-dimensions, where N actually defines the number of time-steps. In other words, one divides the integral into N classical parts corresponding to a time-slice Δt. Moreover, the path integral of a Hamiltonian can be described by

$$\left\langle q_i \left| e^{-\frac{i}{\hbar}\hat{H}t} \right| q_j \right\rangle = \int_{q_i=q(t),q_j=q(0)} D(p,q) \exp\left(\frac{i}{\hbar}\int_0^t dt'(p\dot{q} - H(p,q))\right) \tag{2.41}$$

where $D(p,q)$ is the integration measure of infinite dimension, q defines the position and p the momentum. The path integral can be extended to a functional field integral involving coherent states. Coherent states are eigenstates of the annihilation operator. The identities of coherent states including their completeness leads to the representation as Grassmann variables. The Grassmann Gaussian integral

$$\int d\left(\bar{\phi},\phi\right)\; e^{-\bar{\phi}^T \mathbf{A}\phi + \bar{\mathbf{v}}^T\cdot\phi + \bar{\phi}^T\cdot\mathbf{v}} = \det\;\mathbf{A} e^{-\bar{\mathbf{v}}^T\mathbf{A}\mathbf{v}} \tag{2.42}$$

is again a generalization of a multidimensional Gaussian integral focusing on Grassmann fields ϕ and $\bar{\phi}$. The partition function can be expressed as a Grassmann Gaussian integral in terms of coherent states as well. Hence, the path integral of the partition function yields

$$\mathcal{Z} = \int D(\bar{\psi},\psi) e^{-S[\bar{\psi},\psi]}\;, \tag{2.43}$$

$$S[\bar{\psi},\psi] = \int_0^\beta d\tau[\bar{\psi}\partial_\tau\psi + H(\bar{\psi},\psi) - \mu N(\bar{\psi},\psi)] \tag{2.44}$$

where $S[\bar{\psi},\psi]$ is the action, μ is the chemical potential and $N(\bar{\psi},\psi)$ is the particle number operator. The integration measure is $D(\bar{\psi},\psi) = \lim_{N\to\infty}\prod_{n=1}^N d(\bar{\psi}^n,\psi^n)$ with Grassmann fields $\bar{\psi}^n$ and ψ^n in frequency space. The Green's function $G(x,\tau) = \left\langle \psi^\dagger(x,\tau)\psi(0,0)\right\rangle$ of the Grassmann fields $\psi^\dagger(x,\tau)$ and $\psi(x,\tau)$ can be solved by

$$\left\langle \psi^\dagger(x,\tau)\psi(0,0)\right\rangle = \frac{1}{\mathcal{Z}}\int D(\psi^\dagger,\psi)\psi(x,\tau)^\dagger\psi(0,0)e^{-S[\psi^\dagger,\psi]}\;. \tag{2.45}$$

This procedure will be deepened in chapter 3, where the effective action will be used to solve the Green's function and the current-current correlation functions.

2.6 Tomonaga-Luttinger Liquid

The model of a Luttinger liquid was established by Haldane in 1981 based on the Tomonaga-Luttinger model. The idea is to reduce a system to a one dimensional problem. Although Fermi-Liquid theory follows a similar idea of treating single particles as free particles, it does not hold for one dimensional systems. This means, Fermi Liquid theory describes interacting particles by quasiparticle excitations. However, this description does not hold for small quasiparticle momenta in 1D, since single particle excitations are not well defined anymore. Hence, the Luttinger liquid describes excitations by density-waves instead

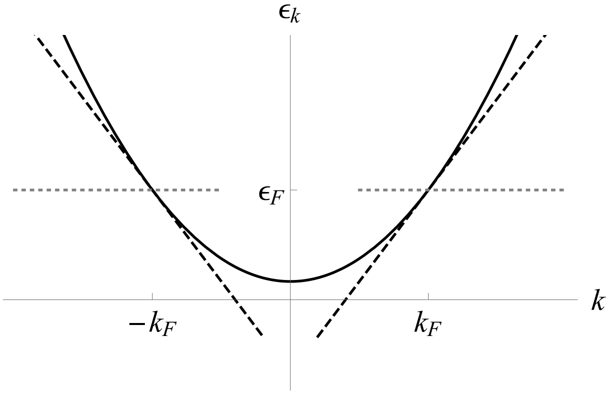

Figure 2.9: Electronic dispersion of a one-dimensional fermion. The dashed lines represent the linearized dispersion around the Fermi points $\pm k_F$. The dotted line shows the Fermi energy ϵ_F. Adapted from Ref. [30], [84] and [32].

of quasiparticles. In 1D, the excitations are not well-defined for quasiparticles. Examples for one dimensional systems with Luttinger Liquid behavior are for instance carbon nanotubes or semiconductor wires [82, 83]. The model of a TI nanowire, that will be discussed in chapter 3, can be treated as a 1D system along the wire axis [19]. As represented in Fig.2.9, the dispersion of a Hamiltonian as in Eq.(2.33) is linearized in the Tomonaga-model which restricts the applicability as long as the linearization holds. Luttinger extented the model including all real momenta in form of a linearized dispersion. The electrons are split in left- and right-moving parts contributing to left- and right moving densities respectively [30, 34, 82].

As already mentioned, the Hamiltonian can be described with this kind of 1D-model. A particularly new method in conformal field theory and especially regarding Luttinger liquids is bosonization. The behavior of particle-hole excitations in one dimension can be treated bosonic. Jordan-Wigner transformation implies that a fermion can be expressed by bosonic operators. These bosonic operators depend on the charge ρ and a phase field φ with the commutator $[\rho(x), \varphi(x')] = i\delta(x - x')$ [81, 85]. One can define the field $\theta(x) = \pi \int_{-\infty}^{x} dx' \rho(x')$ and replace the charge in the bosonic operator by the derivative of that field. The fermion operator follows from the bosonized Hamiltonian $H = H_0 + H_{int}$, where the non-interacting part

$$H_0 = v_F \sum_{q>0} q(a_q^\dagger a_q + b_q^\dagger b_q) \tag{2.46}$$

follows from the non-interacting Hamiltonian in Eq.(2.33) and v_F is the Fermi velocity that occurs from the linearized dispersion $\epsilon_k \approx (\pm k - k_F)v_F$. The Hamiltonian is expressed in terms of bosonic annihilation (creation) operators a_q and b_q ($a_q^\dagger$ and $b_q^\dagger$) which follow boson commutation relations, i.e. $[a_\mu, a_\nu^\dagger] = [b_\mu, b_\nu^\dagger] = \delta_{\mu,\nu}$. They describe the density operators $\rho_{L,R}(q)$ of left- and right-moving fermions. These density operators define the functional fields. Moreover, one finds the non-interacting Hamiltonian in terms of functional fields

$$H_0 = \frac{1}{2} v_F \int dx \ \left((\partial_x \theta)^2 + (\partial_x \varphi)^2 \right) \ . \tag{2.47}$$

If spin is involved in interactions, the phase field can be expressed by two components, i.e. the spin component φ_s and the charge component φ_c. In this case, the Hamiltonian can written as a sum over those fields. Interactions can be included in the bosonized model by bosonization of the interaction Hamiltonian. The electron-electron interaction in terms of fermion creation and annihilation operators is given by

$$H_{int} = \frac{1}{2} \sum_{k,k',q} V(q) c^{\dagger}_{k+q} c^{\dagger}_{k'-q} c_{k'} c_k \tag{2.48}$$

where $V(q)$ denotes a potential due to the interactions and k, k', $k+q$ and $k-q$ are fermion momenta near the Fermi points [86]. The interaction can lead to various scattering processes, for instance forward- and backscattering as well as Umklapp scattering [19,32, 84,87]. Furthermore, the effects of interaction can be stored with a interaction parameter K, that yields

$$K = \frac{1}{\sqrt{1 + \frac{V_0}{\pi v_F}}} \tag{2.49}$$

where V_0 is the Fourier transform of the interaction potential without including spin degrees of freedom. Then, the bosonized Hamiltonian is given by

$$H = \frac{\tilde{v}}{2} \int dx \, \left(K(\partial_x \theta)^2 + \frac{1}{K}(\partial_x \varphi)^2 \right) \tag{2.50}$$

including interactions with $\tilde{v} = v_F/K$ [19, 87]. The interaction parameter is a renormalization of the phase field φ. Including the spin, the interaction parameter $K_{\mu=c,s}$ renormalizes the charge and the spin component of the phase field respectively [84, 86]. Furthermore, these functional fields can be utilized to determine a bosonized form of the fermion operator. Expanding the fermion operator around the Fermi momentum k_F, one obtains the bosonized fermion operator

$$\Psi_{\pm}(x) = \Gamma \sum_{\nu=\pm 1} e^{i\nu k_F x} e^{-i\sqrt{\pi}[\varphi(x)+\nu\theta(x)]} \tag{2.51}$$

where $\Gamma = 1/(2\pi a)^{1/2}$ is a scalar prefactor which can be obtained solving the correlation function and $\nu = -1$ ($\nu = +1$) describes the right (left) mover [30,32,81]. The Lagrangian action can be expressed by those fields as well. In case of non-interacting electrons, it reads

$$S_0[\theta] = \frac{1}{2\pi} \int dx d\tau [v_F (\partial_x \theta)^2 + \frac{1}{v_F} (\partial_\tau \theta)^2] \, . \tag{2.52}$$

It is rotationally invariant and the fields impose a linear dispersion. Introducing the dual boson field leads to the relation $\partial_x \varphi = -(1/v) \partial_\tau \theta$.

An important approach for bosonization is solving Green's functions and correlation functions. One can consider a Green's function with the fermion described by the operator in Eq.(2.51). The Green's function then can be split into the left and right movers keeping the ordering. The expectation value of the functional field can be solved by the partition function [31]. Another advantage of the Tomonaga-Luttinger liquid model is the possibility to examine correlations. To be more precise, one focuses on the ordering of two-particle correlation functions. Moreover, it is an exactly solvable model [34]. The bosonic fermion operator allows to construct charge and spin density operators and also superconducting fluctuations. The orders of charge density waves and spin density waves are described by the two-particle correlation functions of charge and spin respectively. The superconducting order parameters follow from singlet or triplet superconducting paring. These

fluctuations can give information about possible phases in a system [31, 32, 81, 88].
The following chapter discusses a phase diagram of the TI nanowire. Since, the nanowire geometry allows for the approach of bosonization including Coulomb interaction, as shown in Ref. [19], one can compute the single particle Green's function describing the system and moreover, also the density fluctuations [31, 67]. The order parameter of the density fluctuations are then represented in a phase diagram.

2.7 Electron-phonon Interaction

Lattice vibrations can have various effects on a solid. Such quantized lattice vibrations are known as phonons. While electrons are fermion particles with a half-integer spin, phonons are of bosonic nature with integer spin. They follow other commutation rules and can interact with fermions. Phonon interaction can for instance lead to the deformation of a system. Furthermore, the movement of acoustic phonons sets in at a certain temperature called the *Bloch-Grüneisen*-temperature. Increasing with temperature, it can have significant impact on transport properties. This section addresses the electron-phonon coupling and is followed by two methods to evaluate the interaction, the Kubo formula and the Boltzmann equation.

2.7.1 Phonons

The electron-phonon-Hamiltonian consists in general of a non-interacting electron Hamiltonian, a phonon-Hamiltonian and an interaction Hamiltonian. The electron Hamiltonian is described by Eq.(2.33). Phonons are quantized oscillations in a chain of ions. They move between the ions with momentum $\mathbf{p}_j$ and are located at a position $\mathbf{R}_j^0$ with a displacement $\mathbf{u}_j$. The Fourier transform of the displacement is given by

$$\mathbf{u}_{\mathbf{q}\lambda} = \sqrt{\frac{\hbar}{M\omega_{\mathbf{q},\lambda}}} \left(b^\dagger_{-\mathbf{q},\lambda} + b_{\mathbf{q}\lambda} \right) \xi_{\mathbf{q}\lambda} \; e^{i\mathbf{q}\cdot\mathbf{R}_j^0} \tag{2.53}$$

where $\xi_{\mathbf{q}\lambda}$ is the polarization vector, $\mathbf{q}$ is the phonon momentum and λ describes the phonon mode. Isotropic media, for instance, correspond to a polarization which is parallel or perpendicular to the phonon momentum. These oscillations are described in the lattice model by the harmonic oscillator in second quantization

$$H_{ph} = \sum_{\Lambda} \hbar\omega_\Lambda \left(b^\dagger_\Lambda b_\Lambda + \frac{1}{2} \right) \tag{2.54}$$

where $b^\dagger_\Lambda$ (b_Λ) is the bosonic creation (annihilation) operator with $\Lambda = \mathbf{q}, \lambda$ denoting the set of quantum numbers and Ω being the phonon frequency [30, 34]. The types of phonon differ in their excitation energies. At low energy one has mostly acoustic phonons, while at higher energies, like for instance light, optical phonons are excited. Phonons move with different velocities depending on the polarization which can be longitudinal, transverse or a general polarization. Longitudinal waves provide displacements in direction of propagation while transverse waves impose displacements perpendicular to the direction of their propagation. General modes can have properties of both. Another type of modes are *Rayleigh* waves which propagate along the surface and decrease as they enter the medium [66].

2.7.2 Electron-phonon coupling

Electron-phonon coupling is needed to describe the interaction between electrons and phonons. The general form of an electron-phonon interaction Hamiltonian is

$$H = H_e + H_{ph} + H_{el-ph} \tag{2.55}$$

where the first two terms were already described above. The last term defines the electron-phonon coupling and includes interactions between electrons and ions which for instance can be atoms. The lowest trivial order in displacement yields

$$V_{el-ph} = \sum_j \mathbf{u}_j \cdot \nabla V_{ei}(\mathbf{r} - \mathbf{R}_j^0) \tag{2.56}$$

where $\mathbf{r}_j$ describes the position of the electron and V_{ei} the (unscreened) electron-atom potential. The reciprocal lattice vectors enter as the sum over $\mathbf{G}$ through Fourier transformation of the phonon displacement. The summation over phonon momenta $\mathbf{q}$ has to be defined within the first BZ (FBZ). The potential can be obtained by estimating the phonon energies and polarizations for each mode. The electron-phonon Hamiltonian is described by the charge density $\rho(\mathbf{r})$ and the electron-phonon potential. The general form is given by

$$H_{el-ph} = \frac{1}{\mathcal{V}} \sum_{\mathbf{k}} \sum_{\mathbf{qG}\lambda} M_{\mathbf{q}+\mathbf{G},\lambda} c^\dagger_{\mathbf{k}+\mathbf{q}+\mathbf{G}} c_{\mathbf{k}} \left(b^\dagger_{-\mathbf{q},\lambda} + b_{\mathbf{q},\lambda} \right) \tag{2.57}$$

with

$$M_{\mathbf{q}+\mathbf{G},\lambda} = -V_{\mathbf{q}+\mathbf{G}}(\mathbf{q}+\mathbf{G}) \cdot \xi_{\mathbf{q}\lambda} \left(\frac{\hbar}{2\varrho\omega_{\mathbf{q}\lambda}} \right)^{1/2}$$

where ϱ is the mass density, $\xi_{\mathbf{q}\lambda}$ is the polarization vector, $V_{\mathbf{q}+\mathbf{G}}$ is the Fourier transform of V_{ei} and $\rho(\mathbf{q}) = \sum_{\mathbf{k}} c^\dagger_{\mathbf{k}+\mathbf{q}} c_{\mathbf{k}}$ the density operator. The matrix $M_{\mathbf{q}+\mathbf{G},\lambda}$ is the coupling-matrix. The electron-phonon coupling Hamiltonian describes a phonon that is emitted or absorbed by a scattering electron. Momentum and spin conservation are required within the FBZ. In low-energy theory, electron phonon interaction is usually provided by long wavelength phonons, for instance acoustic phonons [30,34]. In chapter 3, electron-phonon interaction is discussed within the low-energy theory. To determine the modes acting in the TI nanowire, isotropic elastic continuum is considered which allows to express the free energy by two constants describing the deformation. In the following, the free energy in crystals and the isotropic elastic continuum theory are addressed.

Isotropic elastic continuum theory

Phonon interaction provides a deformation of the medium. This deformation is given by deformation potentials. Depending on the medium the response on temperature and stress leads to different conditions for deformations. Elastic deformations imply weak deformations. Hence the medium keeps its original form after the deformation. An isotropic medium is defined by continuous symmetries. These are given by the equation of motion

$$0 = \partial_{x_k}\sigma_{ik} + \varrho\ddot{u}_i \tag{2.58}$$

where σ_{ik} is the stress tensor and $\varrho\ddot{u}_i$ is a force. Free energy is in general given by

$$F = \frac{1}{2}\lambda_{iklm} u_{ik} u_{lm} \tag{2.59}$$

in deformed crystals where $\sigma_{ik} = \lambda_{iklm} u_{lm}$. The deformation is described by the strain tensors u_{ik} and u_{lm} and λ_{iklm} is the tensor of elastic moduli, called the Young modulus. The Young modulus describes linear stress in form of a tensor respecting the symmetries of the crystal. A deformation in a crystal can be considered to be isotropic, if it is constructed as a polycrystalline of many significantly small crystallites [42, 66]. Furthermore, the free energy reduces to

$$F = \mu \left(u_{ik} - \frac{1}{3}\delta_{ik} u_{ll} \right)^2 + \frac{K}{2} u_{ll}^2 \tag{2.60}$$

where $K = \lambda + (2/3)\mu$ is the bulk modulus and λ and μ are the LAMÉ coefficients. In order to derive the modes that cause the lattice vibrations, the equation of motion (2.58) has to be solved for elastic waves according to the geometry of the medium. Given the boundary conditions for the stress, for instance stress-free boundary conditions, one obtains the modes given in the system. However, the coupling within the Hamiltonian determines the impact of the mode on the interaction [27, 28, 66].

The aspect, that phonon excitation already arises for low-temperatures in form of acoustic phonons, can in principle affect transport properties even at low-temperatures. However, electron-phonon interaction can also lead to Cooper instability and further to superconductivity [30]. Acoustic phonon interaction in TIs has been studied theoretically in thin film and half-space geometry [27, 28]. In chapter 3, the electron-phonon interaction in a TI nanowire will be discussed. The TI nanowire can be treated as a helical Luttinger liquid [19]. The bosonization approach then allows studying the effects of electron-phonon interaction including also electron-electron interactions.

2.8 Conductivity

Transport properties are of large interest in condensed matter. The scattering of electrons, phonons or other impurities can reduce the conductivity of a solid. Depending on the material, low-temperature resistivity can already occur for instance induced by phonons. This section presents two methods to derive the conductivity. The Kubo formula solves the conductivity in linear response. The other method is solving the Boltzmann equation. Both methods have their advantages regarding the studied system. In the following chapters both methods are represented for different purposes.

2.8.1 Kubo-formula

A very common method to compute the conductivity of a system, is the Kubo formula (1957) [89]. The Kubo formula considers a linear response to a perturbation similar as the linear response to a perturbation is measured in experiments. The perturbation can for instance be an applied external electric field. The Hamiltonian describing the system can also include various interactions. Chapter 3 will present such a conductivity including electron-electron and electron-phonon interactions in a TI nanowire.

Linear response theory in general considers a time-dependent Hamiltonian composed of an initial state in equilibrium and a time-dependent weak perturbation. The expectation values of states with time-dependent perturbation provide time-dependent expectation values. The linear order of the expectation value in perturbation then corresponds to a correlation function [30].

Linear response theory considers a linear order of the perturbation. One can consider a system with a time-dependent external electric field applied to it. Hence, the induced current is proportional to that external field. The conductivity follows from the total electric field, which composes from the external field and the fields induced by the external one. The current can be described by

$$J_\alpha(\mathbf{r},t) = \int d^3r' \int_{-\infty}^{t} dt' \sum_\beta \sigma_{\alpha\beta}(\mathbf{r},\mathbf{r}';t,t') E_\beta(\mathbf{r}',t') \tag{2.61}$$

where $\alpha = x, y, z$ and the electric field is given by $E_\beta(\mathbf{r}',t')$ [34]. The conductivity tensor $\sigma_{\alpha\beta}(\mathbf{r},\mathbf{r}';t,t')$ refers to a current response on the direction of the external field. The current then consists of two parts, one described only by the electric field, the other one by the expectation value of the current operator j_α. The non-vanishing terms of the second part are of linear order in perturbation. Thus, the expectation value of the current operator is proportional to the external electric field. Moreover, the conductivity is given by

$$\sigma_{\alpha\beta}(\mathbf{q},\omega) = \frac{1}{\omega v} \int_{-\infty}^{t} dt' e^{i\omega(t-t')} \left\langle \psi \middle| [j_\alpha^\dagger(\mathbf{q},t), j_\beta(\mathbf{q},t')] \middle| \psi \right\rangle + i\frac{n_0 e^2}{m\omega}\delta_{\alpha\beta} \tag{2.62}$$

where ω is the frequency, n_0 is the particle number, e the charge and m is the particle mass [34]. The conductivity defines the proportionality of the electric field in the expectation value. This is the Kubo formula for conductivity which depends on the current-current correlation function

$$\Pi_{\alpha,\beta}(\mathbf{q},\omega) = -\frac{i}{v} \int_{-\infty}^{\infty} dt\; e^{i\omega(t-t')} \Theta(t-t') \left\langle \psi \middle| [j_\alpha^\dagger(\mathbf{q},t), j_\beta(\mathbf{q},t')] \middle| \psi \right\rangle \; . \tag{2.63}$$

The dc-limit of a conductivity follows by letting the momentum $\mathbf{q} \to 0$ and afterwards setting $\omega \to 0$. This is crucial, since letting $\omega \to 0$, first, would imply a static field instead of a time-dependent field [34].

2.8.2 Boltzmann equation

The conductivity can also be computed by the Boltzmann equation. The connection to the Kubo formula was derived by Green. Nonetheless, for high-energy phonons the derivation from the Kubo formula will not provide the full Boltzmann equation describing the system. In low-energy theory with elastic scattering in isotropic media, the vertex corrections including inelastic scattering that are important to estimate the exact model can be neglected. Since the Boltzmann theory characterizes electrons by a classical distribution function, one finds the distribution function

$$0 = \frac{df}{dt} = \frac{\partial f}{\partial t} + \mathbf{v} \cdot \vec{\nabla}_\mathbf{r} f + \frac{\partial \mathbf{k}}{\partial t} \cdot \vec{\nabla}_\mathbf{k} f + \left(\frac{\partial f}{\partial t}\right)_{collisions} \tag{2.64}$$

changes in time according to the Boltzmann equation. The Boltzmann equation follows from the continuity equation, where the first and the last term describe the time derivative of the distribution function without and with collisions respectively and the divergence of the current is split into the second and third term [30]. In a homogeneous material, the gradient vanishes. The time rate of the distribution function for dc conductivity vanishes as well. The collision term yields

$$
\begin{aligned}
-\left(\frac{\partial f}{\partial t}\right)_{collisions} =& \frac{2\pi}{\hbar}\int_{\mathbf{q}} |M_{\mathbf{q}}|^2 f(\mathbf{p})[1-f(\mathbf{p}+\mathbf{q})] \\
& \times [(N_{\mathbf{q}}+1)\delta(\epsilon_{\mathbf{p}}-\epsilon_{\mathbf{p}+\mathbf{q}}-\hbar\omega_{\mathbf{q}}) + N_{\mathbf{q}}\delta(\epsilon_{\mathbf{p}}-\epsilon_{\mathbf{p}+\mathbf{q}}+\hbar\omega_{\mathbf{q}})] \\
& -\frac{2\pi}{\hbar}\int_{\mathbf{q}} |M_{\mathbf{q}}|^2 f(\mathbf{p}+\mathbf{q})[1-f(\mathbf{p})] \\
& \times [(N_{\mathbf{q}}+1)\delta(\epsilon_{\mathbf{p}}-\epsilon_{\mathbf{p}+\mathbf{q}}+\hbar\omega_{\mathbf{q}}) + N_{\mathbf{q}}\delta(\epsilon_{\mathbf{p}}-\epsilon_{\mathbf{p}+\mathbf{q}}-\hbar\omega_{\mathbf{q}})] \qquad (2.65)
\end{aligned}
$$

by applying relaxation time approximation which implies that a system pursues equilibrium [34]. This collision term represents electron-phonon interactions. Emission of a phonon is described by $(N_{\mathbf{q}}+1)$ and absorption of a phonon by $N_{\mathbf{q}}$ where $N_{\mathbf{q}}$ is the expectation value of the particle number for Bose-Einstein statistics. The transition probability is given by the matrix elements $|M_{\mathbf{q}}|$ due to electron-phonon coupling (s.Eq.(2.57)). The collision integral contains two scattering terms, one from state $\mathbf{p}$ to $\mathbf{p}+\mathbf{q}$ which is represented by the factor $f(\mathbf{p})[1-f(\mathbf{p}+\mathbf{q})]$ and the other into the opposite direction.

The collision integral can be used to compute transport properties. In the following, the Boltzmann equation will be utilized to solve the phonon-induced current correction [33]. Another approach will be shown in chapter 4 where the linearized Boltzmann eqaution will be applied to compute the phonon-induced resistivity [90].

2.8.3 Landauer conductance formula

In mesoscopic systems, electron transport can be studied in a coherent system. This allows for the definition of scattering states that characterize the transport. Assuming coherence lengths beyond the sample size, one can for instance consider a nanoscale device at low temperatures. A system can be treated as mesoscopic, if certain lengths of the system have particular sizes, i.e.

$$a_0 \ll \lambda_F \lesssim l_0 < \mathcal{L} < l_\phi \lesssim l_{in} \qquad (2.66)$$

where a_0 is the Bohr radius, λ_F the Fermi wavelength describing an electron, l_0 the elastic mean free path, $\mathcal{L}$ is the size of the sample, l_ϕ is the coherence length and l_{in} is the relaxation length of the energy [30]. The setup contains two electron reservoirs, on the left and right side thermalizing the electrons. The states of the mesoscopic sample in between will be filled by these electrons which enter through one of the N channels of the lead. The conductance derivation of such a setup is referred to as the two-probe *Landauer-Büttiker formalism.* The scattering states can then be solved in form of a $2N \times 2N$ scattering matrix (S-matrix) which composes of two reflection and two transmission matrices of size $N \times N$

$$\mathbf{S}(\epsilon) = \begin{pmatrix} \mathbf{r}(\epsilon) & \mathbf{t}'(\epsilon) \\ \mathbf{t}(\epsilon) & \mathbf{r}'(\epsilon) \end{pmatrix} \,. \qquad (2.67)$$

The matrix elements of the transmission and reflection matrices describe the transmission and reflection amplitudes respectively. The S-matrix is unitary and can be symmetric if $\mathcal{T}$-symmetry is present. The unitarity of the S-matrix allows the relation $\mathrm{Tr}[\mathbf{t}^{\dagger\prime}(\epsilon)\mathbf{t}'(\epsilon)] = \mathrm{Tr}[\mathbf{t}^{\dagger}(\epsilon)\mathbf{t}(\epsilon)]$. In terms of scattering states, one can then derive the Landauer conductance formula which describes a two-terminal conductance.Assuming completely thermalized electrons, the electrons correspond to the Fermi-Dirac distribution function. Their energy is defined by the chemical potential at the reservoir. The electrical current can be expressed in terms of the scattering states

$$I_e = \frac{e}{\pi} \int_0^\infty d\epsilon \mathrm{Tr}[\mathbf{t}^\dagger(\epsilon)\mathbf{t}(\epsilon)] \left[n_F(\epsilon - \mu + eV_L) - n_F(\epsilon - \mu + eV_R)\right] \tag{2.68}$$

where the trace appears from summing over diagonal elements and $V_{L,R}$ are the applied voltages. The current can be expanded in low voltage and temperature regime. Hence, one obtains the Landauer conductance formula

$$G(\mu, T) = \frac{2e^2}{h} \int_0^\infty d\epsilon \mathrm{Tr}[\mathbf{t}^\dagger(\epsilon)\mathbf{t}(\epsilon)] \left(-\frac{\partial n_F}{\partial \epsilon}\right) \xrightarrow{T\to 0} \frac{2e^2}{h} \mathrm{Tr}[\mathbf{t}^\dagger(\epsilon)\mathbf{t}(\epsilon)] \ . \tag{2.69}$$

At zero temperature the formula describes a conductance increasing in steps of $2e^2/h$ with increasing number of channels where e^2/h is the conductance quantum. The derivation in Kubo formalism leads to the same result. As this is beyond the scope of the thesis, the main ideas are briefly summarized in the following. The conductance in linear response implies a current-current correlation function. The correlation function can be solved in dc-limit. The current matrix elements will then provide the transmission probabilities in form of the trace over the transmission amplitudes. Thus, one arrives at the same equation as above [30, 33].

This chapter established the fundamental principles in this thesis. The following two chapters represent the study of electron-phonon interaction in a TI nanowire and in a WSM nanowire. The different topological nature of both materials has already been shown in this chapter. Moreover, the consequences of the different band structures will be discussed in the following chapters.

Chapter 3

Phase diagram and phonon-induced backscattering in topological insulator nanowires

Electron-phonon interaction has been examined in various materials and geometries. Moreover, phonon-induced effects have already been studied theoretically, for instance in TI thin films and half-space geometries [27, 28, 91–99]. In experiments, like for instance ARPES measurements, the temperature-dependent quasiparticle lifetime has been measured and transport properties have been evaluated [100–117]. Furthermore, the experiments on magnetotransport in TI nanowires are proceeding [20, 118–121].The coupling constant can be determined by measuring the quasiparticle lifetime of surface states. However, measurements of acoustic phonon coupling constants have led to very different results. The origin of the variety can only partially be explained by different experimental conditions.

The Dirac surface states of 3DTIs have been studied theoretically and experimentally since the last decade [8, 52, 53, 122]. In nanowires, the one-dimensional model of a helical Luttinger liquid has been established for the surface states [19]. This chapter addresses a cylindrical TI nanowire pierced by a magnetic flux Φ_B in units of flux quantum $\Phi_0 = hc/e$. The surface states are established first. Electron-electron interactions in Abelian bosonization approach are also taken into account based on the model derived in Ref. [19]. The surface states are followed by the acoustic phonons acting in an infinitely long cylindrical wire. Phonon-induced effects are considered to occur due to deformation potential coupling of acoustic phonons in isotropic elastic continuum theory. Transport properties like conductivity are evaluated applying the Kubo formula. A phase diagram will be evaluated in Sec. 3.4 for the case of half-integer magnetic flux presenting the order-fluctuations of density waves and superconducting paring in dependence of the interaction parameters describing the strength of electron-electron and electron-phonon interactions.

The last section addresses the phonon-induced resistivity slightly away from half-integer flux. This derivation follows without electron-electron interactions. The temperature dependence is obtained by the Boltzmann approach in Ref. [33]. The theoretical work will be compared to experimental investigations on ballistic transport in TI nanowires [20].

This chapter rests upon the included publication by Dorn *et al.* [67]. A lot of the content was reproduced here, since the publication has a pedagogical nature.

3.1 Electronic surface states

This section covers the electronic surface states in a TI nanowire including electron-electron interactions. The electron-electron interaction is described by the interaction parameter K of the helical Luttinger liquid established for helical Dirac fermions. At $K = 1$ no interactions are present, while for smaller K repulsive Coulomb interactions occur. Large K could be possible, taking into account gapped phonon modes.

3.1.1 Surface state Hamiltonian

The model for the low-energy electronic states of a cylindrical TI nanowire, is discussed at first. Typically, TI materials are characterized by a sizeable bulk gap of order $\Delta_b \simeq 0.3$ eV [7, 52, 53, 62, 123]. As long as the Fermi energy resides well within the bulk gap and provided that one has sufficiently clean materials to realize the ballistic transport regime, only surface states will be relevant for the low-energy transport properties. For a cylindrical wire of radius R, the electronic surface spectrum consists of massive 1D Dirac fermion modes with conserved momentum k along the cylinder axis ($\hat{e}_z$) [19, 22, 23, 65, 124–126]. The model discussed below includes an axial magnetic field B giving rise to the dimensionless flux $\Phi_B = \pi R^2 B/(h/e)$ piercing the nanowire. As mentioned in the previous chapter, the energy spectrum of a TI nanowire is gapped away from half-integer flux [19].

In cylindrical coordinates (r, ϕ, z), with unit vectors $(\hat{e}_r, \hat{e}_\phi, \hat{e}_z)$, the electronic single-particle Hamiltonian describing surface states with conserved momentum k is a Dirac Hamiltonian wrapped onto the cylinder surface [19, 65, 124],

$$\mathcal{H}_{\text{el}}(k) = e^{-i\phi\sigma_z/2}\left(v_1 k\sigma_y - \frac{v_2}{R}(-i\partial_\phi + \Phi_B)\sigma_z\right)e^{i\phi\sigma_z/2}, \tag{3.1}$$

with the Fermi velocities v_1 (v_2) along $\hat{e}_z$ (perpendicular to $\hat{e}_z$). The Pauli matrices $\sigma_{x,y,z}$ act in spin space. The dispersion relation of the 1D fermion modes is thus given by ($\pm$ refers to conduction and valence bands) [22, 124, 125]

$$E_{j,\pm}(k) = \pm\sqrt{v_1^2 k^2 + v_2^2 (j + \Phi_B)^2/R^2}. \tag{3.2}$$

Different bands are distinguished by the half-integer eigenvalue j of the conserved z-component of the total angular momentum operator.

For integer magnetic flux, a time-reversal ($\mathcal{T}$) transformation connects the states $(k, j + \Phi_B) \leftrightarrow (-k, -j - \Phi_B)$. Due to this emergent $\mathcal{T}$-symmetry, all states are arranged into doubly degenerate Kramers pairs. Elastic scattering between such pairs is forbidden by virtue of the Kramers theorem, as the overlap vanishes [19]. Nonetheless, $2k_F$ backscattering ($k \to -k$) for given j is allowed and there is no protection against elastic disorder effects. However, for *half-integer* magnetic flux, the emergent $\mathcal{T}$-symmetry now comes with a topological protection against weak spin-conserving backscattering. This is because for the special massless 1D Dirac mode with $j = -\Phi_B$, the two states with momentum $\pm k$ constitute a protected Kramers pair [22, 124–126]. While this scenario — a single Dirac fermion species protected by an emergent $\mathcal{T}$-symmetry — is ruled out for conventional systems by the Nielsen-Ninomiya theorem [53], it can be realized using the surface states of TI nanowires with half-integer flux Φ_B. The special mode with $j = -\Phi_B$ is protected against elastic disorder effects and dominates the physics on energy scales below the surface state gap $E_g \simeq v_2/R$. This is fundamental for the helical Luttinger liquid model of Ref. [19] which will be utilized in the following to describe the Dirac fermions. On higher energy scales, also other transverse bands with $j \neq -\Phi_B$ have to be included in the theory.

3.1.2 Bosonization approach

Nanowire geometries are usually suitable for bosonization approach since one can reduce the fermion propagation to a 1D problem [30]. As mentioned in the previous chapter, bosonization is a useful method to study a system including several interactions which can be described by interaction parameters. Low energies, $|E| \ll \Delta_g \equiv \min(E_g, \Delta_b)$, are considered throughout this chapter. Putting Φ_B to a half-integer value, only the gapless Dirac mode with $j = -\Phi_B$ and $E_\pm(k) = \pm v_1|k|$ remains relevant. The electron field operator is now represented in terms of the spinor [19]

$$\Psi_{\rm el}(r,\phi,z) = \frac{f_\perp(r)}{\sqrt{4\pi}} \sum_{\nu=\pm} e^{i\nu k_F z} e^{i(j-1/2)\phi} \psi_\nu(z) \begin{pmatrix} \nu \\ ie^{i\phi} \end{pmatrix} \tag{3.3}$$

with Fermi momentum $k_F = \mu/v_1$. For simplicity, the chemical potential is assumed to be below the surface state gap, i.e. $0 < \mu \ll \Delta_g$. The slowly varying chiral 1D fermion operators, $\psi_{\nu=+/-}(z)$, correspond to right- and left-movers, respectively. The radial part, $f_\perp(r)$, obeys the normalization $\int_0^\infty rdr|f_\perp(r)|^2 = 1$, vanishes for $r > R$ and decays exponentially away from the surface for $r < R$. Here the radial width, $\xi_\perp$, of the surface state depends on microscopic details [19]. For $\xi_\perp \ll R$, one has

$$f_\perp(r) \simeq \sqrt{\frac{2}{\xi_\perp R}}\, e^{-(R-r)/\xi_\perp}\, \Theta(R-r), \tag{3.4}$$

with the Heaviside step function Θ. Using the standard bosonization approach, the 1D field operators appearing in Eq. (3.3) can be expressed in terms of the dual boson field operators $\theta(z)$ and $\varphi(z)$ [32],

$$\psi_{\nu=\pm}(z) \simeq \frac{1}{\sqrt{2\pi\xi_\perp}} e^{i\sqrt{\pi}[\varphi(z)+\nu\theta(z)]}, \tag{3.5}$$

with the short-distance cutoff length $\xi_\perp$. Using Eq. (3.3), the electron density operator is then given by

$$\rho_{\rm el}(\mathbf{r}) \equiv \Psi^\dagger_{\rm el}\Psi_{\rm el} = \frac{1}{\sqrt{4\pi^3}} |f_\perp(r)|^2\, \partial_z\theta(z). \tag{3.6}$$

However, the standard $2k_F$-term, in the density operator is not present for this topological band [19]. This fact implies that charge density wave ordering is not possible. Nonetheless, once the magnetic flux deviates from half-integer values, one can see in Sec. 3.5.2 that a $2k_F$-oscillatory term appears in the density operator since backscattering is now allowed. The bosonization approach is particularly advantageous for 1D systems because it allows one to easily take into account Coulomb interaction effects [32]. Including the dominant long-range interactions within the helical Luttinger liquid picture of Ref. [19], the effective low-energy Hamiltonian for the many-electron system with half-integer flux Φ_B is given by a noninteracting boson theory,

$$H_{\rm el} = \frac{v_1}{2} \int dz \left[(\partial_z\varphi)^2 + K^{-2}(\partial_z\theta)^2 \right], \tag{3.7}$$

where the Luttinger liquid parameter K takes into account the effect of electron-electron interactions. The Luttinger Liquid parameter K follows from the bosonized Coulomb interaction Hamiltonian in 1D. Rescaling the fields then yields $v = v_1/K$ with

$$K = \frac{1}{\sqrt{1 - \frac{2e^2}{\pi\kappa v_1}(\ln[L/(2\pi R)] + 0.51)}} \tag{3.8}$$

including the electric charge, the dielectric constant within κ, the wire length L and the radius R. For more details, see Ref. [19].The noninteracting limit corresponds to $K = 1$, and repulsive interactions imply $K < 1$. For instance, $K \approx 0.5$ has been estimated for Bi_2Se_3 or Bi_2Te_3 nanowires assuming that there is no closeby metallic gate [19]. Very long wires or small radii imply that the interaction parameter vanishes and the correlations are very strong [87, 88]. Moreover, due to the identity of conjugate field, $\partial_x\varphi = -(1/v)\partial_\tau\theta$, one finds the electron action

$$S_{\text{el}} = \frac{1}{2}\int d\tau dz \left[\frac{1}{v_1}\left(\frac{\partial\theta}{\partial\tau}\right)^2 + \frac{v_1}{K^2}\left(\frac{\partial\theta}{\partial z}\right)^2\right] \tag{3.9}$$

in terms of bosonized fields.

3.2 Acoustic phonon modes

In TI nanowires made of Bi_2Se_3 or Bi_2Te_3 *ab initio* calculations have shown that low-energy phonons can be represented by two Lamé constants although the crystal structure is quite complex [127, 128]. In the following section, the acoustic phonon modes of a cylindrical wire are established by assuming that its elastic properties can be described as isotropic continuum [27, 28, 66, 129, 130]. The previous section showed that, given the half-integer magnetic flux, only one band remains gapless. Furthermore, the nanowire geometry allows for certain gapless modes. The phonon interaction will be studied in low-energy theory. However, Sec.3.2 will show that only one longitudinal mode contributes to the deformation potential.

3.2.1 Displacement fields in 3D isotropic elastic continuum

In a quantized form, lattice vibrations can be described by phonons. The vibrations lead to deformation and, thus, to displacements. The strain tensor is symmetric and diagonalizable and defines the extension or compression. It characterizes the superposition of perpendicular deformations in an infinitesimal volume. In general, small displacements $\mathbf{u}(\mathbf{r}, t)$ lead to the strain tensor

$$u_{ij}(\mathbf{r}) = (\partial_i u_j + \partial_j u_i)/2 \tag{3.10}$$

with $i, j = x, y, z$. A body experiencing deformation will provide stress, since the body is not in equilibrium anymore. The stress occurs from interaction between molecules. The components of the stress tensor describe how the forces from molecular interactions distribute over the surface. The stress tensor is a constant, if the forces compensate.

Elastic deformation implies that a body returns to its original form after deformation. This is given for small deformations while sufficiently large forces provide a remaining deformation. This thesis focuses on elastic deformations by low-energy phonons. Moreover, the studied geometries are assumed to be in isotropic continuum.

Considering a 3D isotropic elastic continuum described by the linearized strain tensor, $u_{ij}(\mathbf{r})$, and the displacement field $\mathbf{u}(\mathbf{r},t)$. The elastic free energy density then reads [66]

$$\mathcal{F}[u] = \frac{\lambda}{2}\left(\mathrm{Tr}u\right)^2 + \mu\mathrm{Tr}(u^2), \tag{3.11}$$

with the Lamé constants λ and μ, and the stress tensor takes the form

$$\sigma_{ij} = \lambda\mathrm{Tr}(u)\,\delta_{ij} + 2\mu\, u_{ij}. \tag{3.12}$$

The forces provided by the stress tensor compensate the gravitational force. Hence, one obtains the equation of motion from Eq. (3.11), which are then are given by

$$\ddot{\mathbf{u}} = c_t^2\Delta\mathbf{u} + (c_l^2 - c_t^2)\nabla(\nabla\cdot\mathbf{u}), \tag{3.13}$$

with the velocities for transverse and longitudinal sound waves, $c_t = \sqrt{\mu/\rho_M}$ and $c_l = \sqrt{(\lambda+2\mu)/\rho_M}$, respectively. Here ρ_M is the mass density. As mentioned in Sec.2.7, a crystal can be treated as an isotropic medium, if the crystallites are small enough compared to the polycrystalline structure they form [66]. For $\mathrm{Bi_2Te_3}$, experiments and simulations have shown that the isotropic elastic continuum approximation is expected to work reasonably well and one finds the mass density $\rho_M \simeq 7860$ kg/m^3 and the velocities $c_t \simeq 1600$ m/s, and $c_l \simeq 2800$ m/s [27], cf. Refs. [127,128]. For later use, the dimensionless ratio is defined by

$$\xi = c_t/c_l < 1. \tag{3.14}$$

The displacement field can always be represented as sum of longitudinal and transverse parts,

$$\mathbf{u}(\mathbf{r},t) = \mathbf{u}_l + \mathbf{u}_t = \nabla\Phi + \nabla\times\boldsymbol{\Psi}, \tag{3.15}$$

as this ansatz solves the equation of motion [66]. The longitudinal part is presented by a scalar potential $\Phi(\mathbf{r},t)$ and the transverse part by a vector potential $\boldsymbol{\Psi}(\mathbf{r},t)$, where Eq. (3.13) implies decoupled wave equations,

$$\left(\partial_t^2 - c_l^2\Delta\right)\Phi = 0, \quad \left(\partial_t^2 - c_t^2\Delta\right)\boldsymbol{\Psi} = 0. \tag{3.16}$$

However, boundary conditions will generally couple both potentials. In the next step, Eq. (3.16) is written in cylindrical coordinates. Assuming periodic boundary conditions with length L and eventually letting $L\to\infty$, translation invariance along $\hat{e}_z$ implies the (z,t)-dependence $\Phi, \boldsymbol{\Psi} \sim e^{i(qz-\Omega t)}$, where q is a conserved wave number along $\hat{e}_z$ and $\Omega > 0$ a possible eigenfrequency. For convenience, one defines the two wave numbers

$$k_l = \sqrt{\frac{\Omega^2}{c_l^2} - q^2}, \quad k_t = \sqrt{\frac{\Omega^2}{c_t^2} - q^2}. \tag{3.17}$$

Second, to exploit rotation symmetry around $\hat{e}_z$, one expands Φ and $\boldsymbol{\Psi}$ in terms of eigenstates of the conserved total angular momentum operator J_z^{ph}. This operator has integer eigenvalues denoted by m. For the *longitudinal part*, $\mathbf{u}_l = \nabla\Phi$, J_z^{ph} is observed to act like $-i\partial_\phi$ on the scalar field Φ. Solutions to Eq. (3.16) are of the form

$$\Phi(\mathbf{r},t) = f(r)\frac{e^{im\phi}}{\sqrt{2\pi}}\frac{e^{iqz}}{\sqrt{L}}e^{-i\Omega t}, \tag{3.18}$$

with a radial Bessel equation for $f(r)$,

$$\left(\frac{1}{r}\partial_r(r\partial_r) - \frac{m^2}{r^2} + k_l^2\right) f(r) = 0. \tag{3.19}$$

The general solution of Eq. (3.19) is given by

$$f(r) = A_1 J_m(k_l r) + A_2 Y_m(k_l r), \tag{3.20}$$

with k_l in Eq. (3.17), arbitrary constants $A_{1,2}$, and the Bessel functions of the first second and kind $J_m(z)$ and $Y_m(z)$ respectively [131]. Regularity at the origin imposes $A_2 = 0$ unless one considers a hollow cylinder. The gradient of the scalar field Φ yields the longitudinal part of the displacement field, which implies that the waves are effected by compression and extension. Hence, one obtains, for given (m, q), the longitudinal part of the displacement field as

$$\mathbf{u}_l(\mathbf{r}, t) = a\left[k_l J_m'(k_l r)\hat{e}_r + \frac{im}{r} J_m(k_l r)\hat{e}_\phi + iqJ_m(k_l r)\hat{e}_z\right] \frac{e^{im\phi}}{\sqrt{2\pi}} \frac{e^{iqz}}{\sqrt{L}} e^{-i\Omega t}, \tag{3.21}$$

with an arbitrary coefficient a and $J_m'(z) = dJ_m(z)/dz$. The above expressions hold for a real wave number k_l, but analytic continuation, $k_l \to i\kappa_l$ with $\kappa_l = \sqrt{q^2 - \Omega^2/c_l^2}$, produces the corresponding results for $\Omega < c_l|q|$. For $R \to \infty$, this step does not yield physical solutions since $J_m(k_l r) \to e^{im\pi/2} I_m(\kappa_l r)$, diverges for $r \to \infty$, where $I_m(\kappa_l r)$ is the modified Bessel function of the first kind. The other modified Bessel function, K_m, diverges at the origin and is also not acceptable. However, such solutions are admitted for finite radii. With the replacement $k_l \to k_t$, see Eq. (3.17), the same remarks apply for $\mathbf{u}_t$ in Eq. (3.26) below.

Next the *transverse part*, $\mathbf{u}_t = \nabla \times \mathbf{\Psi}$ is addressed, where J_z^{ph} acts like[1]

$$J_z^{\text{ph}} = -i\partial_\phi + \Sigma_z, \quad \Sigma_z = \begin{pmatrix} 0 & -i & 0 \\ i & 0 & 0 \\ 0 & 0 & 1 \end{pmatrix} \tag{3.22}$$

on the vector field $\mathbf{\Psi}$.The Σ_z-eigenstates, $\Sigma_z|s\rangle = s|s\rangle$, for the respective eigenvalues $(s = -1, 0, 1)$ are given by

$$|1\rangle = \begin{pmatrix} 1 \\ i \\ 0 \end{pmatrix}, \quad |0\rangle = \begin{pmatrix} 0 \\ 0 \\ 1 \end{pmatrix}, \quad |-1\rangle = \begin{pmatrix} 1 \\ -i \\ 0 \end{pmatrix}. \tag{3.23}$$

In cylindrical coordinates, solutions to Eq. (3.16) then have the form

$$\mathbf{\Psi}(\mathbf{r}, t) = \Big([f_{-1}(r) + f_1(r)]\hat{e}_r + i[f_{-1}(r) - f_1(r)]\hat{e}_\phi + f_0(r)\hat{e}_z\Big) \frac{e^{im\phi}}{\sqrt{2\pi}} \frac{e^{iqz}}{\sqrt{L}} e^{-i\Omega t}, \tag{3.24}$$

where $f_s(r)$ is the radial function for the respective Σ_z-eigenstate. Using k_t in Eq. (3.17), the wave equation (3.16) then yields Bessel equations that are solved by

$$f_{s=-1,0,1}(r) = B_s J_{m+s}(k_t r), \tag{3.25}$$

---

[1] the spin-1 operator Σ_z is here expressed in Cartesian coordinates

with arbitrary constants B_s. As a result, one obtains the transverse part of the displacement field as

$$\begin{aligned}\mathbf{u}_t(\mathbf{r},t) &= \Bigg[q\left(b_1\frac{m}{k_t r}J_m(k_t r)+b_2 J_m'(k_t r)\right)\hat{e}_r \\ &+ iq\left(b_1 J_m'(k_t r)+b_2\frac{m}{k_t r}J_m(k_t r)\right)\hat{e}_\phi \\ &- ik_t b_2 J_m(k_t r)\hat{e}_z\Bigg]\frac{e^{im\phi}}{\sqrt{2\pi}}\frac{e^{iqz}}{\sqrt{L}}e^{-i\Omega t}. \end{aligned} \tag{3.26}$$

Due to the constraint $\nabla\cdot\mathbf{u}_t = 0$, here only two linear combinations of the three B_s parameters appear, namely $b_1 = B_{-1} - B_1 + ik_t B_0/q$ and $b_2 = B_{-1} + B_1$.
For a given set Λ of conserved phonon quantum numbers (see below), the normal modes of the displacement field, $\mathbf{u}_\Lambda(\mathbf{r},t) = \mathbf{u}_l + \mathbf{u}_t$, then follow from Eqs. (3.21) and (3.26). This result still depends on three arbitrary constants (a, b_1, b_2) which must be determined by geometry-specific boundary conditions and by overall normalization.

3.2.2 Modes in a cylindrical nanowire

To calculate the acoustic phonon eigenmodes of an infinitely long cylindrical wire with radius R, one imposes stress-free boundary conditions at the surface $r = R$. After expressing the stress tensor (3.12) in cylindrical coordinates [66], one finds that

$$\mathbf{u}_\Lambda(\mathbf{r},t) = u_r\hat{e}_r + u_\phi\hat{e}_\phi + u_z\hat{e}_z \tag{3.27}$$

has to obey the following conditions

$$\begin{aligned} &iqu_r + \partial_r u_z = 0, \quad \partial_r u_\phi - \frac{u_\phi}{r} + \frac{im}{r}u_r = 0, \\ &(1-2\xi^2)\left(\partial_r u_r + \frac{u_r}{r} + \frac{im}{r}u_\phi + iqu_z\right) + 2\xi^2\partial_r u_r = 0, \end{aligned} \tag{3.28}$$

with ξ given in Eq. (3.14). The phonon dispersion is then given by the solutions of the boundary condition. The following section starts with the case $m = 0$.

Modes with angular momentum $m = 0$

One can consider *torsional modes* [129], where $u_r = u_z = 0$ and only $u_\phi \neq 0$. This implies that the displacement only takes place in direction of ϕ. Moreover, this corresponds to the case $a = b_2 = 0$ in the general solution, where $u_\phi \sim J_1(k_t r)$. For angular momentum $m = 0$, the boundary conditions (3.28) simplify to $\partial_r u_\phi - u_\phi/r = 0$. Inserting the solution, one arrives at a radial quantization condition, $J_2(k_t R) = 0$, such that only certain eigenfrequencies $\Omega = \Omega_{\mathrm{T},i}(q)$ (with $i = 0, 1, \ldots$) implying zeroes of the Bessel function are allowed. Hence, one obtains the frequency

$$\Omega_{\mathrm{T},i}(q) = c_t\sqrt{q^2 + z_{2,i}^2/R^2}, \tag{3.29}$$

where $z_{k,i}$ denotes the non-negative zeroes of the Bessel function $J_k(z)$. The only gapless torsional mode comes from $i = 0$ since $z_{2,0} = 0$, where one finds

$$\Omega_{\mathrm{T}}(q) = c_t|q|, \quad \mathbf{u}_q^{\mathrm{T}}(\mathbf{r}) = \frac{2r}{R^2}\frac{e^{iqz}}{\sqrt{2\pi L}}\hat{e}_\phi. \tag{3.30}$$

For all $i > 0$, the dispersion relation acquires the finite gap $z_{2,i}c_t/R$. Using $z_{2,1} \simeq 5.1356$, the smallest of the gaps can be estimated as ≈ 34 meV for Bi_2Te_3 wires of radius $R \approx 100$ nm. Staying on energy scales well below this gap, all gapped torsional phonon modes can be neglected. This step is assumed in the low-energy theory from now on where only the $i = 0$ torsional mode in Eq. (3.30) will be retained. However, torsional modes cannot exist for $\Omega < c_t|q|$, since the modified Bessel function $I_2(\kappa_t R)$ obtained after analytic continuation has no zeroes except at the origin. All other phonon eigenmodes for $m = 0$ follow by setting $u_\phi = 0$, corresponding to $b_1 = 0$ in the general expression for $\mathbf{u}_\Lambda$. The boundary conditions (3.28) then yield

$$\boldsymbol{M}\begin{pmatrix} a \\ b_2 \end{pmatrix} = 0 \tag{3.31}$$

with the matrix $\boldsymbol{M}$ given by

$$\begin{pmatrix} qk_lJ_1(k_lR) & -(k_t^2-q^2)J_1(k_tR) \\ (k_t^2-q^2)J_0(k_lR) - \frac{2k_lJ_1(k_lR)}{R} & 4qk_tJ_1'(k_tR) \end{pmatrix}. \tag{3.32}$$

A non-trivial solution exists only for $\det\boldsymbol{M} = 0$, which yields the radial quantization condition in the form of Pochhammer's frequency equation [132–134],

$$4q^2k_lk_tJ_1(k_lR)J_0(k_tR) + (k_t^2-q^2)^2J_1(k_tR)J_0(k_lR) = \frac{2k_l\Omega^2}{Rc_t^2}J_1(k_lR)J_1(k_tR). \tag{3.33}$$

Note that $J_0'(k_tR) = -J_1(k_tR)$ and $J_1'(k_tR) = J_0(k_tR) - (1/k_tR)J_1(k_tR)$ follow from the Bessel function identities (s.App.B.1). As the following paragraph shows, Eq. (3.33) describes both longitudinal modes [129] for $\Omega > c_t|q|$, and Rayleigh surface modes for $\Omega < c_t|q|$. The *longitudinal phonon modes* are addressed first. Longitudinal modes in wires act as stress or stain along the wire [66]. For vanishing momentum q, Eq. (3.33) simplifies to

$$J_1(\varpi)\left[\varpi J_0(\xi\varpi) - 2\xi J_1(\xi\varpi)\right] = 0, \quad \varpi \equiv R\Omega/c_t. \tag{3.34}$$

where the ratio ξ is defined in Eq. (3.14). Noting that $\varpi = \Omega = 0$ solves Eq. (3.34), one observes that a gapless longitudinal phonon mode will always exist, since $J_1(\varpi = 0) = 0$. In addition, Eq. (3.34) admits gapped longitudinal modes as for the torsional case, which again are not taken into account in the low-energy theory. Second, for long wavelengths, $|q|R \ll 1$, by expanding the Bessel functions in Eq. (3.33), one finds the dispersion relation for the gapless longitudinal mode [129],

$$\Omega_{\mathrm{L}}(q) = c_{\mathrm{L}}|q|\left[1 - (\sigma qR/2)^2\right] + \mathcal{O}\left(|qR|^5\right). \tag{3.35}$$

The sound velocity for this mode is given by $c_{\mathrm{L}} = \sqrt{E/\rho_M}$ with the Young modulus $E = 2(1+\sigma)\mu$. For Bi_2Te_3, the value for E in Refs. [127, 128] results in $c_{\mathrm{L}} \simeq 2500$ m/s. In Eq. (3.35), Poisson's ratio $\sigma = \lambda/[2(\lambda+\mu)]$ in terms of the LAMÉ coefficients is used. Since usually the latter quantity is within the window $0 < \sigma < 1/2$, one finds that the

sound velocity resides within $c_t < c_\mathrm{L} < c_l$. As a consequence, the longitudinal mode (3.35) has imaginary wave number $k_l = i\kappa_l$ but real wave number k_t.
At short wavelengths, $|q|R \gg 1$, the longitudinal mode evolves into a *Rayleigh mode* with $\Omega < c_t|q|$. From Eq. (3.33), after analytic continuation $k_{l,t} \to i\kappa_{l,t}$, no physical solutions are found for $|q|R \ll 1$, i.e., there are no cylindrical Rayleigh waves in the long wavelength limit. However, for $|q|R \gg 1$, asymptotic expansion of Eq. (3.33) shows that Rayleigh modes do exist at short wavelength, with dispersion relation

$$\Omega_\mathrm{R}(q) = c_\mathrm{R}|q| + \frac{\eta_0 c_\mathrm{R}}{R} + \mathcal{O}\left(\frac{1}{|q|R}\right), \tag{3.36}$$

where $c_\mathrm{R} = \zeta c_t$ is the Rayleigh mode velocity for a planar surface [27,135] which follows by letting $R \to \infty$. The dimensionless number $\zeta < 1$ is a lengthy function of $\xi = c_t/c_l$, that follows from the boundary condition leading to $\zeta \simeq 0.92$ for $\mathrm{Bi_2Te_3}$ [27]. In Eq. (3.36), the number

$$\eta_0 = \frac{\gamma_t(1-\gamma_l\gamma_t)}{2\zeta^2[2\sqrt{\gamma_l\gamma_t} - \xi^2\gamma_t/\gamma_l - \gamma_l/\gamma_t]}, \tag{3.37}$$

with $\gamma_t = \sqrt{1-\zeta^2}$ and $\gamma_l = \sqrt{1-\zeta^2\xi^2}$ is used as well. The longitudinal mode with $\Omega_\mathrm{L}(q) \simeq c_\mathrm{L}|q|$ thus gradually evolves into the Rayleigh mode with $\Omega_\mathrm{R}(q) \simeq c_R|q|$ as $|q|R$ increases. Focusing on the low-energy regime, only the longitudinal mode will be kept in what follows. To leading order in $|q|R \ll 1$, the dispersion relation and the normalized eigenmode yield

$$\Omega_\mathrm{L}(q) = c_\mathrm{L}|q|, \quad \mathbf{u}_q^\mathrm{L}(\mathbf{r}) = \frac{\sqrt{2}\,\mathrm{sgn}(q)}{R}\frac{e^{iqz}}{\sqrt{2\pi L}}\left(\sigma q r\hat{e}_r + i\hat{e}_z\right). \tag{3.38}$$

Modes with finite angular momentum

The case of finite phonon angular momentum, $m \neq 0$ will be discussed briefly in this paragraph. The boundary conditions (3.28) then yield the condition $\boldsymbol{M}_m(a, b_2, b_1)^T = 0$, where the $m = 0$ matrix $\boldsymbol{M}$ in Eq. (3.32) is replaced by

$$\boldsymbol{M}_m = \begin{pmatrix} qk_l J_m^{l\prime} & (q^2-k_t^2)J_m^{t\prime} & \frac{mq^2}{k_tR}J_m^t \\ (q^2+\frac{2m^2}{R^2}-k_t^2)J_m^l - \frac{2k_l}{R}J_m^{l\prime} & qk_t(J_{m-2}^t + J_{m+2}^t - 2J_m^t) & qk_t(J_{m-2}^t - J_{m+2}^t) \\ \frac{1}{2}k_l^2(J_{m-2}^l - J_{m+2}^l) & qk_t(J_{m-2}^t - J_{m+2}^t) & qk_t(J_{m-2}^t + J_{m+2}^t) \end{pmatrix}. \tag{3.39}$$

where the shorthand notations $J_m^{l,t} \equiv J_m(k_{l,t}R)$ and $J_m^{l,t\prime}$ were used for the respective derivative. One easily checks that for $m = 0$, the above results are recovered from these expressions.For $|q|R \ll 1$ and angular momentum $m = \pm 1$, one obtains flexural modes with a quadratic dispersion relation [129],

$$\Omega_\mathrm{F}(q) = \frac{1}{2}c_\mathrm{L}Rq^2 + \mathcal{O}\left(|qR|^3\right). \tag{3.40}$$

These are the energetically lowest phonon modes in a cylindrical wire at long wavelengths. However, for the deformation potential coupling in Sec. 3.3, one finds that phonons with only angular momentum $m = 0$ couple to electrons since the divergence of a rotational vector field $\nabla \cdot \mathbf{u}_t(\mathbf{r}, t) = \nabla \cdot (\nabla \times \boldsymbol{\Psi})$ vanishes. For that reason, $m \neq 0$ phonon modes are not discussed in more detail here.

3.2.3 Quantization

The quantization of the phonon theory now proceeds along standard paths as described in chapter 2. The displacement field is expressed in terms of bosonic annihilation operators, b_Λ, with the commutation relation $[b_\Lambda, b^\dagger_{\Lambda'}] = \delta_{qq'}\delta_{mm'}\delta_{\lambda\lambda'}$, where Λ denotes the set of quantum numbers (q, m, λ). The index λ labels the different branches (e.g., torsional or longitudinal modes) and, in general, includes gapless as well as gapped modes. Inserting the eigenfrequencies $\Omega = \Omega_\Lambda$ into the above normal mode expressions $u_\Lambda(\mathbf{r}, t)$, the displacement field yields

$$\mathbf{u}(\mathbf{r}, t) = \sum_\Lambda \frac{1}{\sqrt{2\rho_M L \Omega_\Lambda}} \mathbf{u}_\Lambda(\mathbf{r}, t) b_\Lambda + \text{h.c.}, \tag{3.41}$$

with the non-interacting second-quantized phonon Hamiltonian

$$H_{\text{ph}} = \sum_\Lambda \Omega_\Lambda \left(b^\dagger_\Lambda b_\Lambda + 1/2 \right). \tag{3.42}$$

As shown in the following section, the only gapless phonon branch that couples to electrons via the deformation potential is given by longitudinal phonons with zero angular momentum. Their dispersion relation and the corresponding normal-mode expression are specified for $|q|R \ll 1$ in Eq. (3.40). All other phonon branches are either gapped (and can thus be included by a renormalization of the Luttinger liquid parameter), or they do not couple to electrons within the low-energy theory, like for instance longitudinal modes of nonzero angular momentum.

3.3 Electron-phonon coupling

This section focuses on the electron-phonon interaction in a cylindrical nanowire in low-energy theory. The electron-phonon coupling in rectangular nanowires has already been addressed in Ref. [136]. The electron-phonon coupling will be defined by a parameter A that can be obtained by the deformation potential. The deformation potential is derived from the electron-phonon coupling Hamiltonian based on stress free boundary conditions for the phonons.

3.3.1 Deformation potential

This section discusses the electron-phonon coupling Hamiltonian and the resulting effective action. The effective action can be solved by a functional field integral, where one integrates over phonon amplitudes. This result is important when solving the single particle Green's function in Sec.3.3.2 which depends on the functional field $\theta(z)$.

The deformation potential in low-energy theory only allows for the zero angular momentum longitudinal acoustic phonon mode. Assuming that the dominant contribution arises from the deformation potential, cf. Refs. [27, 28],

$$H_{\text{e-ph}} = \alpha \int d\mathbf{r} \rho_{\text{el}}(\mathbf{r}) \text{Tr} u(\mathbf{r}), \tag{3.43}$$

where Ref. [127] estimates the bare coupling strength $\alpha \approx 35$ eV for Bi_2Te_3. However, this value could be significantly reduced by internal screening effects and it can only be used as a rough estimate. Inserting Eq. (3.6) for the electronic density operator, keeping only a single Dirac fermion subband corresponding to TI surface states with angular momentum $j = -\Phi_B$, only phonon modes with angular momentum $m = 0$ can couple to electrons, since the band gap vanishes. Later, in Sec. 3.5.2 the case of a flux deviating from half-integer will be addressed. Moreover, at low energy scales, only gapless torsional and longitudinal phonon modes with $m = 0$ exist, see Eqs. (3.30) and (3.38), respectively. Since $\mathrm{Tr}u = \nabla \cdot \mathbf{u}^{\mathrm{T}} = 0$ for the torsional phonon mode in Eq. (3.30), the only contribution of the deformation potential (3.43) to the low-energy theory arises from the $m = 0$ longitudinal phonon mode in Eq. (3.38). Assuming that only phonon momenta with $|q|R \ll 1$ are important and taking the continuum limit $L \to \infty$ in Eqs. (3.41) and (3.42), one finds

$$\nabla \cdot \mathbf{u}(\mathbf{r}, t) = -(1-2\sigma) \int \frac{dq}{2\pi} \frac{|q|}{\sqrt{2\bar{\rho}\Omega_q}} e^{iqz} \left(b_q e^{-i\Omega_q t} + b_{-q}^\dagger e^{i\Omega_q t} \right), \tag{3.44}$$

and

$$H_{\mathrm{ph}} = \int \frac{dq}{2\pi}\, \Omega_q \left(b_q^\dagger b_q + 1/2 \right), \quad \Omega_q \equiv c_{\mathrm{L}} |q|. \tag{3.45}$$

Here the linear mass density is given by $\bar{\rho} = \pi R^2 \rho_M$, and the phonon operators b_q refer to $m = 0$ longitudinal modes, with commutator $[b_q, b_{q'}^\dagger] = 2\pi\delta(q - q')$.
Using Eqs. (3.6), (3.38), and (3.41), one then finds from Eq. (3.43) the coupling Hamiltonian

$$H_{\mathrm{e-ph}} = -\frac{i\alpha(1-2\sigma)}{c_{\mathrm{L}}} \int \frac{dq}{2\pi} \sqrt{\frac{\Omega_q}{2\pi\bar{\rho}}}\, q\tilde{\theta}(q) \left(b_q + b_{-q}^\dagger \right), \tag{3.46}$$

where $\theta(z) = \int \frac{dq}{2\pi} e^{iqz} \tilde{\theta}(q)$ with $[\tilde{\theta}(q)]^\dagger = \tilde{\theta}(-q)$ is the boson field introduced in Sec. 3.1.
For half-integer flux Φ_B, the coupled electron-phonon problem can now be solved exactly even in the presence of electron-electron interactions. One can proceed in analogy to Refs. [31, 137], where non-helical Luttinger liquids coupled to acoustic phonons have been studied. The Euclidean action for the entire system, $S = S_{\mathrm{el}} + S_{\mathrm{ph}} + S_{\mathrm{e-ph}}$, follows from the low-energy Hamiltonian terms in Eqs. (3.7), (3.45) and (3.46), respectively. Instead of the b_q and $b_q^\dagger$ phonon operators, it is convenient to use the oscillator amplitude operators

$$u_q = \frac{1}{\sqrt{2\Omega_q}} \left(b_q + b_{-q}^\dagger \right), \quad p_q = -i\sqrt{\frac{\Omega_q}{2}} \left(b_q - b_{-q}^\dagger \right), \tag{3.47}$$

with the commutator $[u_q, p_{q'}] = 2\pi\delta(q + q')$. Using bosonic Matsubara frequencies, $\omega_n = 2\pi n T$ (integer n and temperature T), the dependence on imaginary time τ is resolved by the expansion

$$u_q(\tau) = T \sum_{\omega_n} e^{-i\omega_n \tau} \tilde{u}_q(\omega_n), \quad \tilde{u}_q^*(\omega_n) = \tilde{u}_{-q}(-\omega_n), \tag{3.48}$$

and likewise for $p_q(\tau)$ and $\theta_q(\tau)$. With the shorthand notation

$$\int [dq]\, (\cdots) = T \sum_{\omega_n} \int \frac{dq}{2\pi}\, (\cdots), \tag{3.49}$$

and writing $\tilde{u}_q(\omega) \to u_q(\omega)$ (and so on), one obtains the action contributions

$$\begin{aligned}
S_{\mathrm{el}} &= \frac{1}{2vK}\int [dq]\left(\omega_n^2 + v^2q^2\right)|\theta_q(\omega_n)|^2 ,\\
S_{\mathrm{ph}} &= \frac{1}{2}\int [dq]\left(\omega_n^2 + \Omega_q^2\right)|u_q(\omega_n)|^2 , \qquad (3.50)\\
S_{\mathrm{e-ph}} &= \frac{i\alpha(1-2\sigma)}{\pi\sqrt{\bar{\rho}}}\int [dq]\ \mathrm{sgn}(q) q^2 u_q(\omega_n)\theta_{-q}(-\omega_n).
\end{aligned}$$

Here $v \equiv v_1/K$ is the plasmon velocity in the helical Luttinger liquid. Moreover, v_1 is the Fermi velocity along the wire axis and K the Luttinger liquid parameter given in Eq.(3.8) including the electron-electron interaction. In practice, one has $v \gg c_{\mathrm{L}}$. Therefore, one finds an exactly solvable Gaussian functional integral for the coupled electron-phonon system.

3.3.2 Electronic Green's function

The Gaussian integral was introduced in chapter 2. As the focus lies on the electronic degrees of freedom, one can proceed by integrating over the phonon amplitudes $u_q(\omega_n)$. As a result of this Gaussian functional integration, the effective action for the bosonized θ field describing the electronic sector is given by

$$S_{\mathrm{eff}} = \frac{1}{2}\int [dq]\ D_{\theta\theta}^{-1}(\omega_n, q)\,|\theta_q(\omega_n)|^2 , \qquad (3.51)$$

with the inverse propagator

$$D_{\theta\theta}^{-1}(\omega_n, q) = \frac{1}{vK}\left(\omega_n^2 + v^2q^2 - \left(\frac{AvK}{c_{\mathrm{L}}}\right)^2 \frac{\Omega_q^4}{\omega_n^2+\Omega_q^2}\right), \qquad (3.52)$$

where the dimensionless electron-phonon coupling parameter is defined as

$$A = \frac{(1-2\sigma)\alpha}{\pi c_{\mathrm{L}}\sqrt{\bar{\rho}v_1}}. \qquad (3.53)$$

Inserting theoretical estimates for the parameters in Eq. (3.53) for $\mathrm{Bi_2Se_3}$ and/or $\mathrm{Bi_2Te_3}$ [127, 128], one finds typical values of the order $A \lesssim 1$. This approach represents a controlled approximation in the low-energy regime. In particular, one assumes that the relevant energy scales are well below v_1/R such that higher electronic subbands can be neglected. However, gapped phonon bands could be included by a renormalization of the Luttinger liquid parameter [32], and one only has to explicitly retain the gapless phonon mode considered above. With the velocities $v_\pm > 0$ defined from

$$v_\pm^2 = \frac{1}{2}\left(v^2 + c_{\mathrm{L}}^2 \pm \sqrt{(v^2 - c_{\mathrm{L}}^2)^2 + (2AvKc_{\mathrm{L}})^2}\right) \qquad (3.54)$$

and the residues

$$F_\pm = \frac{v_\pm^2 - c_{\mathrm{L}}^2}{v_\pm^2 - v_\mp^2}, \qquad (3.55)$$

the propagator follows as

$$D_{\theta\theta}(\omega_n, q) = vK\sum_{s=\pm}\frac{F_s}{\omega_n^2 + v_s^2q^2}. \qquad (3.56)$$

Moreover, Eq. (3.55) implies $F_+ + F_- = 1$ and $\sum_s F_s(v/v_s)^2 = 1/(1 - A^2K^2)$. Similarly, the propagator for the dual boson field φ in Eq. (3.5) follows as

$$D_{\varphi\varphi}(\omega_n, q) = \frac{1}{vK} \sum_{s=\pm} \frac{v_s^2 F_s}{\omega_n^2 + v_s^2 q^2}. \tag{3.57}$$

For $A = 0$, one finds $v_+ = v$ and $v_- = c_{\mathrm{L}}$, with $F_+ = 1$ and $F_- = 0$. Using the above expressions, the electronic Green's function,

$$\mathcal{G}(\mathbf{r}, \tau) = -\left\langle \mathcal{T}_\tau \Psi_{\mathrm{el}}(\mathbf{r}, \tau) \Psi_{\mathrm{el}}^\dagger(0, 0) \right\rangle, \tag{3.58}$$

with the electron operator in Eq. (3.3) and the time ordering operator $\mathcal{T}_\tau$, can be computed in an exact manner. The nontrivial (z, τ) dependence, $\mathcal{G}(z, \tau) \propto \sum_{\nu=\pm} e^{i\nu k_F z} G_\nu(z, \tau)$, follows from the 1D Green's functions,

$$G_\nu(z, \tau) = -\langle \mathcal{T}_\tau \psi_\nu(z, \tau) \psi_\nu^\dagger(0, 0) \rangle, \tag{3.59}$$

where off-diagonal contributions (with $\nu \neq \nu'$) vanish identically. Using the bosonized 1D operators in Eq. (3.5), one obtains the left- and right moving Green's functions

$$G_{\nu=\pm}(z, \tau) = \frac{\mathrm{sgn}(\tau)}{4\pi\xi_\perp} \prod_{s=\pm} \left| \frac{\xi_\perp}{z + i v_s \tau} \right|^{\left(\frac{vK}{2v_s} + \frac{v_s}{2Kv}\right) F_s} \left(\frac{z + i\nu v_s \tau}{z - i\nu v_s \tau} \right)^{F_s}. \tag{3.60}$$

Given this result, one can compute the spectral function from the imaginary part of $\mathcal{G}$, cf. Refs. [32, 138]. The latter quantity could in principle be measured by photoemission spectroscopy. However, in what follows the focus lies on simpler observables.

3.4 Zero-temperature phase diagram

In this section, the zero-temperature phase diagram of the coupled electron-phonon system with half-integer magnetic flux Φ_B is represented. The effective low-energy action (3.51) for the electronic sector, obtained after integration over the phonon degrees of freedom, allows to obtain the exact correlation functions of all possible order parameters. In this 1D system, long-range order is not possible and one can at best find an algebraic decay of correlation functions (at $T = 0$). It is then common practice to define the phases according to the smallest decay exponent [32]. For extremely strong electron-phonon couplings with $A \geq 1/K$ in Eq. (3.53), one encounters the so-called Wentzel-Bardeen singularity, where the system becomes unstable and undergoes phase separation. Furthermore, this instability occurs as the electron-phonon coupling reaches a critical value where the specific heat diverges [31, 137]. In what follows, it is assumed that $A < 1$ and the system is stable since $K < 1$. Moreover, the previously derived model is helpful to examine different candidate order parameter correlations, for instance order parameters for singlet superconductivity. As it is of large interest in experiments, correlation functions can give an insight about dominant correlation processes within an system [87, 88].
First, as pointed out in Sec. 3.1, charge density wave correlations cannot exist in this system due to the absence of $2k_F$ backscattering. Therefore, one finds a vanishing charge density wave correlation. However, spin density wave (SDW) correlations are possible. For the surface state of the TI wire, one can either have a spin density operator component

s_ϕ along the circumferential direction, or a component s_z along the wire axis. In bosonized form, they are given by [19]

$$\begin{aligned} s_\phi(z,\tau) &= \frac{1}{2\sqrt{\pi}}\partial_z\varphi(z,\tau), \\ s_z(z,\tau) &= -\frac{1}{2\pi\xi_\perp}\cos[2k_F z + 2\sqrt{\pi}\theta(z,\tau)]. \end{aligned} \tag{3.61}$$

The first relation is due to spin-momentum locking of the TI surface state: the current density operator along the z-axis has precisely the same form. The correlation functions at $T = 0$ are (the mixed correlator vanishes)

$$\begin{aligned} \langle s_z(z,\tau)s_z(0,0)\rangle &\propto \cos(2k_F z)\prod_{s=\pm}\left|\frac{\xi_\perp}{z+iv_s\tau}\right|^{2vKF_s/v_s}, \\ \langle s_\phi(z,\tau)s_\phi(0,0)\rangle &\propto \prod_{s=\pm}|z+iv_s\tau|^{-\nu_\phi/2}, \end{aligned} \tag{3.62}$$

and can be solved by computing the path integral which yields the corresponding decay exponents $\nu_z = 2vK\sum_s F_s/v_s$ and $\nu_\phi = 2$. Here the $F_\pm$ have been defined in Eq. (3.55). For material parameters where ν_ϕ represents the slowest decay, the phase can be called 'metallic' since here the current-current correlations have the same decay law as in an unperturbed Luttinger liquid. Next, the order parameter for singlet superconductivity[2] is proportional to $\mathcal{O}_{\rm sc}(z,\tau) = \psi_+(z,\tau)\psi_-(z,\tau) \propto e^{2i\sqrt{\pi}\varphi}$ [139,140]. Pairing correlations thus decay along the wire direction as

$$\langle \mathcal{O}_{\rm sc}(z,\tau)\mathcal{O}^\dagger_{\rm sc}(0,0)\rangle \propto \prod_{s=\pm}\left|\frac{\xi_\perp}{z+iv_s\tau}\right|^{2v_sF_s/(Kv)}. \tag{3.63}$$

The resulting decay exponent is given by $\nu_{\rm sc} = (2/vK)\sum_s v_s F_s$.
Using the above results for the three exponents $(\nu_z, \nu_\phi, \nu_{\rm sc})$, the phase diagram in the K-A plane is readily determined by finding the smallest exponent for given parameter choice; see Fig.3.1. For a TI nanowire pierced by a half-integer flux Φ_B, the radius R appears only implicitly via the definition of the dimensionless electron-phonon coupling parameter A in Eq. (3.53), and possibly through a weak R-dependence of the Luttinger liquid parameter K [19]. The latter parameter can encode both the effects of Coulomb interactions and those of residual optical phonon modes not taken into account in this model, cf. Ref. [32], where $K = 1$ in the absence of interactions, $K < 1$ for repulsive interactions, and $K > 1$ for effectively attractive interactions. Fig. 3.1 shows the phase diagram using parameters appropriate for the TI material HgTe, with $v_1 \simeq 5\times10^5$ m/s [20] and $c_{\rm L} \simeq 2400$ m/s [142]. The HgTe case is especially interesting since it is not only a very clean material [143,144]. It has also been established by recent nanowire experiments that the ballistic regime is reachable in practice [20]. Moreover, these experiments have shown that the conductance oscillations of Aharonov-Bohm type allow for the distinction between topological and trivial states in nanowires made of strained HgTe. The phase diagram for Bi_2Te_3 looks qualitatively very similar, as shown in the left panel of Fig.3.1. Please note that the different sound velocity $c_{\rm L} \simeq 2500$ m/s and the Fermi velocity $v_{\rm F} \simeq 4\times10^5$ m/s according to Ref. [145] provide changes in the diagram [27].

---

[2] The angular dependence of the superconducting order parameter may include a phase winding factor $\propto e^{in\phi}$ (with some integer n) due to the magnetic flux; see Ref. [139] for a related case.

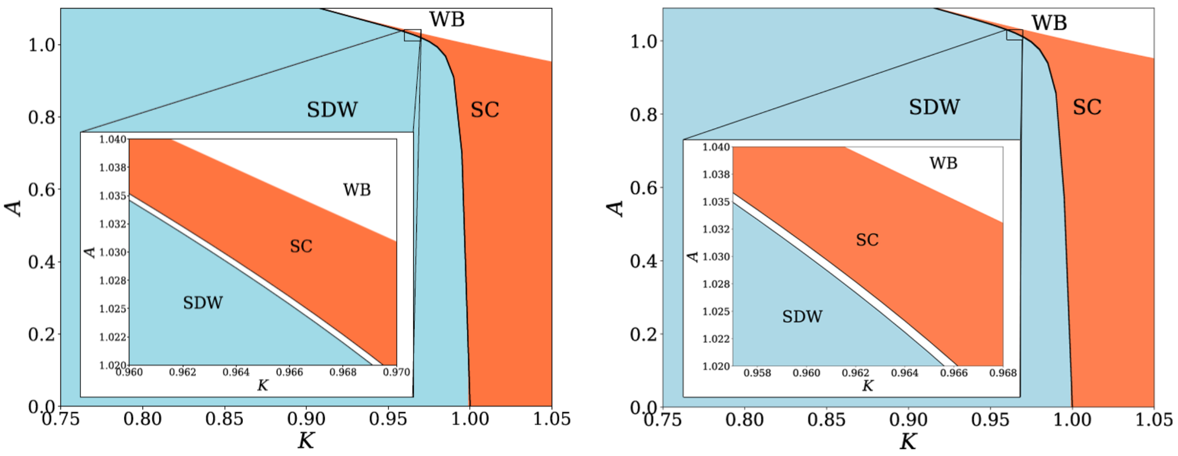

Figure 3.1: Left: Zero-temperature phase diagram of a TI nanowire (pierced by half-integer flux Φ_B) in the K-A plane, where A in Eq. (3.53) parametrizes the electron-phonon coupling strength and K is the Luttinger liquid parameter, encoding the effective electron-electron interaction strength. The material parameters for HgTe were used. For $A \geq 1/K$, the system is unstable (Wentzel-Bardeen regime, 'WB'). For $A < 1/K$, three phases are possible: Superconducting correlations dominate in the 'SC' part of the phase diagram. A spin-density wave phase (with ordering along the nanowire axis) is denoted by 'SDW'. The inset gives a magnified view of a region where the tiny intermediate 'metallic' phase (white) is visible. Here conventional 1D current-current correlations represent the slowest decay. The phase diagram has been computed with python (Matplotlib: A 2D graphics environment [141]) where the order parameter determine the limits of the phases. Adapted from Ref. [67]. Right: Zero-temperature phase diagram of a TI nanowire with material parameters for Bi_2Te_3. Please note, that the inset has a slightly different scale.

In the absence of electron-electron interactions ($K = 1$), superconducting correlations are observed that dominate for arbitrary electron-phonon coupling strength $0 < A < 1$, in accordance with earlier studies for non-helical Luttinger liquids [31,137]. Unless electron-electron interactions are screened off, however, superconducting correlations are expected to be quickly overcome by SDW correlations which are favored for $K < 1$ and small values of A. For large A (but $A < 1/K$), one also finds a tiny intermediate metallic phase, see inset of Fig. 3.1. The phase boundary curves separating the metallic phase from the SDW and the SC phases, respectively, can be analytically shown to merge at the special point ($K = 1$, $A = 0$). However, no merging point exists in the limit $K \to 0$. Ultimately, for $A \geq 1/K$, the system becomes unstable.

The theory therefore suggests the possibility of dominant intrinsic pairing fluctuations when Coulomb interactions are well screened off. The resulting superconducting wire could then even harbor Majorana bound states, see Ref. [146–148]. Such states can exist even in 1D wires with intrinsic superconducting pairing [149]. However, proximity-induced superconductivity is expected to be necessary in practice to achieve this goal since the relevant energy scales protecting the Majorana state will otherwise be tiny.

The phase diagram can significantly change when Φ_B does not have half-integer values. As discussed in detail in Sec. 3.5.2, the presence of $2k_F$ scattering then implies that also regions with CDW ordering become possible. The exploration of the phase diagram for general Φ_B is left to future work.

3.5 Phonon-induced resistivity

The next step is to evaluate the phonon-induced electrical resistivity, ρ, of a long cylindrical TI nanowire pierced by a magnetic flux Φ_B, taking into account electron-phonon couplings of dimensionless strength $A < 1/K$, see Eq. (3.53). The following section studies the case of half-integer flux Φ_B for arbitrary Luttinger liquid parameter K. From the Kubo formalism, one can show that phonons do not generate a finite resistivity correction $\rho(T)$ due to the absence of $2k_F$-backscattering processes. These processes vanish for half-integer magnetic flux which provides a closed gap of the surface state. Hence, it is a consequence of the topological protection of the states. Sec. 3.5.2 examines the case without electron-electron interactions ($K = 1$), where small flux deviations $\delta\Phi_B$ away from half-integer values are allowed. Backscattering between ($k \to -k$) then becomes possible and one obtains a finite resistivity for $T > 0$. For quantitative results, one follows the Boltzmann equation approach of Ref. [33]. Alternatively, one could proceed along the bosonization route of Ref. [150], which also allows to cover the $K \neq 1$ case for $\delta\Phi_B \neq 0$. However, in Sec. 3.5.2 the physically transparent Boltzmann approach for $K = 1$ is applied.

3.5.1 Half-integer magnetic flux: Kubo formula

First, the case of precisely half-integer flux Φ_B is discussed starting from the Kubo formula for the (ω, q)-dependent conductivity [32],

$$\sigma(\omega, q) = \frac{i}{\omega}\left(\frac{e^2vK}{\pi} + \Pi(\omega, q)\right), \tag{3.64}$$

where $\Pi(\omega, q)$ is the retarded current-current correlation function. The latter quantity is first computed in Matsubara frequency space,

$$\Pi(i\omega_n, q) = -\left\langle J^*(i\omega_n, q)J(i\omega_n, q)\right\rangle_{S_{\text{eff}}}, \tag{3.65}$$

followed by the analytic continuation $i\omega_n \to \omega + i0^+$. The charge current operator is here given by $J = \frac{evK}{\sqrt{\pi}}\partial_z\varphi$ [32]. Using Eq. (3.57), one obtains

$$\Pi(i\omega_n, q) = \frac{e^2vK}{\pi}\left(-1 + \sum_{s=\pm}\frac{\omega_n^2}{\omega_n^2 + v_s^2q^2}F_s\right). \tag{3.66}$$

Performing the analytic continuation, Eq. (3.64) yields

$$\sigma(\omega, q) = \frac{e^2vK}{2\pi}\sum_{s=\pm,\nu=\pm}F_s\left(\pi\delta(\omega - \nu v_sq) + i\mathcal{P}\frac{1}{\omega - \nu v_sq}\right), \tag{3.67}$$

where $\mathcal{P}$ denotes the principal part and the velocities $v_\pm$ have been specified in Eq. (3.54). Thus, one obtains

$$\lim_{q\to 0}\text{Re}\sigma(\omega, q) = e^2vK\delta(\omega)\sum_{s=\pm}F_s = e^2vK\delta(\omega). \tag{3.68}$$

The real part of the conductivity in dc limit yields a δ-function Drude peak at $\omega = 0$ for $q \to 0$, and hence a vanishing resistivity at all temperatures (where the above model applies). Since $vK = v_1$ by Galilean invariance, neither electron-electron nor electron-phonon interactions cause corrections to the conductivity. This result is rationalized by the absence of $2k_F$-backscattering processes in TI nanowires pierced by a precisely half-integer flux Φ_B. The next subsection addresses, what happens when Φ_B deviates from half-integer values.

3.5.2 Away from half-integer flux

This case is evaluated without electron-electron interactions, $K = 1$, while the effects of a static deviation of Φ_B from half-integer values, $\delta\Phi_B \neq 0$ are studied. Such a situation may arise either due to changes in the magnetic field strength or its direction, or from fluctuations of the cross-sectional area of the nanowire. For simplicity, $|\delta\Phi_B| \ll 1$is assumed below. For $\delta\Phi_B \neq 0$, since the electron density operator (3.6) will now have a $2k_F$-oscillatory contribution due to the absence of topological protection, phonons can cause electron backscattering. Then, a temperature-dependent correction to the electrical conductance of a TI nanowire is expected to occur. To study this effect in quantitative terms, one follows the approach in Ref. [33] and uses the Boltzmann equation to evaluate the phonon-induced conductance correction for a long TI nanowire of length L. Without coupling to phonons ($A = 0$), the ballistic system has the quantized and temperature-independent conductance $G = G_0 = e^2/h$ [19].

To determine the low-energy form of the electron density operator, the electron operator in Eq. (3.3) is generalized to the case $\delta\Phi_B \neq 0$, first. At low energies, one may focus on the single band with total angular momentum j such that $\Phi_B = -j + \delta\Phi_B$. Assuming that the chemical potential μ is located in the conductance band, Eq. (3.2) implies that the Fermi momentum is now given by

$$k_F \simeq \frac{\mu}{v_1}\left(1 - 2\gamma^2\right), \quad \gamma = \frac{v_2 \delta\Phi_B}{2\mu R}. \tag{3.69}$$

In the following, the consequences of $\gamma \neq 0$ to leading order in γ, i.e., for $|\gamma| \ll 1$, are studied. Taking the conduction band eigenstate of $\mathcal{H}_{\rm el}(k)$ in Eq. (3.7) with angular momentum j from Ref. [19], the low-energy electron operator follows as

$$\Psi_{\rm el}(r,\phi,z) = \frac{f_\perp(r)}{\sqrt{4\pi}} \sum_{\nu=\pm} e^{i\nu k_F z} e^{i(j-1/2)\phi} \psi_\nu(z) \begin{pmatrix} \nu(1-\gamma) \\ i(1+\gamma)e^{i\phi} \end{pmatrix}, \tag{3.70}$$

where all $\mathcal{O}(\gamma^2)$ terms are dropped. As for $\gamma = 0$ in Eq. (3.3), the 1D field operators $\psi_{\nu=\pm}(z)$ describe right- or left-moving fermionic quasiparticles. Indeed, linearization of the dispersion relation (3.2) around the respective Fermi point, $k = \nu k_F + p$ with $|p| \ll k_F$, yields $E_{\nu=\pm}(p) \simeq \mu \pm v_1 p$. The 1D electron density operator, $\rho_{\rm 1D}(z)$, is obtained by integration over the cross section of the nanowire and follows (to leading order in γ) as

$$\begin{aligned} \rho_{\rm 1D}(z) &= \int r dr d\phi\, \Psi^\dagger_{\rm el}(\mathbf{r})\Psi_{\rm el}(\mathbf{r}) \\ &= \sum_{\nu=\pm} \psi^\dagger_\nu \psi_\nu + 2\gamma \sum_\nu e^{-i\nu 2k_F z} \psi^\dagger_\nu \psi_{-\nu} \\ &= \frac{1}{\sqrt{\pi}} \partial_z \theta(z) + \frac{2\gamma}{\pi\xi_\perp} \cos\left[2k_F z + 2\sqrt{\pi}\theta(z)\right]. \end{aligned} \tag{3.71}$$

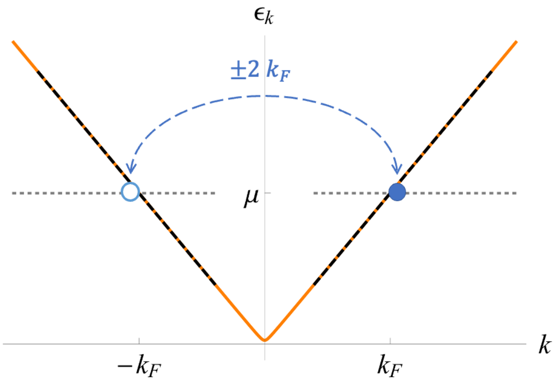

Figure 3.2: Phonon-induced backscattering of a the a surface state in a TI nanowire. The orange line defines the energy dispersion.The linearized dispersions are presented by the dashed black lines. Loosely adapted from Ref. [19, 30].

In the last step, the bosonization identity (3.5) was used. Equation (3.71) shows that for $\delta\Phi_B \neq 0$, the electron density operator contains a $2k_F$-oscillatory term corresponding to electron backscattering. The backscattering process is presented in Fig.3.2. By variation of the flux $\delta\Phi_B$, the relative importance of this term compared to the forward scattering contribution — the first term in Eq. (3.71) — can be changed. For $\gamma \neq 0$, on top of Eq. (3.46) the electron-phonon interaction Hamiltonian then receives an additional term from the deformation potential in Eq. (3.43),

$$H'_{\mathrm{e-ph}} = -v_1 Z \int dz \sum_{\nu=\pm} e^{-i\nu 2k_F z} \psi^\dagger_\nu \psi_{-\nu} \int \frac{dq}{2\pi} e^{iqz} \sqrt{|q|} \left(b_q + b^\dagger_{-q} \right), \tag{3.72}$$

which describes electron backscattering with the simultaneous absorption or emission of a phonon. The corresponding dimensionless coupling constant is given by

$$Z = \sqrt{2\pi^2 c_{\mathrm{L}}/v_1}\; A\gamma, \tag{3.73}$$

with the electron-phonon coupling parameter A in Eq. (3.53) and $\gamma \propto \delta\Phi_B$ in Eq. (3.69). The transition probability for absorption (‘$-$’) or emission (‘$+$’) of a phonon during a quasiparticle scattering process with momentum $p \to p'$ with respect to the Fermi points $\nu \to \nu'$ can be estimated from Fermi’s golden rule as

$$W^{\pm}_{\nu',\nu}(p',p) \propto \Omega_{p-p'}\; \delta\left(E_{\nu'}(p') - E_\nu(p) \pm \Omega_{p-p'+(\nu-\nu')k_F} \right) \tag{3.74}$$

where energy conservation implies $E_{\nu'}(p') - E_\nu(p) \pm \Omega_{p-p'+(\nu-\nu')k_F}$.Using the linearized dispersion relation $E_\nu(p) = \mu + \nu v_1 p$, one first observes that energy conservation requires $v_1|p-p'| = c_{\mathrm{L}}|p-p'|$ for forward scattering processes ($\nu' = \nu$). Unless one accidentally has $c_{\mathrm{L}} = v_1$, the only solution is given by $p = p'$. Transition probabilities for forward scattering processes thus vanish identically, $W^{\pm}_{\nu,\nu}(p',p) = 0$, in accordance with the results in Sec. 3.5.1. For $\gamma \neq 0$, phonon-induced backscattering transitions (with $\nu' = -\nu$) become possible because of $H'_{\mathrm{e-ph}}$ in Eq. (3.72). Fermi’s golden rule then yields the transition probabilities

$$\begin{aligned} W^{\pm}_{-\nu,\nu}(p',p) &= 2\pi v_1^2 Z^2 |2\nu k_F + p - p'| \\ &\times \delta\left(-\nu[2k_F + v_1(p+p')] \pm \Omega_{p-p'+2\nu k_F}\right). \end{aligned} \tag{3.75}$$

The next step is to compute the conductance correction, $G = G_0 + \Delta G(T)$, arising due to phonon-induced backscattering transitions. Following Ref. [33], one can consider a TI wire of length L across which a small bias voltage V is applied. The quasi-classical distribution function of fermionic quasiparticles at position z with momentum $\nu k_F + p$ (where $|p| \ll k_F$ and $\nu = \pm$ for right- or left-moving particles) is denoted by $f_\nu(z, p)$. For $A = 0$, this distribution function reduces to a z-independent Fermi-Dirac distribution,

$$f_\nu(z,p)|_{A=0} = f_\nu^{(0)}(p) \equiv \frac{1}{e^{\nu(v_1 p - eV/2)/T} + 1} \tag{3.76}$$

where the $\pm eV/2$ will be omitted later, expanding the voltage bias V to the first order [33]. Writing $f_\nu(z,p) = f_\nu^{(0)}(p) + \Delta f_\nu(z,p)$, the Boltzmann equation is given by [33]

$$\nu v_1 \partial_z \Delta f_\nu = I\left[f^{(0)}\right] + e\partial_z \phi_e \, \partial_p f_\nu^{(0)}, \tag{3.77}$$

where $\phi_e(z)$ is the electrostatic potential along the wire. With the shorthand notation $q_\nu = p - p' + 2\nu k_F$, the collision integral (omitting the superscripts '(0)' in intermediate steps) is given by

$$\begin{aligned} I\left[f_\nu(p)\right] &= -\int \frac{dp'}{2\pi} \Big\{ W^+_{-\nu,\nu}(p',p)\left[f_\nu(p)\left(1 - f_{-\nu}(p')\right)\left(1 + N_{q_\nu}\right) - f_{-\nu}(p')\left(1 - f_\nu(p)\right) N_{q_\nu}\right] \\ &+ W^-_{-\nu,\nu}(p',p)\left[f_\nu(p)\left(1 - f_{-\nu}(p')\right) N_{-q_\nu} - f_{-\nu}(p')\left(1 - f_\nu(p)\right)\left(1 + N_{-q_\nu}\right)\right]\Big\}, \end{aligned} \tag{3.78}$$

where phonons are distributed according to the Bose-Einstein distribution function, $N_q = 1/\left(e^{\Omega_q/T} - 1\right)$. Inserting the transition probabilities (3.75) into Eq. (3.78), one finds

$$I\left[f_\nu(p)\right] = -2\sinh\left(\frac{\nu eV}{2T}\right) f_\nu(p) \int \frac{dp'}{2\pi} f_{-\nu}(p') N_{q_\nu} \left[W^+_{-\nu,\nu}(p',p) e^{\nu v_1 p/T} + W^-_{-\nu,\nu}(p',p) e^{-\nu v_1 p'/T}\right]. \tag{3.79}$$

By using the identity $W^+_{\nu',\nu}(p',p) = W^-_{\nu,\nu'}(p,p')$, one observes that $\sum_{\nu=\pm} \int \frac{dp}{2\pi} I\left[f_\nu(p)\right] = 0$. Solving the Boltzmann equation (3.77) as detailed in Ref. [33], the conductance correction then follows as

$$\Delta G = \lim_{V \to 0} \frac{eL}{V} \int \frac{dp}{2\pi} I\left[f_+^{(0)}(p)\right]. \tag{3.80}$$

Next one observes that the δ-function in the transition probabilities (3.75) enforces the energy conservation condition $v_1(p' + p) = \pm c_L |2k_F + p - p'|$. Taking into account that $c_\mathrm{L} \ll v_1$ and $|p|, |p'| \ll k_F$, the solution is given by $p' \simeq -p \pm 2k_F c_\mathrm{L}/v_1$. To lowest order in V, Eq. (3.79) then gives

$$\begin{aligned} I\left[f_+(p)\right] &\simeq -2k_F v_1 Z^2 N_{2k_F} \frac{eV e^{T_\mathrm{BG}/2T}}{T} \\ &\times \sum_\pm f_+(p)\left(1 - f_+(p \mp T_\mathrm{BG}/v_1)\right) e^{\pm T_\mathrm{BG}/2T}, \end{aligned} \tag{3.81}$$

with the Bloch-Grüneisen temperature $T_\mathrm{BG} \equiv 2c_\mathrm{L} k_F$. Once T drops below T_BG, phonon-induced $2k_F$-backscattering becomes suppressed since phonon modes with the required energy of order Ω_{2k_F} are not available anymore. One then basically has only forward scattering processes, where the corresponding transition amplitudes vanish and one therefore expects an exponential suppression of the phonon-induced resistivity, see Refs. [33,150,151].

Performing the integration in Eq. (3.80), the conductance reduction is given by

$$\frac{\Delta G(T)}{e^2/h} = -2k_F L Z^2 \frac{T_{\mathrm{BG}}/(2T)}{\sinh^2\left[T_{\mathrm{BG}}/(2T)\right]}. \tag{3.82}$$

As a consequence, the *phonon-induced electrical resistivity* is

$$\rho(T) = \frac{h}{e^2}\frac{2(v_2/v_1)^2}{\pi\rho_M T_{\mathrm{BG}}}\left(\frac{(1-2\sigma)\alpha\,\delta\Phi_B}{v_1 R^2}\right)^2 \frac{T_{\mathrm{BG}}/(2T)}{\sinh^2\left[T_{\mathrm{BG}}/(2T)\right]}, \tag{3.83}$$

where the definitions of A and γ in Eq. (3.73) were used as well as $k_F \approx \mu/v_1$, see Eq. (3.69). Since only one channel contributes at the same time, the relation between the conductance correction and the resistivity is immediately given. However, this is different if more than one channel contributes to the conductivity as will be represented in chapter 4. At fixed temperature and chemical potential, the resistivity thus scales as $\rho \propto (\alpha\delta\Phi_B/R^2)^2$ with the deformation potential coupling α, the deviation $\delta\Phi_B$ of magnetic flux from the nearest half-integer value, and the nanowire radius R. In particular the prediction $\rho \propto \delta\Phi_B^2$ may allow for direct tests of this theory using available TI nanowires [20,121]. At low temperatures compared to the Bloch-Grüneisen temperature, Eq. (3.83) implies an exponential suppression of the resistivity, $\rho(T \ll T_{\mathrm{BG}}) \propto (T_{\mathrm{BG}}/T)e^{-T_{\mathrm{BG}}/T}$, as expected from Refs. [33,150,151]. On the other hand, at high temperatures, the standard linear T dependence, $\rho(T \gg T_{\mathrm{BG}}) \propto T/T_{\mathrm{BG}}$, is recovered.

3.6 Summary and Conclusions

In this chapter the electron-phonon interaction in a cylindrical TI nanowire was discussed. Based on the model in Ref. [19], the electron action was defined including electron-electron interactions within the helical Luttinger liquid parameter K. The electron action was then expressed in terms of bosonized, conjugate fields. The half-integer flux treading the nanowire along the length of the wire, prohibits $2k_F$ backscattering processes induced by phonons and provides topologically protected Dirac fermions.

The phonon modes were established in the isotropic elastic continuum model. However, in low-energy theory, the only contributing modes to electron-phonon interactions are the lowest longitudinal phonon modes with $m = 0$ angular momentum. Torsional modes do not contribute to the deformation potential and flexural modes as well as longitudinal modes of larger angular momentum are gapped for half-integer magnetic flux. Rayleigh surface modes do not exist in the long-wave length regime. The magnetic flux enters the electron-phonon interaction only for small deviation away from the half-integer flux.

While the half-integer flux protects the system from phonon-induced backscattering, a magnetic flux slightly deviating from half-integer leads to phonon-induced resistivity with a *Bloch-Grüneisen* temperature proportional to $2k_F$ as it allows for $2k_F$ backscattering.

The phase diagram at half-integer flux represents a spin density phase which dominate for electron-electron interactions and low electron-phonon coupling strength. Furthermore, superconducting pairing is possible in absence of electron-electron interactions. These phases are separated by a very small metallic phase.

The conductivity at half-integer magnetic flux is not effected by electron-electron nor electron-phonon interaction. Furthermore, away from half-integer flux the resistivity increases since $2k_F$ backscattering is allowed. This, however, implies that $\delta\Phi_B$ is very small and electron-electron interaction is absent. However, it has been shown that electron-electron interactions on TI surfaces provide temperature dependent contributions [29]. This case is left for future study.

The topological insulator nanowire has one channel contributing to the conductivity at the same time. The following chapter introduces the WSM nanowire with a significantly different band structure providing different transport properties.

Chapter 4

Transport in Weyl semimetal nanowires

Weyl semimetals (WSM) are of large interest in recent studies [15,56,152]. These materials impose surface states at the Weyl nodes and connect them in the surface Brillouin zone (sBZ) forming arcs. The arcs are known as Fermi arc surface states. ARPES measurements of these Fermi arc states have been shown in Fig.2.8 in chapter 2 [14–16, 18]. An interesting phenomenon that appears in WSMs is chiral anomaly which leads to various effects like anomalous Hall conductivity [153,154]. However, the impact of chiral anomaly on transport properties is not clarified, yet.

This chapter discusses the band structure in a WSM nanowire threaded by a magnetic flux along the wire. WSM nanowires without disorder have already shown interesting transport properties [26, 35, 155]. Moreover, the significance of the Fermi arcs is observable [24, 156, 157]. In this chapter, the interactions of electrons with acoustic phonons leading to backscattering will be compared to the disorder-free case. Also the parameterized boundary condition (s.Ref. [35, 38]) will be used in order to preserve the angular momentum at the boundary.

Transport experiments have already been done for Dirac semimetals [158–161]. Magnetoresistance has also been studied for quasi 1D-WSMs and ultra thin devices [36, 37]. As already seen in the previous chapters, temperature has a significant impact on phonon interaction [33, 150, 151]. This was also shown in WSM experiments [162–165]. While phonon-induced resistivity has been studied for different geometries of various materials, in WSMs electron-phonon interaction has been studied in slab geometry so far [166–171]. Phonon interaction in a wire can be described similarly to the TI case in the isotropic elastic continuum with a stress free boundary. However, in WSMs also bulk states are gapless. This leads to an important difference between WSMs and TIs [172]. This chapter will show, how the different bands correspond to magnetoresistivity. The model is based on the two-band model in Eq.(2.27) [71, 173, 174].

The first section addresses the electronic band structure and discusses the effects of magnetic flux and the boundary condition. The band structure is followed by the phonon coupling. The discussion about magnetoresistivity is split into two parts. In the first part the two-terminal conductance without phonon-interaction is discussed. In the second part phonon-induced backscattering will be introduced.

This chapter follows the structure of Ref. [78] by De Martino *et al.* on which it is based[1]. Ref. [78] is in principal reproduced in the following, including extended results and is partially presented in App.C.

---

[1] For the preprint s.Ref. [175]

4.1 Model and band structure

This section focuses on the electronic band structure in a WSM nanowire. The model is based on the commonly used two band-model [70, 71]. Furthermore, the model is $\mathcal{P}$-symmetric. Therefore, $\mathcal{T}$-symmetry is broken in order to have two Weyl nodes in the bulk BZ which are set at the momenta $\mathbf{k} = \pm b\hat{e}_z$. The wire length goes along the z-direction. It has cylindrical geometry with a radius R around the axis $\hat{e}_z$. The magnetic flux in units of flux quantum $\Phi_0 = hc/e$ treads the wire in z-direction as well. Moreover, the Weyl nodes are separated in the same direction. Hence the magnetic field with positive B is $\mathbf{B} = B\hat{e}_z$ and a symmetric gauge $\mathbf{A} = \frac{1}{2}B(-y, x, 0)$ will yield $B = \partial_x A_y - \partial_y A_x$. Ref. [26] showed that magnetic fields perpendicular to the wire axis provide a reduced conductance due to the occurrence of zeroth chiral Landau Levels.

The electronic Hamiltonian follows from Eq.(2.27) and Ref. [70, 71]. Isotropic circular planes require that the hopping amplitudes yield $t_x = t_y = t_\perp$. Including the magnetic field, one obtains the low-energy Hamiltonian

$$H_0 = v[\sigma_x(-i\partial_x + A_x) + \sigma_y(-i\partial_y + A_y)] + m_k\sigma_z \tag{4.1}$$

where the Pauli-matrices $\sigma_{x,y,z}$ act in spin-orbital space and the bulk Fermi velocity is denoted by v. The momentum k is the quantum number describing the momentum along the wire. Linearizing in k, the t'-term with hopping amplitude t' has vanished and the effective mass function yields

$$m_k = \frac{v}{2b}(k^2 - b^2) \tag{4.2}$$

focusing on energies $|E| \lesssim vb/2$ with a mass gap of $vb/2$ at $k = 0$. Therefore, the Weyl nodes at $k = \pm b$ are well defined.The magnetic flux is perpendicular to the wire cross-section and can be described by the dimensionless parameter

$$\Phi = \frac{\pi R^2 B}{\Phi_0} = \frac{R^2}{2l_B^2} \tag{4.3}$$

in units of flux quantum with the magnetic length $l_B = \sqrt{\hbar c/(eB)}$, where a nanowire with 25 nm radius corresponds to a magnetic field of $B \approx 2\,\mathrm{T}$. The Zeeman term in Eq.(4.2) remains absent, since it was shown to have a small contribution to the band structure compared to orbital effects [176]. The dimensionless parameter determines the finite-size scale v/R and the magnetic energy scale v/l_B, since it depends on the ratio of R and l_B. Furthermore, within this energy regime the number of bands in a thin wire can be estimated by $\sim vb/(v/R) = bR$. In the following the ratio is set $Rb = 10$ in most examples implying that $Rb \gg 1$. Fig.2.8 (right) represents the ARPES measurement of TaAs, where one can estimate $b \sim 0.5\,\mathrm{nm}^{-1}$ leading to a nanowire with radius $R \sim 20\,\mathrm{nm}$ [15].

The Hamiltonian in Eq.(4.1) leads to the eigenspinor

$$\Psi_{k,j}(\mathbf{r}) = \frac{e^{ikz}}{\sqrt{L}}\frac{e^{ij\phi}}{\sqrt{2\pi}}\begin{pmatrix} e^{-i\phi/2}Y_+(\xi) \\ ie^{i\phi/2}Y_-(\xi)\end{pmatrix} \tag{4.4}$$

in polar coordinates $(x, y) = r(\cos\phi, \sin\phi)$ where $\hat{e}_r$ and $\hat{e}_\phi$ are the unit vectors. The dimensionless parameter ξ is defined by

$$\xi = \frac{r^2}{2l_B^2} \tag{4.5}$$

where $\xi/\Phi = r^2/R^2$. The half-integer values j are eigenvalues of the conserved angular momentum operator $J_z = -i\partial_\phi + \frac{1}{2}\sigma_z$. Normalization is required for the real-valued radial eigenfunctions $Y_\pm(\xi)$. Therefore, the length L of the nanowire is included. Thus, the radial spinor $Y_{k,j}(\xi)$ yields

$$l_B^2 \int_0^\Phi d\xi (Y_+^2 + Y_-^2) = 1 \text{ , where } Y_{k,j}(\xi) = \begin{pmatrix} Y_+(\xi) \\ Y_-(\xi) \end{pmatrix} \tag{4.6}$$

with normalization with respect to the cylindrical geometry. Solving the Dirac-Weyl equation for the spinor in Eq. (4.4), one finds

$$\begin{pmatrix} -\mathcal{E}_- & \sqrt{\xi}\partial_\xi + \frac{\xi+j+\frac{1}{2}}{2\sqrt{\xi}} \\ -\sqrt{\xi}\partial_\xi + \frac{\xi+j-\frac{1}{2}}{2\sqrt{\xi}} & -\mathcal{E}_+ \end{pmatrix} Y_{k,j}(\xi) = 0 \tag{4.7}$$

where the vector potential in radial coordinates yields $-iB(x \pm iy) = -e^{\pm i\phi}Br$. The energies are given by the dimensionless quantity

$$\mathcal{E}_\pm(k, E) = \frac{E \pm m_k}{\sqrt{2}v/l_B} \ . \tag{4.8}$$

The differential equation that results from Eq.(4.7) is known as *confluent hypergeometric equation* (s.App.B.2). The solution is the confluent hypergeometric function (or *Kummer's* function) $M(a, b; \xi)$ which has a regular singularity at the origin and an irregular singularity for infinite argument [131, 177, 178]. Then, the spinor has the form

$$Y_{k,j}(\xi) = \begin{cases} \xi^{\frac{1}{2}\left(j-\frac{1}{2}\right)} e^{-\xi/2} \begin{pmatrix} \left(j+\frac{1}{2}\right) M(a_j, j+\frac{1}{2}; \xi) \\ \mathcal{E}_-\sqrt{\xi} M(a_j, j+\frac{3}{2}; \xi) \end{pmatrix} , & j > 0 \\ \xi^{-\frac{1}{2}\left(j+\frac{1}{2}\right)} e^{-\xi/2} \begin{pmatrix} \mathcal{E}_+\sqrt{\xi} M(a_j+1, -j+\frac{3}{2}; \xi) \\ \left(j-\frac{1}{2}\right) M(a_j, -j+\frac{1}{2}; \xi) \end{pmatrix} , & j < 0 \end{cases} \tag{4.9}$$

where the energy and momentum dependence is kept within the parameter $a_j = (j + 1/2)\Theta(j) - \mathcal{E}_+\mathcal{E}_-$ with Heaviside step function Θ implicitly. As mentioned in chapter 2, a good boundary condition for a Weyl fermion preserves the angular momentum [38, 179]. The parameterized boundary condition implies that for a given angle, called α here, the angular momentum will be conserved. Similar to the case in half-space geometry, one can define the boundary condition for a nanowire [35]. In a cylindrical nanowire the current should vanish at the cylinder surface, i.e. at $r = R$. Hence, the boundary condition yields

$$M(\alpha)\Psi(R) = \pm\Psi(R) \quad \text{with} \quad M(\alpha) = \sigma_\phi \cos\alpha + \sigma_z \sin\alpha \tag{4.10}$$

where the Pauli matrix $\sigma_\phi = e^{-i\frac{\phi}{2}\sigma_z}\sigma_y e^{i\frac{\phi}{2}\sigma_z}$ can be derived by unitary transformation. The radial part of the current density $j^r = \Psi_{k,j}(r)^\dagger\sigma_r\Psi_{k,j}(r)$ can be obtained by Noether's theorem (E. Noether, 1918) [40, 180]. At the boundary the current then responds to

$$j^R = \Psi_{k,j}(R)^\dagger\sigma_r\Psi_{k,j}(R) = \Psi_{k,j}(R)^\dagger\sigma_r M(\alpha)\Psi_{k,j}(R) = [M(\alpha)\Psi_{k,j}(R)]^\dagger\sigma_r\Psi_{k,j}(R) = 0 \ . \tag{4.11}$$

Moreover, $M(\alpha)$ anticommutes with σ_r where $\sigma_r = e^{-i\frac{\phi}{2}\sigma_z}\sigma_x e^{i\frac{\phi}{2}\sigma_z}$. The following derivations and examples focus on the eigenvalue +1, where α is in range $-\pi/2 < \alpha \leq \pi/2$. The direction of the pseudospin is then tangential to the boundary of the wire. However,

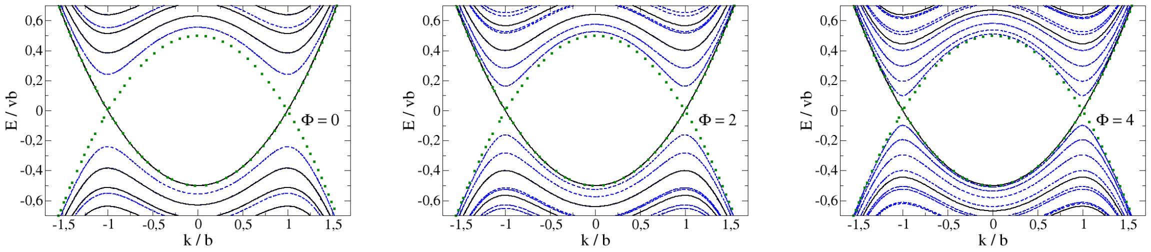

Figure 4.1: Energy bands of a WSM nanowire with boundary parameter $\alpha = \pi/2$ and $bR = 10$. The energy $E_{k,j,p}$ is in dependence of momentum k and in units of vb. The three panels show different magnetic fluxes $\Phi = 0$ (left), $\Phi = 2$ (center) and $\Phi = 4$ (right). Negative angular momenta are represented by the dashed blue curves and positive angular momenta by the solid black curves. The green dotted curves represent the $E = \pm m_k$ states which coincide with the degenerate Fermi arc surface states. The energy range represents bands with the states of angular momentum $-21/2 \leq j \leq 27/2$. Adapted from Ref. [78].

it is not in direction of the unit vector $\hat{e}_\phi$ but instead shifted by the angle α. Applying Eq.(4.10) on the spinor in Eq.(4.4), one finds

$$\frac{Y_+(\Phi)}{Y_-(\Phi)} = \tan\left(\frac{\alpha}{2} + \frac{\pi}{4}\right) \tag{4.12}$$

where $\alpha = 0$ corresponds to the infinite mass boundary condition. This condition implies a finite mass term in Eq.(4.2) inside the wire and $m_k \to \infty$ for $\xi > \Phi$ [24,35]. The energy spectrum of the WSM nanowire is defined by the solutions of the boundary condition in Eq.(4.12). For each angular momentum j and radial band index p the dispersion of a 1D subband is given by $E_{k,j,p}$. A marginal aspect is given by $\mathcal{P}$-symmetry which provides a symmetric dispersion. Hence, each subband with energy $\epsilon_k = E_{k,j,p}$ yields $\epsilon_{-k} = \epsilon_k$. Moreover, the spectrum will be characterized by the dimensionless flux Φ, the dimensionless ratio bR and the angle α.

The confluent hypergeometric function possesses a range of known analytic expansions and limits. New limits have even been derived recently [131,181]. Nonetheless the parameter regime in case of a WSM nanowire only allows for some limiting cases. Beyond these, the spectral condition is solved numerically. At the boundary angle $\alpha = \pi/2$, the spectral condition can be solved for the full spectrum. The condition then reduces to $Y_-(\Phi) = 0$. The zeros of the confluent hypergeometric function regarding the first argument $a_{j,p}$ with band index $p = 1, 2, ...$ solve the equation. Another solution is given by the band index $p = 0$ where $\mathcal{E}_- = 0$. The radial eigenfunction yields

$$Y_{k,j>0,0}(\xi) \propto \xi^{\frac{1}{2}\left(j-\frac{1}{2}\right)} e^{\xi/2} \tag{4.13}$$

which corresponds to a probability density which maximizes at the surface, where $\xi = \Phi$ and decreases if $\xi \to 0$. Furthermore, one obtains the spectrum

$$E_{k,j>0,0} = m_k \quad , \quad E_{k,j,\pm p} = \pm\sqrt{\frac{2C_{j,p}v^2}{l_B^2} + m_k^2} \tag{4.14}$$

with $C_{j>0,p} = j + 1/2 - a_{j,p}$ and $C_{j<0,p} = -a_{-(j+1),p}$. A detailed derivation of the $\alpha = \pi/2$ case is presented in App.C.1. It is worth noting that the $p = 0$ band with negative

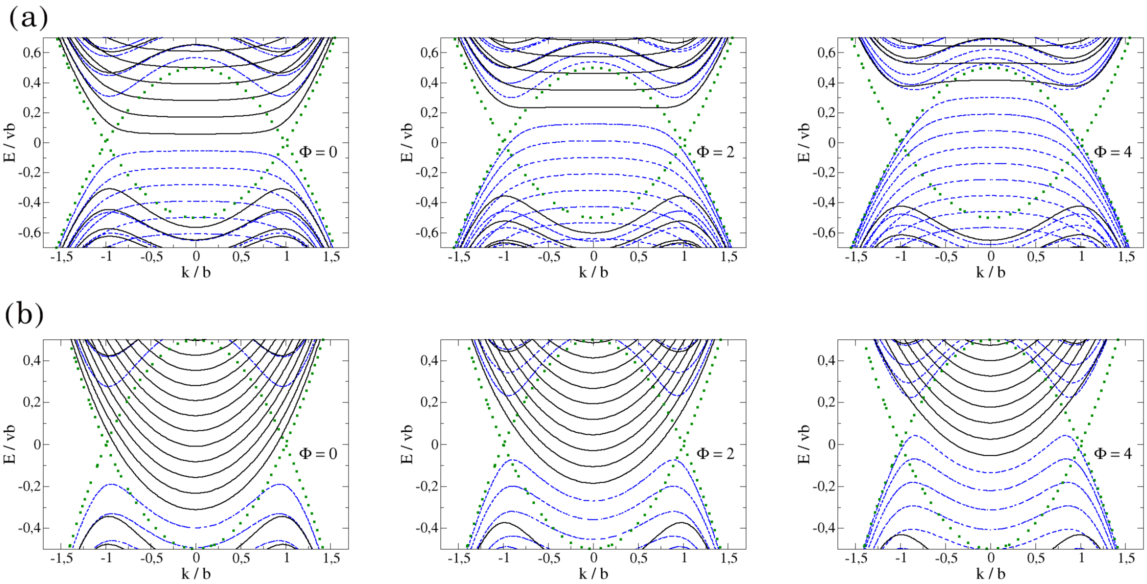

Figure 4.2: Energy bands of a WSM nanowire with boundary parameter $bR = 10$ and (a) $\alpha = 0$ and (b) $\alpha = \pi/4$. The other parameters and the representation are equal to Fig.4.2. The energy $E_{k,j,p}$ is in dependence of momentum k and in units of vb. Adapted from Ref. [78].

angular momentum implies an infinite radius and, thus, is not given within the parameter regime. The band structure for $\alpha = \pi/2$ with different values of magnetic flux is shown in Fig. 4.1. The range of angular momenta j is chosen such that the spectrum is fully given within this energy spectrum. Since $\alpha = \pi/2$, also larger j will contribute to the degenerate surface states. However, the other subbands do not appear within this energy window. At $\alpha = \pi/2$ the bands with positive angular momentum have the same degenerate dispersion relation $\epsilon_k = m_k$ of the Fermi arc which is represented by the green doted line in Fig. 4.1. The $\alpha = \pi/2$ case corresponds to the $\gamma = 0$ in Fig.2.6. However, the degeneracy is lifted as soon as α is below $\pi/2$. Fig.4.2 shows the dispersions for $\alpha = 0$ and $\alpha = \pi/4$ respectively. These dispersions were obtained numerically solving the boundary condition. One can observe that the band structure clearly depends on the magnetic flux. For positive angular momenta the states move away from $E = 0$, while for negative angular momenta, the energy surpasses $E = 0$.

An approximate analytical solution can be found for surface states. Solving the Dirac-Weyl equation (Eq.(4.7)),

$$\begin{pmatrix} -\frac{1}{v}(E - m_k) & \partial_r + \frac{j+\frac{1}{2}}{r} + \frac{r}{2l_B^2} \\ -\partial_r + \frac{j-\frac{1}{2}}{r} + \frac{r}{2l_B^2} & -\frac{1}{v}(E + m_k) \end{pmatrix} Y(r) = 0 \tag{4.15}$$

for a spinor $Y(r)$ (including k, j), one focuses on states with $r \to R$. Therefore, one can shift the radial coordinate by $r = R + x$ such that x is within the range $-R < x < 0$ and $|x| \ll R$ for a surface state. The lowest non-trivial order in $|x|/R \ll 1$ yields the equation

$$\begin{pmatrix} -\frac{1}{v}(E - m_k) & \partial_x + \frac{j+\Phi}{R} - \frac{j-\Phi}{R}x \\ -\partial_x + \frac{j+\Phi}{R} - \frac{j-\Phi}{R}x & -\frac{1}{v}(E + m_k) \end{pmatrix} \chi(x) = 0 \tag{4.16}$$

with the spinor $Y(r) = e^{(x-R)^2/4R^2}\chi(x)$. Neglecting the terms that are proportional to x an approximate solution can be found such that the spinor yields $\chi(x) \propto e^{\kappa x}\chi(0)$. This

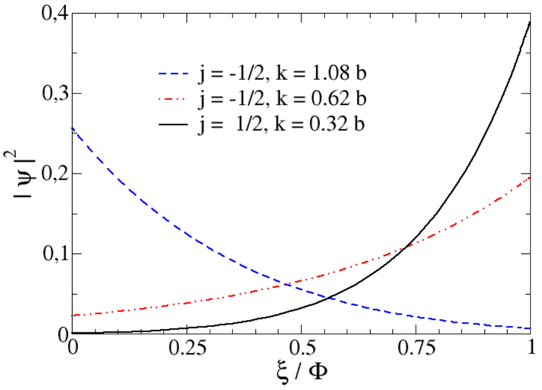

Figure 4.3: Probability density $|\Psi_{k,j}|^2$ in dependence of the radial coordinate with respect to the surface for one $j = +1/2$ eigenstate and two eigenstates of $j = -1/2$ at $E = -0.15vb$. The dimensionless parameters are given by $\alpha = \pi/4$, $bR = 10$ and $\Phi = 2$. Adapted from Ref. [78].

leads to the spinor $Y(r) \propto e^{-\kappa(R-r)}Y(R)$, where

$$\kappa = \sqrt{\frac{(j+\Phi)^2}{R^2} + \frac{m_k^2 - E^2}{v^2}} \tag{4.17}$$

is the inverse decay length. A surface state requires $\kappa R \gg 1$. Applying the boundary condition, one obtains the Fermi arc dispersion

$$E_{k,j} = \frac{v(j+\Phi)}{R}\cos(\alpha) + m_k \sin(\alpha) \quad \text{for} \quad \frac{v(j+\Phi)}{R}\sin(\alpha) - m_k\cos(\alpha) > 0 \tag{4.18}$$

which depends on the boundary angle α and the magnetic flux Φ. This stays in agreement with numerical solutions showing that the angle α and the magnetic flux affect the band structure. Similar to topological insulator nanowires, one finds that the magnetic flux acts as shift of the angular momentum. Moreover, the Fermi arc dispersion and the corresponding condition hold for

$$\left|\frac{j-\Phi}{j+\Phi}\right| \ll \kappa R \tag{4.19}$$

except when $j \to -\Phi$. The analytical and numerical solutions of the Fermi arc dispersion are compared in App.C.2. It is shown that the approximation works very well between the Weyl nodes. The flat bands for $\alpha = 0$ scale with v/R. The bands for $\alpha \neq 0$ form a Fermi arc dispersion. In both cases the approximation fits the band structure.

Focusing on bulk states located at the center of a nanowire with very large finite radius, one finds Landau states since the zeros of the confluent hypergeometric function correspond to integers with $a_{j,p} \to -(p-1)$ and $a_{j,p} < 0$ (s.App.C.1). The dispersions of the Landau states are given by

$$E_{k,j,p} = \begin{cases} \pm\sqrt{\frac{2\left(n+j+\frac{1}{2}\right)v^2}{l_B^2} + m_k^2}\ , & j > 0, p = (n, \pm) \\ \pm\sqrt{\frac{2nv^2}{l_B^2} + m_k^2}\ , & j < 0, p = (n \geq 1, \pm) \\ -m_k\ , & j < 0, p = n = 0\ . \end{cases} \tag{4.20}$$

where $n = 0, 1, 2, ...$ denotes the Landau level and the $n = 0$ state with $j < 0$ describes the chiral zero mode. The dispersions are valid for $l_B \ll R$. With the decrease of the angular momentum the state with Landau level n moves towards the surface which finally results in a chiral edge state. Moreover, one finds a Fermi arc state with $p = 0$ and positive angular momentum as long as the radius is finite. The bulk state dispersion of a state with $\Psi_{k,j<0,p=\pm1}$ becomes $E = \pm|m_k|$. This dispersion follows from the fact that the state with $p = 1$ yields $-p + 1 = 0$ and therefore does not solve $M(-p + 1, -j + 1/2; \Phi) = 0$ which results in an avoided crossing at $m_k = 0$. However, for infinite R, the dispersion $E = m_k$ vanishes and $E = -m_k$ yields the $n = 0$ Landau level dispersion which leads to a closed gap.

The radial probability density shows that surface states exist reaching the surface. However, states that have a large respond on the boundary angle α can also be identified as such. This is presented in Fig. 4.3 for $E = -0.15vb$ where the solid black line shows a state of the $j = 1/2$ subband, which at $\alpha = \pi/4$ acts as a Fermi arc dispersion. The red dashed-dotted line represents the "inner" state, i.e. the one with the smaller $|k|$, of the $j = -1/2$ subband shown in Fig.4.2. The probability of this state increases as $r \to R$, i.e. near the surface. The "outer" state defined by the dashed blue line behaves like a bulk state as it decreases reaching the surface. Nonetheless, this shows that in a WSM nanowire the bulk and surface bands are not clearly distinguishable. The band with local extrema close to the Weyl nodes for instance has one bulk and one surface state.

4.2 Phonon-induced resistivity and Boltzmann theory

This section addresses the electron-phonon interaction in a WSM nanowire leading to phonon-induced backscattering. Similar to the topological insulator nanowire, one finds that the only contributing phonon mode is the longitudinal mode with angular momentum $m = 0$. The electron-phonon Hamiltonian will be presented in Sec.4.2.1. The resistivity in Sec.4.2.3 follows from Boltzmann theory. However, there is a significant difference between the resistivity from Boltzmann theory in a WSM nanowire and the result in the previous chapter. In contrast to the topological insulator, the WSM nanowire has a spectrum where more than only one band can contribute to the resistivity. This implies that the total resistivity also depends on the resistivity of each channel. Moreover, the different shapes of the bands lead to one or more Fermi points contributing. In Sec. 4.2.3 a state with angular momentum j will be considered to contribute with either one or two Fermi momenta.

4.2.1 Electron-phonon coupling in a Weyl semimetal nanowire

Acoustic phonon modes in a nanowire can be described by the model in chapter 3 assuming isotropic elastic continuum. Expecting the nanowire to be deposited on a substrate, flexural modes will be gapped out [160, 161, 182]. Thus, the remaining gapless modes in low-energy theory, regarding the low-temperature regime with $qR \ll 1$, are the longitudinal phonon modes with angular momentum $m = 0$. These modes propagate in z-direction with a sound velocity $c_{\mathrm{L}} = \sqrt{E/\rho_M}$ where E is the Young modulus and ρ_M the mass density. Their dispersion follows from expansion of phonon momentum $q \to 0$. Furthermore, $qR \ll 1$ implies that the phonons act effectively as 1D modes. Like in $\mathrm{Bi_2Te_3}$, the sound velocity is considerably smaller than the Fermi velocity. According to Ref. [183], the ratio is $c_L/v \sim 0.01$ in TaAs.

The displacement field of a longitudinal acoustic phonon mode in an isotropic elastic nanowire is defined by

$$\mathbf{u}(\mathbf{r}) = \int \frac{dq}{2\pi} \frac{\mathrm{sgn}(q) e^{iqz}}{\sqrt{2\pi R^2 \rho_m \omega_q}} (\nu q r \hat{e}_r + i \hat{e}_z) \left(b^\dagger_{-q} + b_q \right) \tag{4.21}$$

where $b^\dagger_{-q}$ (b_q) is a bosonic creation (annihilation) operator with a phonon frequency ω_q and the bulk mass density is given by ρ_M. Poisson's ratio is defined by $0 < \nu < 1/2$. Studying the electron-phonon coupling in low-energy theory, the dominant contribution is given by the deformation potential provided by these longitudinal phonon modes. The electron-phonon Hamiltonian is then proportional to the coupling constant g_0. Hence, one finds

$$H_{el-ph} = g_0 \int d\mathbf{r} \rho_e(\mathbf{r}\ ) \nabla \cdot \mathbf{u}(\mathbf{r}) \tag{4.22}$$

where $\rho_e(\mathbf{r})$ is the charge density operator. Screening processes have a huge impact on the coupling constant. Therefore, theoretical estimations are made concerning Thomas-Fermi screening [30]. The coupling constant g_0 is given in dimension of energy and anticipated to be of order $1/n_{bulk}(\mu)$ by a Thomas-Fermi argument. Here $n_{bulk}(\mu)$ denotes the density of states in the bulk which reduces as the chemical potential μ vanishes. Hence, coupling between electrons and phonons increases as μ approaches zero and is expected to be of order $\approx 10\,\mathrm{meV}$ [184]. However, variation within the coupling is implied. Nonetheless, the resistivity will be observed with respect to a resistivity scale containing the coupling constant in the following sections.

The electron density can be expressed by fermion creation and annihilation operators $c^\dagger_{k',j,p'}$ and $c_{k,j,p}$ respectively by performing Fourier transformation. Furthermore, one finds the electron-phonon coupling Hamiltonian

$$\begin{aligned} H_{el-ph} = &- (1-2\nu) g_0 \sum_{j,p,p'} \int \frac{dk}{2\pi} \frac{dk'}{2\pi} \frac{dq}{2\pi} \delta(k-k'-q) \frac{|q| R\ l_B^2}{\sqrt{2\pi \rho_M \omega_q}} \\ &\times \int_0^\Phi d\xi\ Y^\dagger_{k',j,p'}(\xi) Y_{k,j,p}(\xi) \left(b^\dagger_{-q} + b_q \right) c^\dagger_{k',j,p'} c_{k,j,p} \end{aligned} \tag{4.23}$$

that depends on the radial part of the eigenstates $Y_{k,j,p}(\xi)$. The z and ϕ-dependencies are integrated out considering the limit of an infinite nanowire. Assuming that only longitudinal phonons with zero angular momentum couple to electrons, scattering can only take place between states with the same angular momentum. This would be different including phonon modes of larger angular momentum, where scattering between different angular momenta j becomes possible. This, however, presents an interesting future work. Considering the chemical potential in the range of $|\mu| \lesssim vb/2$, only one band with given angular momentum is present at given energy. This is important, since scattering between Fermi momenta of more than one band having the same angular momentum becomes possible. To ensure this, the band structure of each setup that is presented, was monitored.

4.2.2 Boltzmann theory

Acoustic longitudinal phonons can described very well by Boltzmann theory. This section addresses the Boltzmann approach in a WSM nanowire. Nonetheless, this result will be different than the resistivity of a TI nanowire, since the band shapes in a WSM can be parabolic, having one extremum, and also two-valley bands with two local extrema providing up to two pairs of Fermi momenta.
According to Ohm's law one finds a steady-state charge current density $J = \sigma E$ along the axis of the nanowire. The electric field is considered to be weak and translational-invariance of the wire is required. The transition rates in Boltzmann theory follow from Fermi's golden rule. Here, the coupling matrix elements are taken into account in case of electron-phonon coupling regarding that an electron scatters between two states of same angular momentum, as described in chapter 2.
The conductivity can then be obtained by the transition rates and leads to the resistivity $\rho = 1/\sigma$. Furthermore, one finds the total conductivity by summing the conductivity contributions given by each angular momentum., i.e.

$$\frac{1}{\rho} = \sum_j \sigma_j = \sum_j \frac{1}{\rho_j} \ . \tag{4.24}$$

where each resistivity ρ_j depends on the transition probabilities of the corresponding scattering processes given by Fermi's golden rule. Further processes are not included in this model. In such a case, this model will not yield the exact resistivity. As described in chapter 2, the collision integral obtained from Boltzmann equation is usually very difficult to solve. In the previous chapter, the collision integral was solved by linearizing the energy dispersion of one contributing band [33, 67]. However, this approach is not applicable to this problem, since one band can contribute with more than one pair of Fermi points to the resistivity simultaneously. It will be shown later, that for one pair of Fermi points contributing, one indeed finds the same solution. Nonetheless, a band with two contributing Fermi momenta has more scattering processes taking place between them. Thus, the resistivity will vary.
Following the ansatz of Ref. [90], one can linearize the Boltzmann equation. The ansatz estimates that the distribution functions are nearly in equilibrium. Nonequilibrium is introduced by small correction terms of linear order δn_k. Moreover, the distribution function yields

$$\delta n_k = n_F(\epsilon_k) + \delta n_k \quad \text{with} \quad n_F(\epsilon) = \frac{1}{e^{\beta(\epsilon-\mu)} + 1} \tag{4.25}$$

where the energy of the fermion is given by $\epsilon_k = \epsilon_{-k}$ with angular momentum j. Since the energy range that is observed here, always considers only one radial band for each angular momentum, one can write $E_{k,j,p} = \epsilon_k$ and $Y_{k,j,p} = Y_k$. Thus, the nonequilibrium correction can be parameterized as

$$\delta n_k = -eE \left(-\frac{\partial n_F(\epsilon_k)}{\partial \epsilon_k} \right) v_k g(\epsilon_k) \tag{4.26}$$

where the fermionic group velocity is given by $v_k = \partial_k \epsilon_k$ and $g(\epsilon_k)$ is a function that will be discussed later. Phonons with a frequency $\omega_q = c_L|q|$ enter the linearized Boltzmann equation via the collision integral. The collision kernel given by the transition probabilities and the distribution functions can be rearranged such that the linearized Boltzmann equation yields

$$v_k \frac{\partial n_F(\epsilon_k)}{\partial \epsilon_k} = \frac{1}{T} \int_{-\infty}^{\infty} \frac{dk'}{2\pi} D(k,k')[v_{k'} g(\epsilon_{k'}) - v_k g(\epsilon_k)] \sum_{\nu=\pm} \delta(\epsilon_k - \epsilon_{k'} - \nu\omega_{k-k'}) \tag{4.27}$$

where $\nu = \pm$ corresponds to phonon emission and absorption. The kernel $D(k,k')$ is then described by

$$D(k,k') = W(k,k') \frac{n_F(\epsilon_k) n_F(\epsilon_{k'})}{|e^{-\beta(\epsilon_k - \mu)} - e^{-\beta(\epsilon_{k'} - \mu)}|} \tag{4.28}$$

where $W(k,k')$ is the transition probability. Scattering takes place between two electrons. The initial state corresponds to an electron with momentum k and the final state to an electron of momentum k'. The scattering process includes either emission of a phonon with momentum $q = k - k'$ or absorption of a phonon with momentum $q = k' - k$. The scattering process between the electron involving phonon absorption has the same probability as the emission of a phonon due to microreversability. This leads to the identity $W(k,k') = W(k',k)$. The transition probability follows from Fermi's golden rule. The electron-phonon matrix elements then yield the probability

$$W(k,k') = 2\pi Z v^2 |k - k'| \mathcal{I}_{k,k'} \tag{4.29}$$

where Z denotes the dimensionless coupling parameter and $\mathcal{I}_{k,k'}$ the (squared) dimensionless overlap integral. It is interesting to note, that the overlap integral

$$\mathcal{I}_{k,k'} = \mathcal{I}_{k',k} = \left| l_B^2 \int_0^{\Phi} d\xi Y_{k'}^{\dagger}(\xi) Y_k(\xi) \right|^2 \tag{4.30}$$

becomes equal to 1 for normalized eigenfunctions with $k = \pm k'$. This is allowed, since the radial eigenfunctions depend only on k^2 within the mass term. The dimensionless electron-phonon coupling matrix parameter

$$Z = \frac{g_0^2 (1 - 2\nu)^2}{2\pi\hbar R^2 \rho_M c_L v^2} \tag{4.31}$$

is equivalent to the parameter in the TI nanowire. A TaAs nanowire with 20 nm radius and a mass density of $10\,\mathrm{g/cm^3}$ is expected to have a coupling parameter of an order of magnitude $Z \sim 10^{-8}$ which follows from a phonon velocity of $c_L \approx 2000\,\mathrm{m/s}$ that corresponds to $c_L/v \sim 0.01$.

The linearized Boltzmann equation can be solved by expressing Eq.(4.27) as the variational derivative of an auxiliary functional to find the function $g(\epsilon_k)$ where $\epsilon_k = E(k_j)$ implies the energy for given angular momentum j. The function $g(\epsilon_k) = g$ is assumed to be constant, as this is expected to be the case for scattering with low-energy phonons (s.Sec.2.7). The variational ansatz then yields the function

$$\begin{aligned} g =& \frac{C}{A} \quad \text{where} \\ C =& \int \frac{dk}{2\pi} v_k^2 \left(-\frac{\partial n_F(\epsilon_k)}{\partial \epsilon_k} \right) \\ A =& \frac{1}{2T} \int \frac{dk}{2\pi} \frac{dk'}{2\pi} D(k',k)(v_{k'} - v_k)^2 \sum_{\nu=\pm} \delta(\epsilon_k - \epsilon_{k'} - \nu\omega_{k-k'}) \end{aligned} \tag{4.32}$$

characterizing the coupling in the resistivity

$$\frac{1}{\rho_j} = e^2 \int \frac{dk}{2\pi} v_k^2 \left(-\frac{\partial n_F(\epsilon_k)}{\partial \epsilon_k} \right) g(\epsilon_k) \tag{4.33}$$

which is the only solution of the Boltzmann equation above, due to the setup. A WSM nanowire has two different shapes of bands, a two-valley band and a single-valley band. Similar to the TI surface state, the single valley band has one local extremum at $k = 0$ and a single pair of Fermi points $k = \pm k_F$. The two-valley band has up to two local extrema at $m \approx 0$ occuring from the regular (with two minima) or inverted (with two maxima) mexican hat shape. The chemical potential defines, whether zero, one or two pairs of Fermi points exist. If the two-valley band reaches the chemical potential at its minima or maxima at $k = 0$, it will also provide only one pair of Fermi points.

4.2.3 Resistivity

The phonon-induced resistivity is characterized by the scattering processes. Moreover, the number of scattering processes increases with the number of Fermi points. The number of Fermi points includes all the bands that intersect the Fermi energy and also, how often they intersect. This section discusses the resistivity regarding one or two pairs of Fermi points. Although Sec.4.3.1 will show that the conductance increases faster by a two-valley band with two Fermi point pairs than a band with one Fermi point pair, it provides more Fermi momenta with more scattering processes. Below, the resistivity of a band with one pair of Fermi momenta will be discussed, first.

One pair of Fermi points

A single pair of Fermi points can for instance occur from a parabolic band as represented in Fig.4.4. The Fermi points are denoted by $k = \pm k_F$ where $k_F > 0$. In low-energy theory, one considers acoustic phonons with low excitation energies. Hence, they are significantly smaller than the electron energies. The electron energies at the Fermi points lie near the Fermi energy $\mu = \epsilon_{k=\pm k_F}$. The group velocity at those points then yields $v_F = |\partial_k \epsilon_{k=k_F}|$. Solving the integrals in order to obtain the coupling constant g, one can linearize the energy dispersions, since the δ-function implies, that scattering takes place close to the Fermi energy according to the low-energy phonons. Thus, one finds $k \to \pm k_F$. However, close to the extremum or extrema - depending on the band shape - the linearized model becomes inappropriate. Nonetheless, solving the Boltzmann equation without linearization is quite difficult and Eq.(4.24) states, that diverging resistivity contributes only negligibly small to the total resistivity.
Proceeding as in Ref. [90], the coefficient A in Eq.(4.32) is given by

$$\begin{aligned} A =& \frac{1}{2T} \int d\epsilon d\epsilon' \int_0^\infty d\omega F(\epsilon, \epsilon', \omega) \frac{\omega n_F(\epsilon_k) n_F(\epsilon_{k'})}{|e^{-\beta(\epsilon_k - \mu)} - e^{-\beta(\epsilon_{k'} - \mu)}|} \sum_{\nu=\pm} \delta(\epsilon - \epsilon' - \nu\omega) \\ F(\epsilon, \epsilon', \omega) =& \frac{1}{\omega} \int \frac{dk}{2\pi} \frac{dk'}{2\pi} W(k', k)(v_{k'} - v_k)^2 \delta(\epsilon - \epsilon_k) \delta(\epsilon' - \epsilon_{k'}) \delta(\omega - \omega_{k-k'}) \end{aligned} \tag{4.34}$$

where $F(\epsilon, \epsilon', \omega)$ is an auxiliary function. As mentioned above, low-energy theory implies acoustic phonons with low excitation energies confining the electron energies near Fermi energy. Hence, for a single pair, one finds the momenta $k = sk_F + \tilde{k}$ and $k' = s'k_F + \tilde{k}'$

defining the initial and final states where $s, s' = \pm$ defines whether the momentum is positive or negative and $\tilde{k}$ is much smaller than the Fermi momentum. Thus, one can linearize the energy dispersion around the chemical potential lying at the Fermi energy, i.e. $\epsilon_{\pm k_F + \tilde{k}} \simeq \mu \pm v_F \tilde{k}$. Similar to the topological insulator surface state, the forwardscattering with $s' = s$ is suppressed, since the scattering electrons have nearly the same group velocity, i.e. $(v_{k'} - v_k)^2 \propto (\tilde{k} - \tilde{k}')$. However, backscattering takes place between the momenta $-k'$ and k, where $s' = -s$. Linearization of the energy implies that $v_k \simeq s v_F$. This is valid as long as the Fermi points are not close to the band bottom. Also changing α, a flat band can for instance become a two-valley band and linearization does not hold anymore. In such cases, resistivity contributions diverge. Nonetheless, the total resistivity holds, if linearization holds for other bands, since the contributions add up with $1/\rho_j$ and diverging resistivity contributions are negligible. The momentum k appears only in the mass term m_k with an order of $\mathcal{O}(k^2)$. Thus, the overlap integrals $\mathcal{I}_{k,-k}$ and $\mathcal{I}_{-k,k}$ are equal. Furthermore, the normalization of the radial part of the wave function yields also the same result as the overlap integrals. Therefore, the overlap integrals yield $\mathcal{I}_{k,-k} = \mathcal{I}_{-k,k} = 1$. Hence, the transition probability is

$$W_{bs} \approx W(k_F, -k_F) = W(-k_F, k_F) = 4\pi Z v^2 k_F \tag{4.35}$$

and moreover, the auxiliary function yields

$$F(\epsilon, \epsilon', \omega) \simeq \frac{4Zv^2}{\pi c_L} \delta(\omega - 2c_L k_F)\ . \tag{4.36}$$

According to Ref. [90], the integral in A leads to

$$\sum_{\nu=\pm} \int d\epsilon d\epsilon' \frac{n_F(\epsilon_k) n_F(\epsilon_{k'})}{\left|e^{-\beta(\epsilon_k - \mu)} - e^{-\beta(\epsilon_{k'} - \mu)}\right|} \delta(\epsilon - \epsilon' - \nu\omega) = \frac{\omega}{\cosh(\beta\omega) - 1} = \frac{\omega}{2\sinh^2(\frac{\beta\omega}{2})} \tag{4.37}$$

and one obtains the ratio A/C with

$$A \simeq \frac{4k_F}{\pi} Z v^2 \frac{\frac{T_{BG}}{2T}}{\sinh^2\left(\frac{T_{BG}}{2T}\right)} = \frac{4k_F}{\pi} Z v^2 \mathcal{F}(T_{BG}/T) \tag{4.38}$$

and $C = \simeq v_F/\pi$. The Bloch-Grüneisen temperature describes the temperature regime where acoustic phonon interaction arises. In the case of one Fermi point pair intersecting the Fermi momentum, one finds $T_{BG} = 2c_L k_F$, similar to the TI nanowire. This means that an energy $2c_L k_F$ is necessary for backscattering of an electron by a phonon. The Bloch-Grüneisen temperature is scaled around $T_{BG} \sim 10\,\mathrm{K}$ for a WSM made of TaAs. The resistivity for given angular momentum follows from Eq.(4.33)

$$\rho_j \simeq \frac{\pi\hbar}{e^2 v_F} \frac{A}{C}\ . \tag{4.39}$$

Rescaling the resistivity with $\rho_0 = (h/e^2)Zb$, one finds the resistivity for a single pair of Fermi points

$$\frac{\rho_j}{\rho_0} = \frac{2k_F}{b} \frac{v^2}{v_F^2} \mathcal{F}(T_{BG}/T) \tag{4.40}$$

which is similar to the result of the TI nanowire. However, the difference lies within the dependence on angular momentum j which determines k_F,v_F and thus the Bloch-Grüneisen temperature. Analog to the TI nanowire, the limits of the resistivity ρ_j are

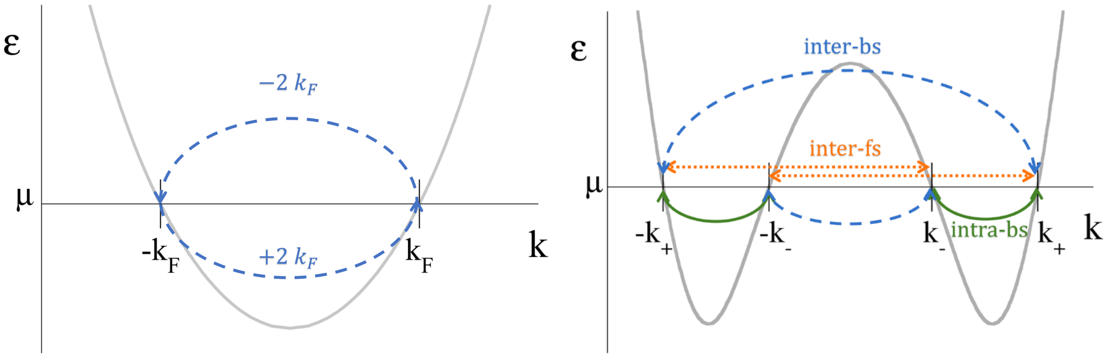

Figure 4.4: Scattering processes in a WSM nanowire. Left: Single pair of Fermi points with $2k_F$-backscattering between them. Right: Two pairs of Fermi points. The scattering processes of a two-valley band are described below.Adapted from Ref. [78].

given by an exponential suppression for very low temperatures, for instance $\rho_j \propto e^{-T_{BG}/T}$ with $T \ll T_{BG}$. At high temperatures with $T \gg T_{BG}$, one finds a linear dependence, i.e. $\rho_j \propto T$.

A single pair of Fermi points can only yield backscattering processes between these two momenta. In the following, the scattering between four momenta will be discussed. Furthermore, the Boltzmann theory will show that the approach in Ref. [33] and [67] does not hold anymore.

Two pairs of Fermi points

A two-valley band provides up to two pairs of Fermi points. Moreover, two pairs of Fermi points yield more scattering processes which can contribute to the resistivity of one channel. The model implies that the Fermi energy is set on a two-valley band such that it intersects the Fermi energy four times. The two pairs of Fermi points are set at $k = \pm k_{\gamma=\pm}$ where k_+ is the momentum on the outside, i.e. $0 < k_- < k_+$. The corresponding group velocities $v_{s,\gamma} = s\gamma v_\gamma$ yield opposite signs $s = \pm$ for the momenta k_- and k_+. The Fermi velocity is given by $v_\gamma = |\partial_k \epsilon_{k=k_\gamma}|$. Fig.4.4 represents the scattering processes of a two-valley band providing two pairs of Fermi points:

- **Inter-node backscattering:** Similar to the case, where only one pair of Fermi points exists, one has inter-node backscattering processes between momenta $k_\gamma \leftrightarrow -k_\gamma$. Here, one has two pairs, where theses processes takes place with a phonon momentum of $2k_\gamma$. In the following, $k \sim k_\gamma$ and $k' \sim -k_\gamma$ for inter-node backscattering ("inter-bs").

- **Intra-node backscattering:** The Weyl nodes appear as two local extrema of the band. Scattering between the momenta of each of these nodes, for instance $k_{-\gamma} \leftrightarrow k_\gamma$, is possible, if the chemical potential is set properly. As Fig.4.4 shows, the momentum between the Fermi momenta $k \sim sk_+$ and $k' \sim sk_-$ of each node is smaller than $2k_\gamma$. This implies, that intra-node backscattering ("intra-bs") becomes significant for low-temperatures.

- **Inter-node forwardscattering:** In the previous case forwardscattering processes were forbidden since the states were topologically protected. However, forwardscattering can now take place between a momentum $k \sim sk_\gamma$ and $k' \sim -sk_{-\gamma}$, since the momenta yield an overlap of the states. Even though the contributions can be rather small, the different velocities $v_+ \neq v_-$ are responsible that forward scattering contributions to the resistivity.

Hence, a two-valley band that intersects the chemical potential such that two pairs of Fermi momenta exist allows for the scattering processes that are described above. The Fermi momenta are located at $k = \pm k_\gamma$, where $\gamma = \pm$, has the corresponding group velocities $v_{s,\gamma} = s\gamma v_\gamma$ with $s = \pm$ due to the symmetry of the energy dispersion. The Fermi velocities v_+ and v_- are considered to be positive. The linearized dispersion provides that the auxiliary function $F(\epsilon, \epsilon', \omega)$ composes of these scattering processes, i.e. $F(\epsilon, \epsilon', \omega) \simeq F_{\text{inter-bs}} + F_{\text{intra-bs}} + F_{\text{inter-fs}}$ where $k \approx sk_\gamma$. The inter-node backscattering process yields similar results to the case, where only one pair of Fermi points exists

$$F_{\text{inter-bs}} \simeq \frac{4Zv^2}{\pi c_L} \sum_{\gamma=\pm} \delta(\omega - 2c_L k_\gamma) \tag{4.41}$$

and includes a sum over both scattering processes. Intra-node backscattering and inter-node forward scattering depend on k_+ and k_-. This implies that the overlap integral is not equal to the normalization anymore. However, the k-dependence of the eigenstate allows that $\mathcal{I}_{k_+,-k_-} = \mathcal{I}_{k_+,k_-}$. Furthermore, one obtains the auxiliary functions

$$\begin{aligned} F_{\text{intra-bs}} \simeq& \frac{2Zv^2}{\pi c_L} \frac{(v_+ + v_-)^2}{v_+ v_-} \mathcal{I}_{k_+,k_-} \delta(\omega - 2c_L|k_+ - k_-|) & (4.42) \\ F_{\text{inter-fs}} \simeq& \frac{2Zv^2}{\pi c_L} \frac{(v_+ - v_-)^2}{v_+ v_-} \mathcal{I}_{k_+,k_-} \delta(\omega - 2c_L|k_+ + k_-|) \ . & (4.43) \end{aligned}$$

The sum over all processes of the auxiliary function implies a sum over A, i.e. $A \simeq A_{\text{inter-bs}} + A_{\text{intra-bs}} + A_{\text{inter-fs}}$. Analog to the crossing of a singe pair, the inter-node backscattering has a Bloch-Grüneisen temperature of $T^{(\gamma)}_{\text{inter-bs}} = 2c_L k_\gamma$ for the scattering between each pair with k_γ. Hence, $A_{\text{inter-bs}}$ yields

$$A_{\text{inter-bs}} \simeq \frac{4}{\pi} Zv^2 \sum_{\gamma=\pm} k_\gamma \mathcal{F}\left(T^{(\gamma)}_{\text{inter-bs}}/T\right) \ . \tag{4.44}$$

The difference between a single pair of Fermi points appears already here. The ratio A/C with $C \simeq (v_+ + v_-)/\pi$ does not yield the previous result. Instead, the sum over the momenta implies that the resistivity contribution from inter-node backscattering is composed by the scattering between both momenta. The intra-node backscattering processes and the inter-node forward scattering processes provide

$$\begin{aligned} A_{\text{intra-bs}} \simeq& \frac{1}{\pi} Zv^2 \frac{(v_+ + v_-)^2}{v_+ v_-} (k_+ - k_-) \mathcal{I}_{k_+,k_-} \mathcal{F}\left(T_{\text{intra-bs}}/T\right) & (4.45) \\ A_{\text{inter-fs}} \simeq& \frac{1}{\pi} Zv^2 \frac{(v_+ - v_-)^2}{v_+ v_-} (k_+ + k_-) \mathcal{I}_{k_+,k_-} \mathcal{F}\left(T_{\text{inter-fs}}/T\right) & (4.46) \end{aligned}$$

with Bloch-Grüneisen temperatures $T_{\text{intra-bs}} = c_L(k_+ - k_-)$ and $T_{\text{inter-fs}} = c_L(k_+ + k_-)$ respectively. The resistivity of each channel is then given by a sum over all the scattering processes $\rho_j = \rho_{\text{inter-bs}} + \rho_{\text{intra-bs}} + \rho_{\text{inter-fs}}$ where each contribution is given by

$$\frac{\rho_{\text{inter-bs}}}{\rho_0} = \sum_\gamma \frac{2k_\gamma}{b} \frac{v^2}{(v_+ + v_-)^2} \mathcal{F}\left(T^{(\gamma)}_{\text{inter-bs}}/T\right) \tag{4.47}$$

$$\frac{\rho_{\text{intra-bs}}}{\rho_0} = \frac{k_+ - k_-}{b} \mathcal{I}_{k_+,k_-} \frac{v^2}{2v_+ v_-} \mathcal{F}\left(T_{\text{intra-bs}}/T\right) \tag{4.48}$$

$$\frac{\rho_{\text{inter-fs}}}{\rho_0} = \frac{k_+ + k_-}{b} \mathcal{I}_{k_+,k_-} \left(\frac{v_+ - v_-}{v_+ + v_-}\right)^2 \frac{v^2}{2v_+ v_-} \mathcal{F}\left(T_{\text{inter-fs}}/T\right) \tag{4.49}$$

where ρ_0 is the resistivity scale given above Eq.(4.40). Focusing again on the resistivity contribution by inter-node backscattering $\rho_{\text{inter-bs}}$, one observes that the final resistivity contribution also depends on the combined contributions of the backscattering processes. Therefore, Matthiessen's rule does not hold in this case due to the overall factor $1/(v_+ + v_-)^2$. Each channel provides a contribution ρ_j for a given angular momentum j affecting each scattering contribution involving the Fermi momenta $k_\pm$ and the corresponding Fermi velocities $v_\pm$. Thus, also the Bloch-Grüneisen temperatures and the overlap integrals vary in each channel. Eq.(4.24) implies that the dominant contributions to the total resistivity are given by the smallest ρ_j. Hence, the largest contribution within this channel yields the dominant term. For very small temperatures the contribution $(k_+ - k_-)$ needs the smallest phonon energy and thus dominates the resistivity contribution. In general the contribution for $T \ll T_{bBG}$ is given by $\rho_j \propto e^{-T_{bBG}/T}$ where the T_{bBG} describes one of the Bloch-Grüneisen temperatures above. At high temperature $T \gg T_{bBG}$, one recovers the linear T-dependence.

In contrast to the TI nanowire where only one pair contributes to the resistivity, the crossing of two Fermi momenta pairs in the WSM represents more scattering processes. The intra-node backscattering arises already at very low temperatures. The following section discusses the results of the two-terminal conductance at zero temperature and the phonon-induced resistivity. In both cases the effect of two crossing momenta is present and also the magnetic field is responsible for changes in transport.

4.3 Transport properties

Transport in nanowires is of large interest within this thesis, since the scattering of electrons by emission or absorption of a phonon, can affect the conductance. This section discusses the two-terminal conductance at zero temperature where phonon interaction is not present. In a WSM nanowire, this involves both type of bands, single- and two-valley bands. In the limit of zero temperature, the conductance increases with each channel that intersects the Fermi energy. Thus, the number of intersections of the Fermi energy sets the conductance. Away from zero temperature, scattering processes take place, as described in Sec.4.2.3. The model in Sec.4.2.3 is used to describe the resistivity at given temperature and for different parameterized angle α and chemical potential μ.

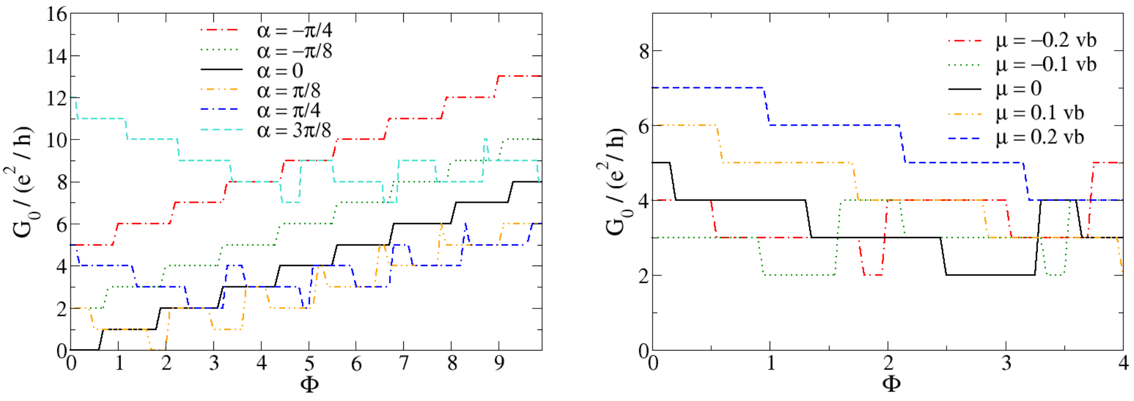

Figure 4.5: Two-terminal conductance G_0 in dependence of the magnetic flux Φ. G_0 is given in units of conductance quantum at zero temperature. The magnetic flux dependence is represented for chemical potential set at zero and $-\pi/4 \leq \alpha \leq 3\pi/8$ as well as $\alpha = \pi/4$ and $-0.2vb \leq \mu \leq 0.2vb$. Adapted from Ref. [78].

4.3.1 Zero-temperature conductance

In the limit of zero-temperature, the two-terminal conductance is not affected by phonon interaction since they remain frozen. The setup considers no disorder. Moreover, the setup responds to the Landauer-Büttiker formalism implying that the contacts connecting the nanowire to the source and drain electrodes are perfectly adiabatic [185]. As shown in Fig.4.1-4.2, number of contributing channels depends on the chemical potential μ, the magnetic flux Φ and the boundary angle α. Thus, it can be denoted as $N = N(\mu, \Phi, \alpha)$. Since the bands are symmetric in k, the number of contributing channels equals the number of positive momenta intersecting the chemical potential. Similar to Ref. [24–26] that have been discussed in Sec.2.4.3, the conductance can be obtained by

$$G_0(\mu, \Phi, \alpha) = N\frac{e^2}{h} \ . \tag{4.50}$$

The two-terminal conductance is shown in Fig.4.5 in dependence of the magnetic flux and the chemical potential. As the magnetic flux increases, the number of crossing bands varies in steps. As one band starts intersecting the Fermi energy, the conductance G_0 increases either with a step of $\Delta G_0 = +e^2/h$, if the band intersects with one pair of Fermi momenta, or a step of $\Delta G_0 = +2e^2/h$, if the band intersects with two pairs. If a band leaves the chemical potential and does not intersect the Fermi energy anymore, the conductance decreases with $\Delta G_0 = -e^2/h$ in case of one pair and $\Delta G_0 = -2e^2/h$ in case of Fermi point pairs.

Especially for $\alpha \leq 0$ in the left panel of Fig.4.5, one observes that the conductance increases in periods of magnetic flux step $\Delta\Phi \approx 1$. It was shown before in Eq.(4.18) that the Aharonov-Bohm effect provides a phase shift $j \to j + \Phi$ of the Fermi arc dispersion. A shift of the magnetic flux by $\Phi \to \Phi + 1$ then yields the following subband. As Φ increases for $\alpha \leq 0$, the band structure is dominated by surface states at $\mu = 0$. Hence, the conductance increases by one conductance quantum approximately once the magnetic flux increases by one unit. Aharonov-Bohm oscillations have also appeared in Dirac semimetal nanowires made of Cd_3As_2 where a magnetic field breaks $\mathcal{T}$-symmetry

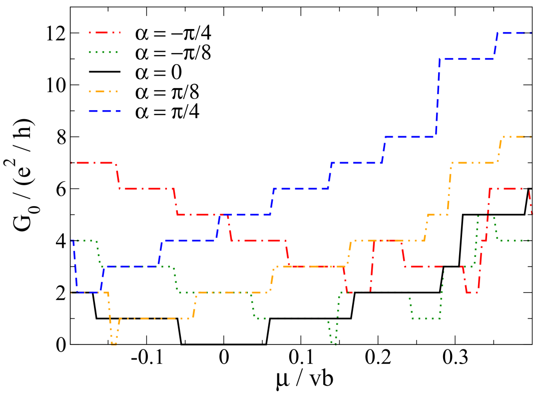

Figure 4.6: Two-terminal conductance G_0 in dependence of the chemical potential μ in units of vb. G_0 is given in units of conductance quantum at zero temperature and zero magnetic flux, i.e. $\Phi = 0$. The dependence of the chemical potential is presented for values of $-\pi/4 \leq \alpha \leq \pi/4$. Adapted from Ref. [78].

and splits the Dirac node into Weyl nodes [160, 161].
Since the boundary angle α changes the shape of the Fermi arc, it determines whether a band contributes to the conductance. The effects are represented in the left panel of Fig.4.5. For $\alpha \leq 0$, the bands with negative angular momentum obey single-valley bands with negative angular momentum and thus increasing the magnetic field, the bands intersecting the chemical potential at $\mu = 0$ contribute with one pair of Fermi points. This is represented in Fig.4.2 (a) for $\alpha = 0$. For $\alpha > 0$ the band structure composes of single-valley bands with positive angular momentum intersecting the chemical potential at zero magnetic field. One observes in Fig.4.2 (b) that increasing the magnetic field shifts these single-valley bands away from $\mu = 0$ and two-valley bands with negative angular momentum reach the chemical potential contributing with two pairs of Fermi points. Moreover, the steps are non-monotonic, since a two-valley band can also contribute with only one pair of Fermi points, if the chemical potential is away from the local minimum or maximum at $k = 0$. This leads to a drop by $\Delta G_0 = -e^2/h$. The band structure in a cylindrical WSM is very different compared to the infinite WSM case, where the lowest chiral Landau level in principle implies a negative magnetoresistance. However, the left panel of Fig.4.5 represents that for $0 \leq \alpha < \pi/2$ a minimum of magnetoconductance $\Phi \approx \xi_{\mathrm{min}}(\alpha)$ exists. This minimum follows from surface states dominating the regime for small energies and allows for the empirical relation $\alpha \simeq 0.28\xi_{\mathrm{min}} - 0.01\xi_{\mathrm{min}}$ between the boundary angle α and the magnetic flux. This connection follows from the fit of a third-order polynomial function onto the conductance. It implies that the minimum of the magnetoconductance contains information about the boundary angle α. Since α cannot be directly estimated, the connection to the minimum of the magnetoconductance can reveal some information about it.

The right panel of Fig.4.5 shows the dependence on the chemical potential for $\alpha = \pi/4$. In Fig.4.2 (b) one observes that for the given chemical potentials only single-valley bands with positive angular momentum exist at $\Phi = 0$. These bands shift away as the magnetic field increases. For a certain magnetic flux, the conductance increases by $\Delta G_0 = +2e^2/h$ as a two-valley band is reached.

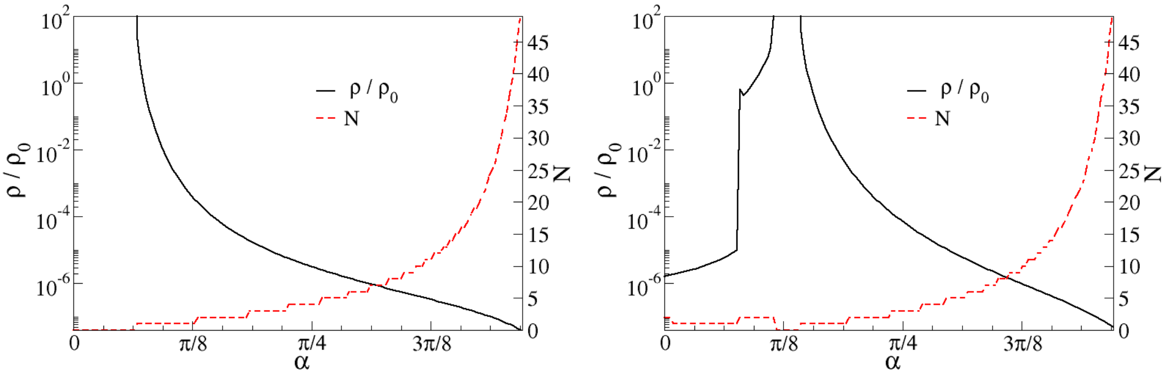

Figure 4.7: Magnetoresistivity (solid black curve) and number of Fermi point pairs (red dashed line) in dependence of boundary angle α for magnetic flux $\Phi = 1/2$ (left panel) and $\Phi = 2$ (right panel). The other parameters are estimated as follows, $T = 0.1c_L b$, $\mu = 0$, $Rb = 10$ and $c_L = 0.01v$. For $\Phi = 2$ one observes that the number of bands increases and decreases for $\alpha \lesssim \pi/8$. This case is describes in detail below. Note that the resistivity is given in logarithmic scale. Adapted from Ref. [78].

In agreement with Ref. [24], the conductance increases in steps of $\Delta G_0 = +e^2/h$ for small varying chemical potential at $\alpha = 0$ as shown in Fig.4.6. For $\mu \gtrsim 0.35vb$, the steps increase faster, as the two-valley bands are reached. The conductance is zero for $\mu = 0$ where no bands intersect the chemical potential within a gap of $\sim v/R$ and increases again for chemical potential $\mu < 0$, where the chemical potential reaches the following bands. For $\alpha \neq 0$, one finds that at $\mu = 0$ the conductance is nonzero. Nonetheless, the conductance has a minimum.

This section has shown that the magnetoconductance shows interesting features for the WSM band structure. On the one hand the band shapes contribute in different ways. On the other hand the magnetic flux shifts the bands in relation with the boundary angle which determines the band shape of Fermi arc states (s.Eq.(4.18)). So far, phonon interaction has been suppressed at zero temperature. The following section discusses the phonon-induced magnetoresistivity that arises at nonzero temperature.

4.3.2 Phonon-induced resistivity

As yet, the conductance at zero temperature has been addressed. However phonon-interaction can already arise at low temperatures and induce backscattering processes that lead to an increase of resistivity. This section addresses the magnetoresistivity that has been derived in Sec.4.2.3. The resistivity includes the interaction of a longitudinal phonon mode.

Fig.4.7 shows how the resistivity changes with α. The chemical potential is set at zero and $T = 0.1c_L b$. One observes that the resistivity decreases as the boundary angle α approaches $\pi/2$. Concurrently, the number of contributing Fermi point pairs increases and diverges for $\alpha \to \pi/2$. According to Fig.4.1, the number diverges since the bands become degenerate for $\alpha = \pi/2$. The increase of the number of Fermi points in general follows from the boundary angle changing the band shapes such that they start intersecting the chemical potential. Hence, the resistivity in the left panel diverges for $\alpha \to 0$ where

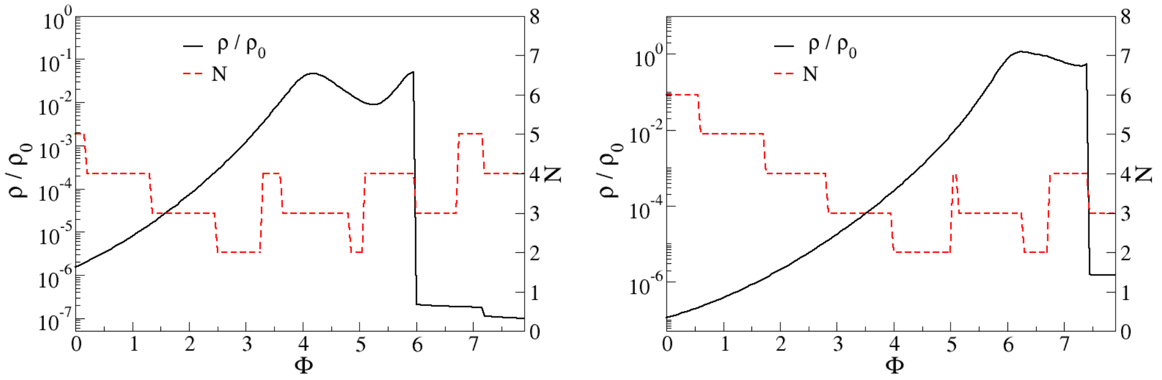

Figure 4.8: Magnetoresistivity (solid black curve) and number of Fermi point pairs (red dashed line) in dependence of the magnetic flux Φ for boundary angle $\alpha = \pi/4$ and chemical potential $\mu = 0$ (left panel) and $\mu = 0.1vb$ (right panel). The other parameters are estimated as follows, $T = 0.1c_L b$, $Rb = 10$ and $c_L = 0.01v$. Adapted from Ref. [78].

no bands intersect the chemical potential (s.Fig.4.2 (a)). As the first band enters the chemical potential, the resistivity is still very large since the Fermi velocity is close to zero. Nonetheless, since the total resistivity sums over the inverse of the contribution of each angular momentum, the total resistivity decreases as soon as the Fermi velocities are large enough. The right panel refers to a more difficult band structure for $\Phi = 2$. Around $\alpha \approx \pi/8$, the resistivity does not only diverge but it has also a steep increase. Beyond $\alpha \approx \pi/8$ the resistivity behaves similar to the resistivity for $\Phi = 1/2$, where only bands with one pair of Fermi points contribute. For $\alpha = 0$, one observes in Fig.4.2 (a) that the $j = -1/2$ and $j = -3/2$ flat bands intersect with one pair of Fermi points. Increasing the boundary angle to $\alpha \simeq \pi/16$ the band shape changes and the $j = -1/2$ becomes a two-valley band that intersects with two pairs of Fermi points. This leads to the sudden increase in resistivity since more scattering processes can occur. Furthermore, the intra-node backscattering processes have a large contribution in this temperature regime. As α approaches $\pi/8$, the $j = -1/2$ leaves the chemical potential and no band contributes until the positive angular momenta fall underneath the chemical potential.

For the two-terminal conductance and the band structure, one observes that the magnetic flux shifts the bands and thus affects the number of Fermi point pairs. The left panel of Fig.4.8 represents the resistivity for $\mu = 0$. The resistivity increases until $\Phi \approx 4$ where it drops until $\Phi \approx 5.5$ and increases again as it reaches $\Phi = 6$. The first increase appears in the regime where two-valley bands intersect the chemical potential as shown in Fig.4.2. Hence, again the intra-node backscattering has a significant impact. The drop occurs when the number of Fermi points decreases by one point pair that follows from the lowest subband with positive angular momentum leaving the chemical potential. However, being in the regime with two-valley bands, one observes the abrupt decrease at $\Phi \approx 6$ where the number of Fermi points decreases by one. Since a two-valley band can also contribute with one pair of Fermi momenta, it suddenly contributes with a lower resistivity. Moreover, Eq.(4.24) determines that the channel with the smallest resistivity dominates. Thus, the drop follows from the $j = -1/2$ subband having only one pair of Fermi points. The other panel shows $\mu = 0.1vb$. Since the chemical potential is now shifted upwards, more

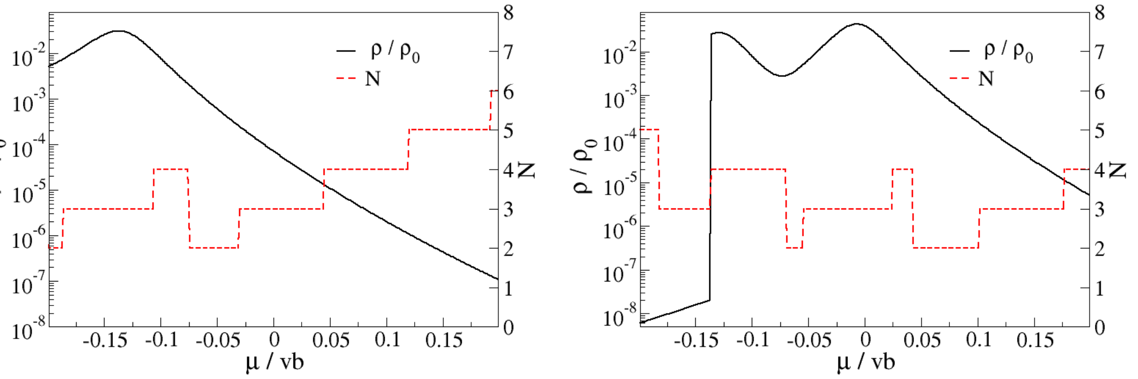

Figure 4.9: Magnetoresistivity (solid black curve) and number of Fermi point pairs (red dashed line) in dependence of the chemical potential μ in units of vb for boundary angle $\alpha = \pi/4$ and magnetic flux $\Phi = 2$ (left panel) and $\Phi = 4$ (right panel). The other parameters are estimated as follows, $T = 0.1c_Lb$, $Rb = 10$ and $c_L = 0.01v$. Adapted from Ref. [78].

bands with positive angular momentum intersect the chemical potential at $\Phi = 0$. As the magnetic flux shifts the band structure, this drop occurs at a larger Φ.

Changing the chemical potential determines how many bands contribute to the resistivity. From Fig.4.9, one follows that for $\Phi = 2$ the resistivity has a small increase and then decreases smoothly within the regime of μ. The small increase is due to two-valley bands contributing with two pairs of Fermi points. The resistivity decreases the more bands with one pair of Fermi points intersect the chemical potential. The right panel represents the resistivity at $\Phi = 4$. It behaves similar to the resistivity at $\Phi = 2$ as μ decreases until $\mu \approx 0.05vb$. Then it increases as a two-valley band enters the chemical potential with two pairs of Fermi points. At a critical value of $\mu_c \simeq -0.136vb$ the lowest subband with negative angular momentum $j = -1/2$ has its local minimum well above the chemical potential only intersecting with one pair of Fermi points. To get a better understanding about the abrupt change at the critical chemical potential, App.C.3 represents the Toy model with a simplified dispersion following Ref. [78]. Since the intra-node backscattering is absent for $\mu < \mu_c$, the large contribution by phonon backscattering to the resistivity is not given anymore. Hence, the resistivity of one subband is larger, if the Bloch-Grüneisen temperature is determined by $T_{BG} = c_L(k_+ - k_-)$ for low temperatures. As the chemical potential approaches the critical value the local minimum of the subband leaves the chemical potential. The linearization, however, does not hold for $v_- \to 0$. This leads to the sudden change in resistivity.

As already mentioned before, the temperature defines the scale of the resistivity. Fig.4.10 represents the temperature dependence for $\Phi = 0, 1$ and 4 at zero chemical potential and boundary angle $\alpha = \pi/4$. At high temperatures, for instance $T \gg 2c_Lb$, one observes the expected linear temperature dependence. According to Fig.4.8, the small temperature resistivity is larger for $\Phi = 4$ than the other values due to intra-node backscattering processes. This feature is also observable in Fig.4.10. Furthermore, the decay of resistivity is exponential as the temperature approaches zero and no phonon-interactions take place. Hence, the resistivity of a WSM nanowire depends very much on the magnetic flux Φ and the boundary angle α. For instance, the angle α changes the curvature of the Fermi arc

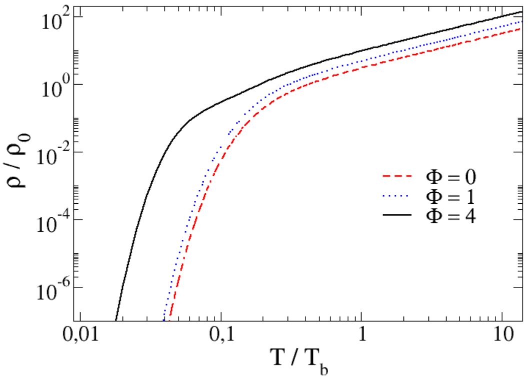

Figure 4.10: Magnetoresistivity in dependence of temperature T in units of $T_b = 2c_L b$ for boundary angle $\alpha = \pi/4$ and different values of magnetic flux with double-logarithmic scale. The other parameters are estimated as follows, $\mu = 0$, $Rb = 10$ and $c_L = 0.01v$. Adapted from Ref. [78].

and therefore, it can fall below the chemical potential. The magnetic flux shifts the band structure and provides that certain bands contribute to the resistivity. At low temperature, the resistivity then obtains a large increase, if intra-node backscattering becomes possible. This step is smears out for large temperatures.

4.4 Summary

This section has shown that the diverse band structure of a WSM nanowire represents very different features in transport properties compared to the TI nanowire. The setup involved a $\mathcal{P}$-symmetric WSM nanowire with a magnetic flux piercing the wire in direction parallel to the wire length. The band structure of a WSM nanowire depends on the magnetic flux. In case of Fermi arc states, it acts as a shift on the angular momentum j. An important aspect is that the curvature of the Fermi arcs is defined within the boundary condition by the angle α. This boundary angle ensures momentum conservation at the boundary [38].

Phonon-interaction at low-temperatures follows from longitudinal acoustic phonons assuming that the nanowire lies on a substrate. Electron-phonon coupling then follows from deformation potential coupling similar to the TI nanowire. This setup allows taking into account only longitudinal phonons with zero angular momentum. One expects the other modes to be gapped since the substrate reduces the deformations [66]. The study of the interaction with other phonon modes involves also other scattering processes. The scattering between the subbands then becomes possible, if the angular momentum is different from zero. Further, one can extend the model including a $\mathcal{T}$-symmetric WSM. A $\mathcal{T}$-symmetric WSM would have at least four Weyl nodes and possibly allow for more scattering processes. Both of this, however, is left for future work.

The consequences of the WSM band structure on transport properties already appeared in the zero temperature magnetoconductance. The zero temperature magnetoconductance increases or decreases in steps of $\Delta G_0 = \pm e^2/h$ or $\Delta G_0 = \pm 2e^2/h$ depending on the number of Fermi points that are added or removed from the chemical potential. This is quite different to the case of semiconductor wires [33]. Moreover, one finds a strong dependence on the parameterized boundary condition that changes the behavior. The number of Fermi points itself depends on number of subbands with angular momentum j. The boundary angle changes the curvature of the Fermi arcs and thus provides that they intersect the chemical potential. The magnetic flux shifts the band structure which leads to different bands contributing to the conductance. The magnetoconductance also presents a relation between the magnetic flux and the boundary angle.

The scattering processes induced by phonon interaction depend on how many Fermi momenta are given by one band. A band with one pair will act similar to the surface state of a TI nanowire. The total resistivity then depends on the sum over the inverse contribution of each channel since in a WSM more than one band can contribute. A two-valley band can intersect the chemical potential with up to two pairs of Fermi points. This allows for more scattering processes including intra-node scattering which at low temperatures leads to a large increase in resistivity. However, disorder effects have been absent in this study which are also present at low-temperatures and have been investigated without magnetic field so far [157]. Furthermore, the study on effects of the Zeeman field is relevant for a better comparison between the experiments and the theoretical model.

Thus, it was shown that the band structure in a WSM nanowire allows for very interesting features. The effects of the magnetic field have been studied for a magnetic field that is parallel to the wire axis and the Weyl nodes are separated in this direction as well. In chapter 2, the Weyl node separation perpendicular to the wire axis has been introduced [26]. Such a case can in principle not be solved without generalizing the model unless one assumes small perturbations. Moreover, the studied WSM is a type-I WSM. Type-II WSM materials have a tilted Weyl which show analogies to black hole physics [186]. Furthermore, pseudo-magnetic effects provide an interesting study according to their differences compared to electromagnetic fields [187].

Chapter 5

Summary and Outlook

This chapter presents a summary of this thesis beginning with the two materials, three dimensional topological insulators and Weyl semimetals, and their topological nature. Furthermore, it outlines the important results of phonon-induced backscattering and the magnetoresistance.

Topological insulators and Weyl semimetals were both introduced in chapter 2 as materials with topological nature. Quantized Hall conductance can be treated as an analogy to the Chern-number in materials. In topology the homotopy groups describe continuous deformations. This idea can be utilized to describe the mapping of a Bloch Hamiltonian in condensed matter physics. The quantum Hall effect requires a broken time-reversal symmetry that can for instance be given by a magnetic field. However, there exist also states that are time-reversal invariant and still considered topological, i.e. the quantum spin Hall state. The topology in such cases follows from spin-orbit interactions characterized by the $\mathbb{Z}_2$ topological invariant in a two dimensional topological insulator. In a three dimensional topological insulator four $\mathbb{Z}_2$ topological invariants determine the topology of the material. The topological semimetal has a topological invariant connected to the Berry curvature which is a topological quantity. The required broken symmetry within a three dimensional topological insulator films leads to the two dimensional quantum anomalous Hall effect. The anomalous Hall conductivity can be treated as critical point between ordinary and topological insulators.
Furthermore, chapter 2 focused on the materials and the transport properties of the topological insulators and Weyl semimetals. The three dimensional topological insulator, Bi_2Se_3, provides crystal symmetries. These are time-reversal symmetry, inversion symmetry as well as two- and threefold rotation symmetry. Moreover, the symmetries combined with spin-orbit interaction provide a single Dirac cone at the Γ-point that can be observed in ARPES measurements. The band structure well is approximated by a 4×4-Dirac Hamiltonian and describes gapped bulk bands and a conducting surface state. In Weyl semimetals, one observes Fermi arc surface states. These are an assembly of surface states at given Fermi energy connecting the Weyl nodes in the surface Brillouin zone. Weyl semimetals require a broken symmetry that splits the Weyl nodes apart. Their band structure consists of conducting surface and bulk states at the same time. Among several candidates, the Fermi arcs were observed in TaAs, first.

In chapter 3, the resistivity in a topological insulator nanowire was discussed. The topological insulator is a topological phase that provides conducting surface states while imposing a gapped bulk. The surface states in a topological insulator nanowire become topologically protected for half-integer flux. The model discussed in chapter 3 included electron-electron interaction within the bosonized Hamiltonian and electron-phonon interaction induced by acoustic phonons [67]. The phase diagram of the three dimensional topological insulator nanowires HgTe and Bi_2Te_3 presented orders of spin-density waves and superconducting phases. The conductivity at half-integer flux presented no effects of the interactions. However, if the flux is slightly away from half-integer, resistivity contributions follow from phonon-induced backscattering.

Chapter 4 presented the transport properties in a Weyl semimetal nanowire. The band structure of the Weyl semimetal nanowire followed from the parametrized boundary condition which ensured momentum conservation at the boundary. This allowed studying different curvatures of the Fermi arc. In agreement with previous work, the flat-bands were determined and the magnetoconductance showed similar behavior. Moreover, for different shapes of the Fermi arc dispersion, the magnetoconductance responded with different increase or decrease of conductance in steps of conductance quanta. Finally, the magnetoresistivity that followed from phonon-interaction as well, showed also different behavior depending on the shape of the contributing bands. Moreover, in contrast to the topological insulator nanowire, bands with two local extrema provided the possibility of more scattering processes.

In summary, this thesis discussed the effects of electron-phonon interaction in two different materials. Focusing on the topological insulator nanowire first, it was shown that given the half-integer magnetic flux that protects the surface state, the conductivity is not affected by electron-electron or electron-phonon interaction. The study of finite magnetic flux including electron-electron interaction is left for future work. The phase diagram showed that superconducting phases and spin density waves. The aspect that superconducting phases were still observable provides a promising basis for the Majorana bound states, for instance by proximity induced superconductivity implying a topological insulator nanowire on an s-wave superconductor. Regarding the Weyl semimetals, the conductance showed a connection between the Fermi arc curvature and the magnetic field which could allow gaining information about the curvature defining angle. Moreover, the magnetoresistivity can also be affected by other modes, if the wire is not setup on substrate that prevents other deformations. Further, the effects of the Zeeman fields are of interest for experiments. The studied Weyl semimetal has a broken time-reversal symmetry. Scattering effects in Weyl semimetals with broken inversion symmetry can be different, since such a material has at least four Weyl nodes. Furthermore, there exists another type of Weyl semimetals, the type-II Weyl semimetal, which has a tilted Weyl cone. A junction of these two types is for instance expected to act in analogy to black holes [186]. Especially the chiral anomaly appearing in Weyl semimetals is expected to show further interesting features also in tilted Weyl semimetals [188]. In conclusion, these topological phases have already shown their rich physics and one can expect more interesting research in this field.

List of publications

In the following, the publications included within this thesis are presented. The own contributions to the research are mentioned below as well.

PHASE DIAGRAM AND PHONON-INDUCED BACKSCATTERING IN TOPOLOGICAL INSULATOR NANOWIRES, PUBLISHED 3 JANUARY 2020 IN PHYSICAL REVIEW B

In this paper, the phase diagram of a TI nanowire was established and the effects of phonon-induced backscattering on transport properties were investigated. My contributions to this project involved the derivation of the Green's function. Therefore, I solved the Gaussian functional integral estimated the electron-phonon coupling parameter. Furthermore, I derived the order fluctuations for the topological insulator nanowire and computed the phase diagram. I was involved in the conductivity derivation by solving the current-current correlation function at half-integer magnetic flux.

Reference: Kathrin Dorn, Alessandro De Martino, and Reinhold Egger. *Phase diagram and phonon-induced backscattering in topological insulator nanowires.* Phys. Rev. B 101.045402 (2020).

PHONON-INDUCED MAGNETORESISTIVITY OF WEYL SEMIMETAL NANOWIRES, PUBLISHED 19 OCTOBER 2021 IN PHYSICAL REVIEW B

In this project, the Weyl semimetal band structure of a Weyl semimetal nanowire was established and the transport properties were investigated. I determined the parametrized boundary condition and applied it to the nanowire setup and computed the numerical band structures. Moreover, I calculated the probability density numerically. The numerical evaluation of the conductance plots was done by me. This includes the dependence of the conductance on the boundary angle, the magnetic flux and the chemical potential. Furthermore, I was involved in the numerical implementation of the resistivity plots where I found the origin of the abrupt resistivity changes.

Reference: Alessandro De Martino, Kathrin Dorn, Francesco Buccheri, and Reinhold Egger. *Phonon-induced magnetoresistivity of Weyl semimetal nanowires.* Phys. Rev. B 104, 155425 (2021)
Preprint available on arXiv: https://arxiv.org/abs/2110.05149 .

Appendix A

Topological insulator

A.1 Parameters in the effective Hamiltonian

The parameters of the effective Hamiltonian describing Bi_2Se_3 were determined by putting it in contrast to *ab initio* calculations. Therefore, the energy spectrum which follows from the model Hamiltonian was solved and compared with the spectrum obtained by *ab initio* calculations. Moreover, the following parameters were established with this method for Bi_2Se_3 (s.Ref. [61]) and for Bi_2Te_3 (s.Ref. [52]).

Parameter	Bi_2Se_3	Bi_2Te_3
$\mathcal{A}_1$	$2.2\,\mathrm{eV\AA}$	$0.3\,\mathrm{eV\AA}$
$\mathcal{A}_2$	$4.1\,\mathrm{eV\AA}$	$2.87\,\mathrm{eV\AA}$
C	$-0.0068\,\mathrm{eV}$	$-0.18\,\mathrm{eV}$
D_1	$1.3\,\mathrm{eV\AA}^2$	$6.55\,\mathrm{eV\AA}^2$
D_2	$19.6\,\mathrm{eV\AA}^2$	$19.6\,\mathrm{eV\AA}^2$
M	$0.28\,\mathrm{eV}$	$0.30\,\mathrm{eV}$
B_1	$10\,\mathrm{eV\AA}^2$	$2.79\,\mathrm{eV\AA}^2$
B_2	$56.6\,\mathrm{eV\AA}^2$	$57.38\,\mathrm{eV\AA}^2$

Table A.1: Parameter set for 3DTI of the $D_{3d}^5(R\bar{3}m)$ space group with rhombohedral crystal structure. Table adapted from Ref. [61] and [52].

Appendix B

Bessel- and Hypergeometric functions

B.1 Identities of Bessel functions

The following identities of Bessel functions have been used throughout this thesis [131, 178]:

Definition

The Bessel's equation is given by

$$0 = z^2 \frac{d^2u}{dz^2} + z\frac{du}{dz} + s(z^2 - sn^2)u \tag{B.1}$$

where $s = +$ corresponds to the Bessel's equation and leads to the solution of Bessel functions $J_n(z)$ and $Y_n(z)$, while $s = -$ corresponds to the modified Bessel's equation and leads to the modified Bessel functions. The Bessel's equation provides a regular singularity at the origin and an irregular singularity, if $z \to \infty$. The modified Bessel's equation obtains equivalent singularities by setting $z \to iz$. The Bessel function of the first kind is defined by

$$J_n(z) = \left(\frac{z}{2}\right)^n \sum_{m=0}^{\infty} (-1)^m \frac{\left(\frac{z^2}{4}\right)^m}{m!\Gamma(n+m+1)} \tag{B.2}$$

and the modified Bessel function of the first kind is given by

$$I_n(z) = \left(\frac{z}{2}\right)^n \sum_{m=0}^{\infty} \frac{\left(\frac{z^2}{4}\right)^m}{m!\Gamma(n+m+1)} \ . \tag{B.3}$$

Recurrence relations

The following recurrence relations were used:

$$J'_\nu(z) = J_{\nu-1}(z) - \frac{\nu}{z} J_\nu(z) \tag{B.4}$$

$$J'_\nu(z) = -J_{\nu+1}(z) + \frac{\nu}{z} J_\nu(z) \tag{B.5}$$

$$2J'_\nu(z) = J_{\nu-1}(z) - J_{\nu+1}(z) \tag{B.6}$$

$$(2\nu/z)J_\nu(z) = J_{\nu-1}(z) + J_{\nu+1}(z) \tag{B.7}$$

$$I'_\nu(z) = I_{\nu+1}(z) + \frac{\nu}{z} I_\nu(z) \tag{B.8}$$

$$I'_\nu(z) = I_{\nu-1}(z) - \frac{\nu}{z} I_\nu(z) \tag{B.9}$$

Connection between Bessel-functions

The modified Bessel-function is conntected by

$$J_{j\pm 1/2}(-i\kappa R) = i^{j\pm 1/2} I_{j\pm 1/2}(\kappa R) \tag{B.10}$$

to the Bessel-function of the first kind.

Limits of Bessel-functions

The limit of Bessel functions with large argument is

$$I_\nu(z) \approx \frac{e^z}{\sqrt{2\pi z}} \left(1 - \frac{4\nu^2 - 1}{8z}\right) \tag{B.11}$$

and

$$J_\nu(z) \approx \sqrt{\frac{2}{\pi z}} \cos\left(z - \frac{\nu\pi}{2} - \frac{\pi}{4}\right) \ . \tag{B.12}$$

B.2 Identities of the confluent hypergeometric functions

The following identities of the confluent hypergeometric function have been used throughout this thesis [131, 177, 178]:

Definition

The confluent hypergeometric equation, or Kummer's equation, is given by

$$0 = z\frac{d^2u}{dz^2} + (b - z)\frac{du}{dz} - au \tag{B.13}$$

with a regular singularity for $z \to 0$ and an irregular singularity for $z \to \infty$. Kummer's function follows from the differential equation above

$$M(a, b, z) = \sum_{\nu=0}^{\infty} \frac{(a)_\nu}{(b)_\nu \nu!} z^\nu \tag{B.14}$$

where $(c)_n$ is Pochhammer's symbol. The confluent hypergeometric function is also named $\Phi(a, b, z)$ or ${}_1F_1(a, b, z)$.

Derivatives

The following derivatives were applied in this note:

$$\frac{d}{dz} M(a, b, z) = \frac{a}{b} M(a + 1, b + 1, z) \tag{B.15}$$

Relation of the solutions of the confluent hypergeometric function

Kummer's transformation yields

$$M(a,b,z) = e^{z} M(b-a,b,-z)\ . \tag{B.16}$$

The relation between $M(a,b,z)$ and $U(a,b,z)$ is

$$U(a,b,z) = \frac{\pi}{\sin(\pi b)}\left[\frac{M(a,b,z)}{\Gamma(1+a-b)\Gamma(b)} - z^{1-b}\frac{M(1+a-b,2-b,z)}{\Gamma(a)\Gamma(2-b)}\right]\ . \tag{B.17}$$

Appendix C

Weyl semimetal nanowire

This chapter of the appendix also follows Ref. [78] (preprint s.Ref. [175]) and covers the derivations of the band structure for $\alpha = \pi/2$, the Fermi arc solution and the toy model mentioned in Sec.4.3.2.

C.1 Band structure for $\alpha = \pi/2$ and different limits of magnetic flux

Among the certain limits of the confluent hypergeometric function, the band structure for $\alpha = \pi/2$ can be computed exactly. Setting $\alpha = \pi/2$ leads to the boundary condition $Y_-(\Phi) = 0$. This yields two possible solutions. The first one considers $\mathcal{E}_- = 0$ and $j > 0$ that leads to the radial eigenfunction

$$Y_{k,j>0,0}(\xi) \propto \xi^{\frac{1}{2}\left(j-\frac{1}{2}\right)} e^{\xi/2} \begin{pmatrix} 1 \\ 0 \end{pmatrix} \tag{C.1}$$

of a radial band index $p = 0$. The corresponding energy dispersion relation is given by

$$E_{k,j>0,0} = m_k \tag{C.2}$$

and thus it is equal to the result of the Fermi arc dispersion in Eq.(4.18) at $\alpha = \pi/2$. The dispersion is presented in Fig.4.1. The other bands follow from the zeros of the confluent hypergeometric function in $M(a, j + 3/2; \Phi) = 0$. The zeros are given by $a = a_{j,p}$ for any j and $p = 1, 2, \ldots$. Therefore, one obtains the energy

$$E_{k,j,\pm p} = \pm\sqrt{\frac{2C_{j,p}v^2}{l_B^2} + m_k^2} \tag{C.3}$$

with $C_{j>0,p} = j + 1/2 - a_{j,p}$ where the zeros $a_{j,p}$ correspond to negative numbers. However, no bands with $p = 0$ exist for $j < 0$ and finite radius. Hence, one finds $C_{j<0,p} = -a_{-(j+1),p}$ implying that the bands appear pairwise as shown in Fig.4.1.

Considering the limit of small magnetic flux, first, one finds that the dispersion in Eq.(C.2) remains unchanged, since it does not depend on the radius or the magnetic length. However, the radial eigenfunction in Eq.(C.1) does depend on the magnetic flux and,thus, it reduces to

$$Y_{k,j>0,0}(r) \propto r^{j-\frac{1}{2}} \begin{pmatrix} 1 \\ 0 \end{pmatrix} \tag{C.4}$$

describing degenerate Fermi surface arc states. Eq.(C.3) yields bulk states with dispersion

$$E_{k,j,\pm p} = \pm\sqrt{\left(\frac{v z_{j,p}}{R}\right)^2 + m_k^2} \tag{C.5}$$

including the pth zero of the Bessel function of the first kind $J_{j+1/2}(z)$. The bulk states correspond to a finite-size quantization of v/R of the energy scale.
Second, in the limit of very large magnetic flux, which is still finite, one finds the bulk Landau spectrum that is described by Eq.(4.20). The main aspects are presented here as well. The zeros of the confluent hypergeometric functions yield $a_{j,p} \to -(p-1)$, where p is an integer leading to the Landau Level spectrum. One observes that the Fermi arc with $j > 0$ and $p = 0$ vanishes for infinite radius. Moreover, an avoided crossing appears at $m = 0$ following from the eigenstate $\Psi_{k,j<0,\pm 1}$ with the dispersion $E = \pm|m_k|$, since $a = 0$ cannot be a solution of $M(-p+1, -j+1/2; \Phi) = 0$. In the limit of infinite radius, one finds that the positive dispersion vanishes and $E = -m_k$ becomes a bulk zero mode.

C.2 Fermi arc dispersion

Following Ref. [78], the Fermi arc dispersion in a WSM nanowire is given by the approximation

$$E_{k,j} = \frac{v(j+\Phi)}{R}\cos(\alpha) + m_k \sin(\alpha) \tag{C.6}$$

with the condition defining the range

$$\frac{v(j+\Phi)}{R}\sin(\alpha) - m_k\cos(\alpha) > 0\ . \tag{C.7}$$

Fig.C.1 represents the numerical and analytical Fermi arc dispersions for $j = \pm 1/2$ for $\alpha = 0$ and $\alpha = \pi/4$ with magnetic flux Φ. Although $j = -1/2$ for a magnetic flux $\Phi = 1/2$, the approximation fits well. However, for positive angular momenta the approximation fits better. Moreover, the boundary condition shows that the magnetic field is involved in the first parameter which differs for positive and negative angular momenta. Regarding to Eq.(4.19) the approximation deviates from the numerical band structure at the Weyl nodes. This also stays in agreement with Fig.C.1.

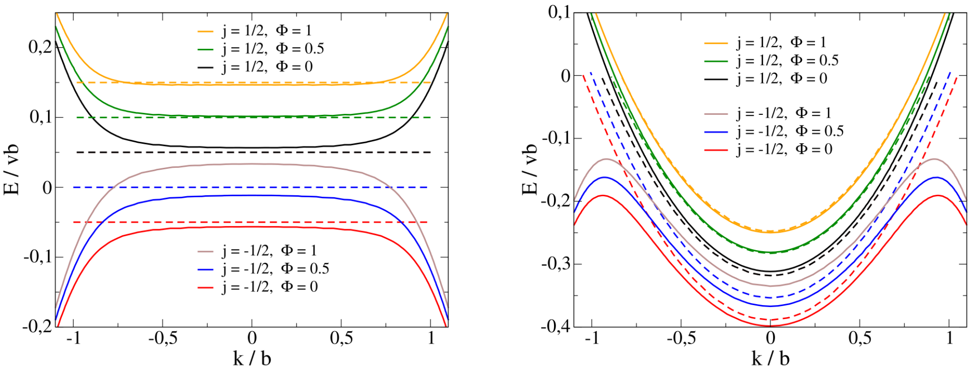

Figure C.1: Fermi arc dispersion relation plotted numerically (solid lines) and analytically (dashes lines). The bands represent angular momentum $j = 1/2$ and $j = -1/2$ for $\Phi = 0, 0.5$ and 1. The dispersion relation in Eq.(C.6) yields the same result for $j = 1/2$ at $\Phi = 0$ and for $j = -1/2$ and $\Phi = 1$. Adapted from Ref. [78].

C.3 Toy model

For a better understanding of the abrupt changes in the phonon-induced resistivity in Fig.4.8 and 4.9 this toy model dispersion

$$\epsilon_k = -|k^2 - 1| \tag{C.8}$$

is utilized to describe a simple two valley band with $v = b = 1$. Following Ref. [78] the model shall represent the case in in Fig.4.9 where the chemical potential is below zero and is intersected by one pair of Fermi points $\pm k_+$ with Fermi velocity v_+ for $\mu < \mu_c$. If $\mu > \mu_c$, two pairs of Fermi points $k_\pm$ intersect the chemical potential. From $\epsilon_k = \mu$ follows that the Fermi momenta are given by $k_\pm = \sqrt{1 \pm |\mu|}$ with corresponding Fermi velocity $v_\pm = 2\sqrt{1 \pm |\mu|}$.

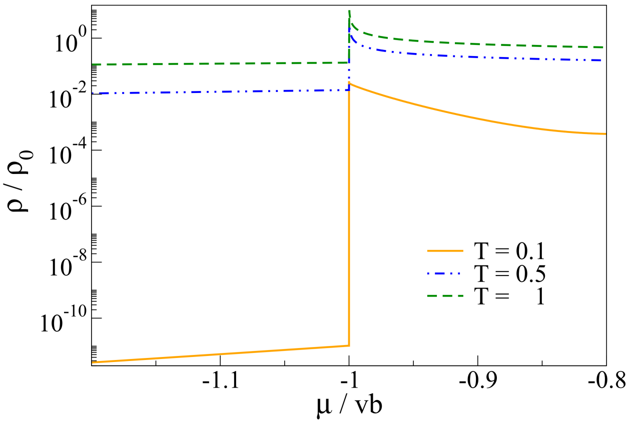

Figure C.2: Resistivity of a toy model dispersion for a two-valley band in dependence of the chemical potential μ in units of vb. The critical chemical potential μ_c defines the point, where the number of Fermi point pairs changes between one and two pairs. The overlap-integral is set $\mathcal{I}_{k_+,k_-} = 0.5$. The temperature is given units of $T_b = 2c_L b$. Please note the logarithmic scale. Adapted from Ref. [78].

The resistivity in Fig.C.2 shows the expected abrupt increase of resistivity at $\mu = \mu_c \approx 1$ as $\mu \to 0$. The critical value of the chemical potential determines that $k = 0$, where the band has its local minimum. The contribution to the resistivity for $\mu < \mu_c$ arises from inter-node backscattering with a Bloch-Grüneisen scale of $T_{BG} = 2c_L k_+$. For $\mu > \mu_c$, intra-node backscattering processes provide the dominant contribution due to a much smaller Bloch-Grüneisen temperature $T_{BG} = c_L(k_+ - k_-)$. These processes yield a much higher resistivity than the inter-node backscattering. This difference between the resistivity values results in the sudden change. Eventually, this jump is a consequence of the transition between the number of Fermi points.

Bibliography

[1] Markus König, Steffen Wiedmann, Christoph Brüne, Andreas Roth, Hartmut Buhmann, Laurens W. Molenkamp, Xiao-Liang Qi, and Shou-Cheng Zhang. Quantum Spin Hall Insulator State in HgTe Quantum Wells. *Science*, 318(5851):766–770, 2007.

[2] Paul Adrien Maurice Dirac. The quantum theory of the electron. *Proc. R. Soc. Lond. A*, 117:610, 1928.

[3] Hermann Weyl. Elektron und Gravitation I. *Zeitschrift Physik*, 56:330, 1929.

[4] K. v. Klitzing, G. Dorda, and M. Pepper. New Method for High-Accuracy Determination of the Fine-Structure Constant Based on Quantized Hall Resistance. *Phys. Rev. Lett.*, 45:494–497, Aug 1980.

[5] D. J. Thouless, M. Kohmoto, M. P. Nightingale, and M. den Nijs. Quantized Hall Conductance in a Two-Dimensional Periodic Potential. *Phys. Rev. Lett.*, 49:405–408, Aug 1982.

[6] C. L. Kane and E. J. Mele. Quantum Spin Hall Effect in Graphene. *Phys. Rev. Lett.*, 95:226801, Nov 2005.

[7] Liang Fu and C. L. Kane. Topological insulators with inversion symmetry. *Phys. Rev. B*, 76:045302, Jul 2007.

[8] Liang Fu, C. L. Kane, and E. J. Mele. Topological Insulators in Three Dimensions. *Phys. Rev. Lett.*, 98:106803, Mar 2007.

[9] Markus König, Hartmut Buhmann, Laurens W. Molenkamp, Taylor Hughes, Chao-Xing Liu, Xiao-Liang Qi, and Shou-Cheng Zhang. The Quantum Spin Hall Effect: Theory and Experiment. *Journal of the Physical Society of Japan*, 77(3):031007, 2008.

[10] David Hsieh, Dong Qian, Lewis Wray, Yiman Xia, Yew San Hor, Robert Joseph Cava, and M Zahid Hasan. A topological Dirac insulator in a quantum spin Hall phase. *Nature*, 452(7190):970–974, 2008.

[11] Andrea Damascelli, Zahid Hussain, and Zhi-Xun Shen. Angle-resolved photoemission studies of the cuprate superconductors. *Rev. Mod. Phys.*, 75:473–541, Apr 2003.

[12] Yuqi Xia, Dong Qian, David Hsieh, L Wray, Arijeet Pal, Hsin Lin, Arun Bansil, DHYS Grauer, Yew San Hor, Robert Joseph Cava, et al. Observation of a large-gap

topological-insulator class with a single Dirac cone on the surface. *Nature physics*, 5(6):398–402, 2009.

[13] A. A. Burkov and Leon Balents. Weyl Semimetal in a Topological Insulator Multilayer. *Phys. Rev. Lett.*, 107:127205, Sep 2011.

[14] Su-Yang Xu, Ilya Belopolski, Nasser Alidoust, Madhab Neupane, Guang Bian, Chenglong Zhang, Raman Sankar, Guoqing Chang, Zhujun Yuan, Chi-Cheng Lee, Shin-Ming Huang, Hao Zheng, Jie Ma, Daniel S. Sanchez, BaoKai Wang, Arun Bansil, Fangcheng Chou, Pavel P. Shibayev, Hsin Lin, Shuang Jia, and M. Zahid Hasan. Discovery of a Weyl fermion semimetal and topological Fermi arcs. *Science*, 349(6248):613–617, 2015.

[15] M. Zahid Hasan, Su-Yang Xu, Ilya Belopolski, and Shin-Ming Huang. Discovery of Weyl Fermion Semimetals and Topological Fermi Arc States. *Annual Review of Condensed Matter Physics*, 8(1):289–309, 2017.

[16] B. Q. Lv, H. M. Weng, B. B. Fu, X. P. Wang, H. Miao, J. Ma, P. Richard, X. C. Huang, L. X. Zhao, G. F. Chen, Z. Fang, X. Dai, T. Qian, and H. Ding. Experimental Discovery of Weyl Semimetal TaAs. *Phys. Rev. X*, 5:031013, Jul 2015.

[17] Hongming Weng, Chen Fang, Zhong Fang, B. Andrei Bernevig, and Xi Dai. Weyl Semimetal Phase in Noncentrosymmetric Transition-Metal Monophosphides. *Phys. Rev. X*, 5:011029, Mar 2015.

[18] B. Q. Lv, T. Qian, and H. Ding. Experimental perspective on three-dimensional topological semimetals. *Rev. Mod. Phys.*, 93:025002, Apr 2021.

[19] R. Egger, A. Zazunov, and A. Levy Yeyati. Helical Luttinger Liquid in Topological Insulator Nanowires. *Phys. Rev. Lett.*, 105:136403, Sep 2010.

[20] J. Ziegler, R. Kozlovsky, C. Gorini, M.-H. Liu, S. Weishäupl, H. Maier, R. Fischer, D. A. Kozlov, Z. D. Kvon, N. Mikhailov, S. A. Dvoretsky, K. Richter, and D. Weiss. Probing spin helical surface states in topological HgTe nanowires. *Phys. Rev. B*, 97:035157, Jan 2018.

[21] Hailin Peng, Keji Lai, Desheng Kong, Stefan Meister, Yulin Chen, Xiao-Liang Qi, Shou-Cheng Zhang, Zhi-Xun Shen, and Yi Cui. Aharonov–Bohm interference in topological insulator nanoribbons. *Nature materials*, 9(3):225–229, 2010.

[22] J. H. Bardarson, P. W. Brouwer, and J. E. Moore. Aharonov-Bohm Oscillations in Disordered Topological Insulator Nanowires. *Phys. Rev. Lett.*, 105:156803, Oct 2010.

[23] Jens H Bardarson and Joel E Moore. Quantum interference and Aharonov–Bohm oscillations in topological insulators. *Reports on Progress in Physics*, 76(5):056501, apr 2013.

[24] Vardan Kaladzhyan and Jens H. Bardarson. Quantized Fermi arc mediated transport in Weyl semimetal nanowires. *Phys. Rev. B*, 100:085424, Aug 2019.

[25] Pavlo O. Sukhachov, Mykhailo V. Rakov, Olena M. Teslyk, and Eduard V. Gorbar. Fermi Arcs and DC Transport in Nanowires of Dirac and Weyl Semimetals. *Annalen der Physik*, 532(2):1900449, Jan 2020.

[26] Akira Igarashi and Mikito Koshino. Magnetotransport in Weyl semimetal nanowires. *Phys. Rev. B*, 95:195306, May 2017.

[27] Sébastien Giraud and Reinhold Egger. Electron-phonon scattering in topological insulators. *Phys. Rev. B*, 83:245322, Jun 2011.

[28] Sébastien Giraud, Arijit Kundu, and Reinhold Egger. Electron-phonon scattering in topological insulator thin films. *Phys. Rev. B*, 85:035441, Jan 2012.

[29] H. K. Pal, V. I. Yudson, and D. L. Maslov. Effect of electron-electron interaction on surface transport in the Bi_2Te_3 family of three-dimensional topological insulators. *Phys. Rev. B*, 85:085439, Feb 2012.

[30] Henrik Bruus and Karsten Flensberg. *Many-Body Quantum Theory in Condensed Matter Physics: An Antroduction*. OUP Oxford, 2004.

[31] Daniel Loss and Thierry Martin. Wentzel-Bardeen singularity and phase diagram for interacting electrons coupled to acoustic phonons in one dimension. *Phys. Rev. B*, 50:12160–12163, Oct 1994.

[32] A.O. Gogolin, A.A. Nersesyan, and A.M. Tsvelik. *Bosonization and Strongly Correlated Systems*. Cambridge University Press, 2004.

[33] V. L. Gurevich, V. B. Pevzner, and K. Hess. Phonon-assisted ballistic resistance. *Phys. Rev. B*, 51:5219–5226, Feb 1995.

[34] G.D. Mahan. *Many-Particle Physics*. Physics of Solids and Liquids. Springer US, 2000.

[35] Michele Burrello, Enore Guadagnini, Luca Lepori, and Mihail Mintchev. Field theory approach to the quantum transport in Weyl semimetals. *Phys. Rev. B*, 100:155131, Oct 2019.

[36] Nityan L. Nair, Marie-Eve Boulanger, Francis Laliberté, Sinead Griffin, Sanyum Channa, Anaelle Legros, Wojciech Tabis, Cyril Proust, Jeffrey Neaton, Louis Taillefer, and James G. Analytis. Signatures of possible surface states in TaAs. *Phys. Rev. B*, 102:075402, Aug 2020.

[37] I. A. Cohn, S. G. Zybtsev, A. P. Orlov, and S. V. Zaitsev-Zotov. Magnetoresistance in Quasi-One-Dimensional Weyl Semimetal $(TaSe_4)_2I$. *JETP Letters*, 112(2):88–94, Jul 2020.

[38] Edward Witten. Three Lectures On Topological Phases Of Matter, 2015.

[39] B.A. Bernevig and T.L. Hughes. *Topological Insulators and Topological Superconductors*. Princeton University Press, 2013.

[40] M.E. Peskin and D.V. Schroeder. *An Introduction to Quantum Field Theory*. CRC Press LLC, 2019.

[41] F. Schwabl. *Quantenmechanik für Fortgeschrittene (QM II)*. Springer-Lehrbuch. Springer, 2005.

[42] Rudolf Gross and Achim Marx. *Festkörperphysik*. De Gruyter, 2018.

[43] Palash B. Pal. Dirac, Majorana, and Weyl fermions. *American Journal of Physics*, 79(5):485–498, 2011.

[44] Michael Victor Berry. Quantal phase factors accompanying adiabatic changes. *Proceedings of the Royal Society of London. A. Mathematical and Physical Sciences*, 392(1802):45–57, 1984.

[45] M. Nakahara and M. Delbrück. *Differentialgeometrie, Topologie und Physik*. Springer Berlin Heidelberg, 2015.

[46] Y. Aharonov and D. Bohm. Significance of Electromagnetic Potentials in the Quantum Theory. *Phys. Rev.*, 115:485–491, Aug 1959.

[47] F. D. M. Haldane. Berry Curvature on the Fermi Surface: Anomalous Hall Effect as a Topological Fermi-Liquid Property. *Phys. Rev. Lett.*, 93:206602, Nov 2004.

[48] J. E. Avron, R. Seiler, and B. Simon. Homotopy and Quantization in Condensed Matter Physics. *Phys. Rev. Lett.*, 51:51–53, Jul 1983.

[49] J. E. Moore and L. Balents. Topological invariants of time-reversal-invariant band structures. *Phys. Rev. B*, 75:121306, Mar 2007.

[50] R. B. Laughlin. Quantized Hall conductivity in two dimensions. *Phys. Rev. B*, 23:5632–5633, May 1981.

[51] C. L. Kane and E. J. Mele. Z_2 Topological Order and the Quantum Spin Hall Effect. *Phys. Rev. Lett.*, 95:146802, Sep 2005.

[52] Xiao-Liang Qi and Shou-Cheng Zhang. Topological insulators and superconductors. *Rev. Mod. Phys.*, 83:1057–1110, Oct 2011.

[53] M. Z. Hasan and C. L. Kane. Colloquium: Topological insulators. *Rev. Mod. Phys.*, 82:3045–3067, Nov 2010.

[54] Rahul Roy. Topological phases and the quantum spin Hall effect in three dimensions. *Phys. Rev. B*, 79:195322, May 2009.

[55] H.B. Nielsen and Masao Ninomiya. The Adler-Bell-Jackiw anomaly and Weyl fermions in a crystal. *Physics Letters B*, 130(6):389–396, 1983.

[56] A.A. Burkov. Weyl Metals. *Annual Review of Condensed Matter Physics*, 9(1):359–378, 2018.

[57] N. P. Armitage, E. J. Mele, and Ashvin Vishwanath. Weyl and Dirac semimetals in three-dimensional solids. *Rev. Mod. Phys.*, 90:015001, Jan 2018.

[58] Mahito Kohmoto, Bertrand I. Halperin, and Yong-Shi Wu. Diophantine equation for the three-dimensional quantum Hall effect. *Phys. Rev. B*, 45:13488–13493, Jun 1992.

[59] Ettore Majorana. Teoria simmetrica dell'elettrone e del positrone. *Il Nuovo Cimento (1924-1942)*, 14(4):171–184, 1937.

[60] Alexei Kitaev. Periodic table for topological insulators and superconductors. *AIP Conference Proceedings*, 1134(1):22–30, 2009.

[61] Haijun Zhang, Chao-Xing Liu, Xiao-Liang Qi, Xi Dai, Zhong Fang, and Shou-Cheng Zhang. Topological insulators in bi_2se_3, bi_2te_3 and sb_2te_3 with a single Dirac cone on the surface. *Nature physics*, 5(6):438–442, 2009.

[62] Chao-Xing Liu, Xiao-Liang Qi, HaiJun Zhang, Xi Dai, Zhong Fang, and Shou-Cheng Zhang. Model Hamiltonian for topological insulators. *Phys. Rev. B*, 82:045122, Jul 2010.

[63] Baiqing Lv, Tian Qian, and Hong Ding. Angle-resolved photoemission spectroscopy and its application to topological materials. *Nature Reviews Physics*, 1(10):609–626, 2019.

[64] David Hsieh, Yuqi Xia, Dong Qian, L Wray, JH Dil, Fedorov Meier, J Osterwalder, L Patthey, JG Checkelsky, Nai Phuan Ong, et al. A tunable topological insulator in the spin helical Dirac transport regime. *Nature*, 460(7259):1101–1105, 2009.

[65] Arijit Kundu, Alex Zazunov, Alfredo Levy Yeyati, Thierry Martin, and Reinhold Egger. Energy spectrum and broken spin-surface locking in topological insulator quantum dots. *Phys. Rev. B*, 83:125429, Mar 2011.

[66] L.D. Landau, L.P. Pitaevskii, A.M. Kosevich, and E.M. Lifshitz. *Theory of Elasticity: Volume 7*. Number Bd. 7. Berlin Akad.-Verl., 1991.

[67] Kathrin Dorn, Alessandro De Martino, and Reinhold Egger. Phase diagram and phonon-induced backscattering in topological insulator nanowires. *Phys. Rev. B*, 101:045402, Jan 2020.

[68] C. Brüne, C. X. Liu, E. G. Novik, E. M. Hankiewicz, H. Buhmann, Y. L. Chen, X. L. Qi, Z. X. Shen, S. C. Zhang, and L. W. Molenkamp. Quantum Hall Effect from the Topological Surface States of Strained Bulk HgTe. *Phys. Rev. Lett.*, 106:126803, Mar 2011.

[69] Shu-Chun Wu, Binghai Yan, and Claudia Felser. Ab initio study of topological surface states of strained HgTe. *EPL (Europhysics Letters)*, 107(5):57006, sep 2014.

[70] P Baireuther, J A Hutasoit, J Tworzydło, and C W J Beenakker. Scattering theory of the chiral magnetic effect in a Weyl semimetal: interplay of bulk Weyl cones and surface Fermi arcs. *New Journal of Physics*, 18(4):045009, apr 2016.

[71] N Bovenzi, M Breitkreiz, T E O'Brien, J Tworzydło, and C W J Beenakker. Twisted Fermi surface of a thin-film Weyl semimetal. *New Journal of Physics*, 20(2):023023, feb 2018.

[72] Shuichi Murakami and Shun-ichi Kuga. Universal phase diagrams for the quantum spin Hall systems. *Phys. Rev. B*, 78:165313, Oct 2008.

[73] Stephen L. Adler. Axial-Vector Vertex in Spinor Electrodynamics. *Phys. Rev.*, 177:2426–2438, Jan 1969.

[74] John S Bell and Roman Jackiw. A PCAC puzzle: $\pi\ 0 \rightarrow \gamma\gamma$ in the σ-model. *Il Nuovo Cimento A (1965-1970)*, 60(1):47–61, 1969.

[75] A A Burkov. Chiral anomaly and transport in Weyl metals. *Journal of Physics: Condensed Matter*, 27(11):113201, feb 2015.

[76] Y. Chen, Si Wu, and A. A. Burkov. Axion response in Weyl semimetals. *Phys. Rev. B*, 88:125105, Sep 2013.

[77] Christoph W Groth, Michael Wimmer, Anton R Akhmerov, and Xavier Waintal. Kwant: a software package for quantum transport. *New Journal of Physics*, 16(6):063065, jun 2014.

[78] Alessandro De Martino, Kathrin Dorn, Francesco Buccheri, and Reinhold Egger. Phonon-induced magnetoresistivity of Weyl semimetal nanowires. *Phys. Rev. B*, 104:155425, Oct 2021.

[79] Binghai Yan and Claudia Felser. Topological Materials: Weyl Semimetals. *Annual Review of Condensed Matter Physics*, 8(1):337–354, 2017.

[80] Shin-Ming Huang, Su-Yang Xu, Ilya Belopolski, Chi-Cheng Lee, Guoqing Chang, BaoKai Wang, Nasser Alidoust, Guang Bian, Madhab Neupane, Chenglong Zhang, et al. A Weyl Fermion semimetal with surface Fermi arcs in the transition metal monopnictide TaAs class. *Nature communications*, 6(1):1–6, 2015.

[81] A. Altland and B.D. Simons. *Condensed Matter Field Theory*. Cambridge books online. Cambridge University Press, 2010.

[82] R. Egger, A. Bachtold, M. S. Fuhrer, M. Bockrath, D. H. Cobden, and P. L. McEuen. Luttinger liquid behavior in metallic carbon nanotubes. In Rolf Haug and Herbert Schoeller, editors, *Interacting Electrons in Nanostructures*, pages 125–146, Berlin, Heidelberg, 2001. Springer Berlin Heidelberg.

[83] Yaroslav Tserkovnyak, Bertrand I. Halperin, Ophir M. Auslaender, and Amir Yacoby. Interference and zero-bias anomaly in tunneling between Luttinger-liquid wires. *Phys. Rev. B*, 68:125312, Sep 2003.

[84] D. Sénéchal. *An Introduction to Bosonization*, pages 139–186. Springer New York, New York, NY, 2004.

[85] Matthew P. A. Fisher and Leonid I. Glazman. *Transport in a One-Dimensional Luttinger Liquid*, pages 331–373. Springer Netherlands, Dordrecht, 1997.

[86] T. Giamarchi. *Quantum Physics in One Dimension*. International Series of Monographs on Physics. Clarendon Press, 2003.

[87] Reinhold Egger and Alexander O. Gogolin. Effective Low-Energy Theory for Correlated Carbon Nanotubes. *Phys. Rev. Lett.*, 79:5082–5085, Dec 1997.

[88] Reinhold Egger and Alexander O Gogolin. Correlated transport and non-Fermi-liquid behavior in single-wall carbon nanotubes. *The European Physical Journal B-Condensed Matter and Complex Systems*, 3(3):281–300, 1998.

[89] Ryogo Kubo, Mario Yokota, and Sadao Nakajima. Statistical-Mechanical Theory of Irreversible Processes. II. Response to Thermal Disturbance. *Journal of the Physical Society of Japan*, 12(11):1203–1211, 1957.

[90] Alex Levchenko and Jörg Schmalian. Transport properties of strongly coupled electron-phonon liquids. *Annals of Physics*, 419:168218, 2020.

[91] Peter Thalmeier. Surface phonon propagation in topological insulators. *Phys. Rev. B*, 83:125314, Mar 2011.

[92] Jan Carl Budich, Fabrizio Dolcini, Patrik Recher, and Björn Trauzettel. Phonon-Induced Backscattering in Helical Edge States. *Phys. Rev. Lett.*, 108:086602, Feb 2012.

[93] Solofo Groenendijk, Giacomo Dolcetto, and Thomas L. Schmidt. Fundamental limits to helical edge conductivity due to spin-phonon scattering. *Phys. Rev. B*, 97:241406, Jun 2018.

[94] Ion Garate. Phonon-Induced Topological Transitions and Crossovers in Dirac Materials. *Phys. Rev. Lett.*, 110:046402, Jan 2013.

[95] P. Zhang and M. W. Wu. Hot-carrier transport and spin relaxation on the surface of topological insulator. *Phys. Rev. B*, 87:085319, Feb 2013.

[96] V. Parente, A. Tagliacozzo, F. von Oppen, and F. Guinea. Electron-phonon interaction on the surface of a three-dimensional topological insulator. *Phys. Rev. B*, 88:075432, Aug 2013.

[97] S. Das Sarma and Qiuzi Li. Many-body effects and possible superconductivity in the two-dimensional metallic surface states of three-dimensional topological insulators. *Phys. Rev. B*, 88:081404, Aug 2013.

[98] M. Q. Weng and M. W. Wu. High-field charge transport on the surface of $\mathrm{Bi_2Se_3}$. *Phys. Rev. B*, 90:125306, Sep 2014.

[99] Rolf Heid, Irina Yu Sklyadneva, and Evgueni V Chulkov. Electron-phonon coupling in topological surface states: The role of polar optical modes. *Scientific reports*, 7(1):1–9, 2017.

[100] Xuetao Zhu, L. Santos, R. Sankar, S. Chikara, C. . Howard, F. C. Chou, C. Chamon, and M. El-Batanouny. Interaction of phonons and dirac fermions on the surface of $\mathrm{bi_2se_3}$: A strong kohn anomaly. *Phys. Rev. Lett.*, 107:186102, Oct 2011.

[101] Richard C. Hatch, Marco Bianchi, Dandan Guan, Shining Bao, Jianli Mi, Bo Brummerstedt Iversen, Louis Nilsson, Liv Hornekær, and Philip Hofmann. Stability of the $\mathrm{Bi_2Se_3}$(111) topological state: Electron-phonon and electron-defect scattering. *Phys. Rev. B*, 83:241303, Jun 2011.

[102] Xuetao Zhu, L. Santos, C. Howard, R. Sankar, F. C. Chou, C. Chamon, and M. El-Batanouny. Electron-Phonon Coupling on the Surface of the Topological Insulator Bi_2Se_3 Determined from Surface-Phonon Dispersion Measurements. *Phys. Rev. Lett.*, 108:185501, May 2012.

[103] Y. H. Wang, D. Hsieh, E. J. Sie, H. Steinberg, D. R. Gardner, Y. S. Lee, P. Jarillo-Herrero, and N. Gedik. Measurement of Intrinsic Dirac Fermion Cooling on the Surface of the Topological Insulator Bi_2Se_3 Using Time-Resolved and Angle-Resolved Photoemission Spectroscopy. *Phys. Rev. Lett.*, 109:127401, Sep 2012.

[104] Z.-H. Pan, A. V. Fedorov, D. Gardner, Y. S. Lee, S. Chu, and T. Valla. Measurement of an Exceptionally Weak Electron-Phonon Coupling on the Surface of the Topological Insulator Bi_2Se_3 Using Angle-Resolved Photoemission Spectroscopy. *Phys. Rev. Lett.*, 108:187001, May 2012.

[105] Dohun Kim, Qiuzi Li, Paul Syers, Nicholas P. Butch, Johnpierre Paglione, S. Das Sarma, and Michael S. Fuhrer. Intrinsic Electron-Phonon Resistivity of Bi_2Se_3 in the Topological Regime. *Phys. Rev. Lett.*, 109:166801, Oct 2012.

[106] Z.-H. Pan, E. Vescovo, A. V. Fedorov, G. D. Gu, and T. Valla. Persistent coherence and spin polarization of topological surface states on topological insulators. *Phys. Rev. B*, 88:041101, Jul 2013.

[107] Chaoyu Chen, Zhuojin Xie, Ya Feng, Hemian Yi, Aiji Liang, Shaolong He, Daixiang Mou, Junfeng He, Yingying Peng, Xu Liu, et al. Tunable Dirac fermion dynamics in topological insulators. *Scientific reports*, 3(1):1–6, 2013.

[108] Takeshi Kondo, Y. Nakashima, Y. Ota, Y. Ishida, W. Malaeb, K. Okazaki, S. Shin, M. Kriener, Satoshi Sasaki, Kouji Segawa, and Yoichi Ando. Anomalous Dressing of Dirac Fermions in the Topological Surface State of Bi_2Se_3, Bi_2Te_3, and Cu-Doped Bi_2Se_3. *Phys. Rev. Lett.*, 110:217601, May 2013.

[109] A. Crepaldi, F. Cilento, B. Ressel, C. Cacho, J. C. Johannsen, M. Zacchigna, H. Berger, Ph. Bugnon, C. Grazioli, I. C. E. Turcu, E. Springate, K. Kern, M. Grioni, and F. Parmigiani. Evidence of reduced surface electron-phonon scattering in the conduction band of Bi_2Se_3 by nonequilibrium ARPES. *Phys. Rev. B*, 88:121404, Sep 2013.

[110] Colin Howard and M. El-Batanouny. Connecting electron and phonon spectroscopy data to consistently determine quasiparticle-phonon coupling on the surface of topological insulators. *Phys. Rev. B*, 89:075425, Feb 2014.

[111] M. V. Costache, I. Neumann, J. F. Sierra, V. Marinova, M. M. Gospodinov, S. Roche, and S. O. Valenzuela. Fingerprints of Inelastic Transport at the Surface of the Topological Insulator Bi_2Se_3: Role of Electron-Phonon Coupling. *Phys. Rev. Lett.*, 112:086601, Feb 2014.

[112] J. A. Sobota, S.-L. Yang, D. Leuenberger, A. F. Kemper, J. G. Analytis, I. R. Fisher, P. S. Kirchmann, T. P. Devereaux, and Z.-X. Shen. Distinguishing Bulk and Surface Electron-Phonon Coupling in the Topological Insulator Bi_2Se_3 Using Time-Resolved Photoemission Spectroscopy. *Phys. Rev. Lett.*, 113:157401, Oct 2014.

[113] Yuichiro Ando, Takahiro Hamasaki, Takayuki Kurokawa, Kouki Ichiba, Fan Yang, Mario Novak, Satoshi Sasaki, Kouji Segawa, Yoichi Ando, and Masashi Shiraishi. Electrical Detection of the Spin Polarization Due to Charge Flow in the Surface State of the Topological Insulator $Bi_{1.5}Sb_{0.5}Te_{1.7}Se_{1.3}$. *Nano Letters*, 14(11):6226–6230, Oct 2014.

[114] Yuri D. Glinka, Sercan Babakiray, Trent A. Johnson, Mikel B. Holcomb, and David Lederman. Acoustic phonon dynamics in thin-films of the topological insulator Bi_2Se_3. *Journal of Applied Physics*, 117(16):165703, 2015.

[115] Anton Tamtögl, Patrick Kraus, Nadav Avidor, Martin Bremholm, Ellen M. J. Hedegaard, Bo B. Iversen, Marco Bianchi, Philip Hofmann, John Ellis, William Allison, Giorgio Benedek, and Wolfgang E. Ernst. Electron-phonon coupling and surface Debye temperature of $Bi_2Te_3(111)$ from helium atom scattering. *Phys. Rev. B*, 95:195401, May 2017.

[116] Xun Jia, Shuyuan Zhang, Raman Sankar, Fang-Cheng Chou, Weihua Wang, K. Kempa, E. W. Plummer, Jiandi Zhang, Xuetao Zhu, and Jiandong Guo. Anomalous Acoustic Plasmon Mode from Topologically Protected States. *Phys. Rev. Lett.*, 119:136805, Sep 2017.

[117] M Wiesner, A Trzaskowska, B Mroz, S Charpentier, S Wang, Y Song, F Lombardi, P Lucignano, G Benedek, D Campi, et al. The electron-phonon interaction at deep Bi_2 Te_3-semiconductor interfaces from Brillouin light scattering. *Scientific reports*, 7(1):1–12, 2017.

[118] J. Dufouleur, L. Veyrat, A. Teichgräber, S. Neuhaus, C. Nowka, S. Hampel, J. Cayssol, J. Schumann, B. Eichler, O. G. Schmidt, B. Büchner, and R. Giraud. Quasiballistic Transport of Dirac Fermions in a Bi_2Se_3 Nanowire. *Phys. Rev. Lett.*, 110:186806, Apr 2013.

[119] Seung Sae Hong, Yi Zhang, Judy J Cha, Xiao-Liang Qi, and Yi Cui. One-dimensional helical transport in topological insulator nanowire interferometers. *Nano letters*, 14(5):2815–2821, 2014.

[120] Sungjae Cho, Brian Dellabetta, Ruidan Zhong, John Schneeloch, Tiansheng Liu, Genda Gu, Matthew J Gilbert, and Nadya Mason. Aharonov–bohm oscillations in a quasi-ballistic three-dimensional topological insulator nanowire. *Nature communications*, 6(1):1–5, 2015.

[121] Felix Münning, Oliver Breunig, Henry F. Legg, Stefan Roitsch, Dingxun Fan, Matthias Rößler, Achim Rosch, and Yoichi Ando. Quantum confinement of the Dirac surface states in topological-insulator nanowires. *Nature Communications*, 12(1), Feb 2021.

[122] Yoichi Ando. Topological insulator materials. *Journal of the Physical Society of Japan*, 82(10):102001, 2013.

[123] Xiao-Liang Qi, Taylor L. Hughes, and Shou-Cheng Zhang. Topological field theory of time-reversal invariant insulators. *Phys. Rev. B*, 78:195424, Nov 2008.

[124] Yi Zhang, Ying Ran, and Ashvin Vishwanath. Topological insulators in three dimensions from spontaneous symmetry breaking. *Phys. Rev. B*, 79:245331, Jun 2009.

[125] P. M. Ostrovsky, I. V. Gornyi, and A. D. Mirlin. Interaction-Induced Criticality in F_2 Topological Insulators. *Phys. Rev. Lett.*, 105:036803, Jul 2010.

[126] Yi Zhang and Ashvin Vishwanath. Anomalous Aharonov-Bohm Conductance Oscillations from Topological Insulator Surface States. *Phys. Rev. Lett.*, 105:206601, Nov 2010.

[127] Bao-Ling Huang and Massoud Kaviany. Ab initio and molecular dynamics predictions for electron and phonon transport in bismuth telluride. *Phys. Rev. B*, 77:125209, Mar 2008.

[128] J. O. Jenkins, J. A. Rayne, and R. W. Ure. Elastic Moduli and Phonon Properties of bi_2 te_3. *Phys. Rev. B*, 5:3171–3184, Apr 1972.

[129] A.E.H. Love. *A Treatise on the Mathematical Theory of Elasticity*. Dover Books on Engineering Series. Dover Publications, 1944.

[130] L.D. Landau, E.M. Lifshitz, A.M. Kosevich, J.B. Sykes, L.P. Pitaevskii, and W.H. Reid. *Theory of Elasticity: Volume 7*. Course of theoretical physics. Elsevier Science, 1986.

[131] NIST Digital Library of Mathematical Functions. http://dlmf.nist.gov/, Release 1.1.2 of 2021-06-15. F. W. J. Olver, A. B. Olde Daalhuis, D. W. Lozier, B. I. Schneider, R. F. Boisvert, C. W. Clark, B. R. Miller, B. V. Saunders, H. S. Cohl, and M. A. McClain, eds.

[132] L. Pochhammer. Ueber die Fortpflanzungsgeschwindigkeiten kleiner Schwingungen in einem unbegrenzten isotropen Kreiscylinder. 1876(81):324–336, 1876.

[133] C. Chree. The Equations of an Isotropic Elastic Solid in Polar and Cylindrical Co-ordinates their Solution and Application. *Transactions of the Cambridge Philosophical Society*, 14:250, January 1889.

[134] K.F. Graff. *Wave Motion in Elastic Solids*. Dover Books on Physics. Dover Publications, 2012.

[135] Yuri M. Sirenko, K. W. Kim, and Michael A. Stroscio. Near-surface electrons and acoustic phonons: Energy and momentum relaxation. *Phys. Rev. B*, 56:15770–15781, Dec 1997.

[136] A. Svizhenko, A. Balandin, S. Bandyopadhyay, and M. A. Stroscio. Electron interaction with confined acoustic phonons in quantum wires subjected to a magnetic field. *Phys. Rev. B*, 57:4687–4693, Feb 1998.

[137] A. De Martino and R. Egger. Acoustic phonon exchange, attractive interactions, and the Wentzel-Bardeen singularity in single-wall nanotubes. *Phys. Rev. B*, 67:235418, Jun 2003.

[138] Andreas Schulz, Alessandro De Martino, and Reinhold Egger. Spin-orbit coupling and spectral function of interacting electrons in carbon nanotubes. *Phys. Rev. B*, 82:033407, Jul 2010.

[139] S. Vaitiekėnas, G. W. Winkler, B. van Heck, T. Karzig, M.-T. Deng, K. Flensberg, L. I. Glazman, C. Nayak, P. Krogstrup, R. M. Lutchyn, and et al. Flux-induced topological superconductivity in full-shell nanowires. *Science*, 367(6485):eaav3392, Mar 2020.

[140] S. Vaitiekenas, G. W. Winkler, B. van Heck, T. Karzig, M.-T. Deng, K. Flensberg, L. I. Glazman, C. Nayak, P. Krogstrup, R. M. Lutchyn, and C. M. Marcus. Flux-induced topological superconductivity in full-shell nanowires. *Science*, 367(6485), 2020.

[141] J. D. Hunter. Matplotlib: A 2D graphics environment. *Computing in Science & Engineering*, 9(3):90–95, 2007.

[142] I. V. Kurilo, V. P. Alekhin, I. O. Rudyi, S. I. Bulychev, and L. I. Osypyshin. Mechanical Properties of ZnTe, CdTe, CdHgTe and HgTe Crystals from Micromechanical Investigation. *physica status solidi (a)*, 163(1):47–58, 1997.

[143] P. Capper, J. Garland, S. Kasap, and A. Willoughby. *Mercury Cadmium Telluride: Growth, Properties and Applications.* Wiley Series in Materials for Electronic & Optoelectronic Applications. Wiley, 2011.

[144] Anubhav Jain, Shyue Ping Ong, Geoffroy Hautier, Wei Chen, William Davidson Richards, Stephen Dacek, Shreyas Cholia, Dan Gunter, David Skinner, Gerbrand Ceder, and Kristin A. Persson. Commentary: The Materials Project: A materials genome approach to accelerating materials innovation. *APL Materials*, 1(1):011002, 2013.

[145] Johannes Gooth, Bacel Hamdou, August Dorn, Robert Zierold, and Kornelius Nielsch. Resolving the Dirac cone on the surface of Bi_2Te_3 topological insulator nanowires by field-effect measurements. *Applied Physics Letters*, 104(24):243115, 2014.

[146] A. M. Cook, M. M. Vazifeh, and M. Franz. Stability of Majorana fermions in proximity-coupled topological insulator nanowires. *Phys. Rev. B*, 86:155431, Oct 2012.

[147] A. Cook and M. Franz. Majorana fermions in a topological-insulator nanowire proximity-coupled to an s-wave superconductor. *Phys. Rev. B*, 84:201105, Nov 2011.

[148] J. Manousakis, A. Altland, D. Bagrets, R. Egger, and Yoichi Ando. Majorana qubits in a topological insulator nanoribbon architecture. *Phys. Rev. B*, 95:165424, Apr 2017.

[149] Lukasz Fidkowski, Roman M. Lutchyn, Chetan Nayak, and Matthew P. A. Fisher. Majorana zero modes in one-dimensional quantum wires without long-ranged superconducting order. *Phys. Rev. B*, 84:195436, Nov 2011.

[150] Georg Seelig, K. A. Matveev, and A. V. Andreev. Phonon-Induced Resistivity of Electron Liquids in Quantum Wires. *Phys. Rev. Lett.*, 94:066802, Feb 2005.

[151] V. L. Gurevich, V. B. Pevzner, and E. W. Fenton. Reflection of electrons and phonon-assisted Landauer resistance. *Phys. Rev. B*, 51:9465–9475, Apr 1995.

[152] Cheng Zhang, Yi Zhang, Hai-Zhou Lu, XC Xie, and Faxian Xiu. Cycling Fermi arc electrons with Weyl orbits. *Nature Reviews Physics*, pages 1–11, 2021.

[153] NP Ong and Sihang Liang. Experimental signatures of the chiral anomaly in Dirac–Weyl semimetals. *Nature Reviews Physics*, 3(6):394–404, 2021.

[154] B. Z. Spivak and A. V. Andreev. Magnetotransport phenomena related to the chiral anomaly in Weyl semimetals. *Phys. Rev. B*, 93:085107, Feb 2016.

[155] P Baireuther, J Tworzydło, M Breitkreiz, İ Adagideli, and C W J Beenakker. Weyl-Majorana solenoid. *New Journal of Physics*, 19(2):025006, feb 2017.

[156] M. Breitkreiz and P. W. Brouwer. Large Contribution of Fermi Arcs to the Conductivity of Topological Metals. *Phys. Rev. Lett.*, 123:066804, Aug 2019.

[157] E. V. Gorbar, V. A. Miransky, I. A. Shovkovy, and P. O. Sukhachov. Origin of dissipative Fermi arc transport in Weyl semimetals. *Phys. Rev. B*, 93:235127, Jun 2016.

[158] Cai-Zhen Li, An-Qi Wang, Chuan Li, Wen-Zhuang Zheng, Alexander Brinkman, Da-Peng Yu, and Zhi-Min Liao. Topological Transition of Superconductivity in Dirac Semimetal Nanowire Josephson Junctions. *Phys. Rev. Lett.*, 126:027001, Jan 2021.

[159] Janice Ruth Bayogan, Kidong Park, Zhuo Bin Siu, Sung Jin An, Chiu-Chun Tang, Xiao-Xiao Zhang, Man Suk Song, Jeunghee Park, Mansoor B A Jalil, Naoto Nagaosa, Kazuhiko Hirakawa, Christian Schönenberger, Jungpil Seo, and Minkyung Jung. Controllable p–n junctions in three-dimensional Dirac semimetal Cd_3As_2 nanowires. *Nanotechnology*, 31(20):205001, mar 2020.

[160] Li-Xian Wang, Cai-Zhen Li, Da-Peng Yu, and Zhi-Min Liao. Aharonov–Bohm oscillations in Dirac semimetal Cd_3As_2 nanowires. *Nature communications*, 7(1):1–7, 2016.

[161] Ben-Chuan Lin, Shuo Wang, Li-Xian Wang, Cai-Zhen Li, Jin-Guang Li, Dapeng Yu, and Zhi-Min Liao. Gate-tuned Aharonov-Bohm interference of surface states in a quasiballistic Dirac semimetal nanowire. *Phys. Rev. B*, 95:235436, Jun 2017.

[162] Thanh Nguyen, Fei Han, Nina Andrejevic, Ricardo Pablo-Pedro, Anuj Apte, Yoichiro Tsurimaki, Zhiwei Ding, Kunyan Zhang, Ahmet Alatas, Ercan E. Alp, Songxue Chi, Jaime Fernandez-Baca, Masaaki Matsuda, David Alan Tennant, Yang Zhao, Zhijun Xu, Jeffrey W. Lynn, Shengxi Huang, and Mingda Li. Topological Singularity Induced Chiral Kohn Anomaly in a Weyl Semimetal. *Phys. Rev. Lett.*, 124:236401, Jun 2020.

[163] Kunyan Zhang, Xiaoqi Pang, Tong Wang, Fei Han, Shun-Li Shang, Nguyen T. Hung, Ahmad R. T. Nugraha, Zi-Kui Liu, Mingda Li, Riichiro Saito, and Shengxi Huang. Anomalous phonon-mode dependence in polarized Raman spectroscopy of the topological Weyl semimetal TaP. *Phys. Rev. B*, 101:014308, Jan 2020.

[164] Petra Hein, Stephan Jauernik, Hermann Erk, Lexian Yang, Yanpeng Qi, Yan Sun, Claudia Felser, and Michael Bauer. Mode-resolved reciprocal space mapping of electron-phonon interaction in the Weyl semimetal candidate Td-WTe$_2$. *Nature communications*, 11(1):1–8, 2020.

[165] Gavin B. Osterhoudt, Yaxian Wang, Christina A. C. Garcia, Vincent M. Plisson, Johannes Gooth, Claudia Felser, Prineha Narang, and Kenneth S. Burch. Evidence for Dominant Phonon-Electron Scattering in Weyl Semimetal WP$_2$. *Phys. Rev. X*, 11:011017, Jan 2021.

[166] Giacomo Resta, Shu-Ting Pi, Xiangang Wan, and Sergey Y. Savrasov. High surface conductivity of Fermi-arc electrons in Weyl semimetals. *Phys. Rev. B*, 97:085142, Feb 2018.

[167] S. Alexander, Ora Entin-Wohlman, and R. Orbach. Phonon-fracton anharmonic interactions: The thermal conductivity of amorphous materials. *Phys. Rev. B*, 34:2726–2734, Aug 1986.

[168] U. Bockelmann and G. Bastard. Phonon scattering and energy relaxation in two-, one-, and zero-dimensional electron gases. *Phys. Rev. B*, 42:8947–8951, Nov 1990.

[169] A. Y. Shik and L. J. Challis. Electron-phonon energy relaxation in quasi-one-dimensional electron systems in zero and quantizing magnetic fields. *Phys. Rev. B*, 47:2082–2088, Jan 1993.

[170] R. Mickevičius and V. Mitin. Acoustic-phonon scattering in a rectangular quantum wire. *Phys. Rev. B*, 48:17194–17201, Dec 1993.

[171] Igor V. Yurkevich, Alexey Galda, Oleg M. Yevtushenko, and Igor V. Lerner. Duality of Weak and Strong Scatterer in a Luttinger Liquid Coupled to Massless Bosons. *Phys. Rev. Lett.*, 110:136405, Mar 2013.

[172] Luis A Jauregui, Michael T Pettes, Leonid P Rokhinson, Li Shi, and Yong P Chen. Magnetic field-induced helical mode and topological transitions in a topological insulator nanoribbon. *Nature nanotechnology*, 11(4):345–351, 2016.

[173] M. M. Vazifeh and M. Franz. Electromagnetic Response of Weyl Semimetals. *Phys. Rev. Lett.*, 111:027201, Jul 2013.

[174] Ryo Okugawa and Shuichi Murakami. Dispersion of Fermi arcs in Weyl semimetals and their evolutions to Dirac cones. *Phys. Rev. B*, 89:235315, Jun 2014.

[175] Alessandro De Martino, Kathrin Dorn, Francesco Buccheri, and Reinhold Egger. Phonon-induced magnetoresistivity of Weyl semimetal nanowires. arXiv:2110.05149, 2021.

[176] B. J. Ramshaw, K. A. Modic, Arkady Shekhter, Yi Zhang, Eun-Ah Kim, Philip J. W. Moll, Maja D. Bachmann, M. K. Chan, J. B. Betts, F. Balakirev, and et al. Quantum limit transport and destruction of the weyl nodes in taas. *Nature Communications*, 9(1), Jun 2018.

[177] J.B. Seaborn. *Hypergeometric Functions and Their Applications*. Texts in applied mathematics. Springer, 1991.

[178] M. Abramowitz and I. Stegun. *Handbook of Mathematical Functions with Formulas, Graphs, and Mathematical Tables.* Applied mathematics series. Martino Publishing, 2014.

[179] Mikhail Erementchouk and Pinaki Mazumder. Weyl fermions in cylindrical wires. *Phys. Rev. B*, 97:035429, Jan 2018.

[180] E. Noether. Invariante Variationsprobleme. *Nachrichten von der Gesellschaft der Wissenschaften zu Göttingen, Mathematisch-Physikalische Klasse*, 1918:235–257, 1918.

[181] José L. López and Pedro J. Pagola. The confluent hypergeometric functions M(a,b;z) and U(a,b;z) for large b and z. *Journal of Computational and Applied Mathematics*, 233(6):1570–1576, 2010. Special Functions, Information Theory, and Mathematical Physics. Special issue dedicated to Professor Jesus Sanchez Dehesa on the occasion of his 60th birthday.

[182] Ben-Chuan Lin, Shuo Wang, An-Qi Wang, Ying Li, Rong-Rong Li, Ke Xia, Dapeng Yu, and Zhi-Min Liao. Electric Control of Fermi Arc Spin Transport in Individual Topological Semimetal Nanowires. *Phys. Rev. Lett.*, 124:116802, Mar 2020.

[183] Bo Peng, Hao Zhang, Hezhu Shao, Hongliang Lu, David Wei Zhang, and Heyuan Zhu. High thermoelectric performance of Weyl semimetal TaAs. *Nano Energy*, 30:225–234, 2016.

[184] Iraj Abbasian Shojaei, Seyyedesadaf Pournia, Congcong Le, Brenden R. Ortiz, Giriraj Jnawali, Fu-Chun Zhang, Stephen D. Wilson, Howard E. Jackson, and Leigh M. Smith. A Raman probe of phonons and electron–phonon interactions in the Weyl semimetal $\mathrm{NbIrTe_4}$. *Scientific Reports*, 11(1):8155, Apr 2021.

[185] Yuli V. Nazarov and Yaroslav M. Blanter. *Quantum Transport: Introduction to Nanoscience.* Cambridge University Press, 2009.

[186] Yaron Kedem, Emil J. Bergholtz, and Frank Wilczek. Black and white holes at material junctions. *Phys. Rev. Research*, 2:043285, Nov 2020.

[187] Roni Ilan, Adolfo G. Grushin, and Dmitry I. Pikulin. Pseudo-electromagnetic fields in 3D topological semimetals. *Nature Reviews Physics*, 2(1):29–41, Nov 2019.

[188] Andrés Gómez and Luis Urrutia. The Axial Anomaly in Lorentz Violating Theories: Towards the Electromagnetic Response of Weakly Tilted Weyl Semimetals. arXiv:2106.15062, 2021.

Acknowledgements

The first person I would like to thank is my supervisor Prof.Dr.Reinhold Egger, who always supported me throughout my academic time in the institute. I am deeply grateful for his encouragement and that he always has been reachable to answer questions and emails from any place in the world and also during the pandemic. Most of all, I thank him for the possibility to do my PhD with him. Secondly, I thank Prof.Dr.Thomas Heinzel for becoming my second referent and for all the help and advice I received from him during my academic life.

Furthermore, I would like to thank PD Dr.Hermann Kampermann for being my Mentor. My deep gratitude goes to Prof.Dr.Alessandro De Martino, who always answered my mathematical questions with a huge dedication and for all the time we spend calculating in the coffee room. Moreover, I would like thank Prof.Dr. Rodrigo Pereira for the scientific exchange about Weyl semimetals and the cultural exchange about Brazil.

A deep gratitude goes also to Dr.Francesco Buccheri who taught me so many mathematical methods and sent me a stack of references whenever I did not know something. I will miss our discussions about movies. Moreover, I thank Dr.Oleksander Zazunov for the interesting scientific conversations. Especially, I would like to thank Tim Bauer and Samuel Morales for reading my thesis and for the scientific and joyful discussions. Also, I thank Lukas Handt, Kateryna Zatsarynna, Dr. Matthias Gau and Albert Iks for being my office neighbors and the pleasant conversations we had. Furthermore, I thank Claudia Stader and Jens Bremer for helping me organizing the exercise groups and the nice discussions early in the morning. Also, I thank all my friends and colleagues I met during my time at the university.

I would particularly like to thank my parents and my sister for always supporting me and for the freedom they give me to be whatever I want to be. I am glad to have you! Finally, I would like to thank to Michael Janschek for supporting me with all his heart not only during the PhD but also for the last eight years in every situation. I would not have been able to do this without you!

Selbstständigkeitserklärung

Ich versichere an Eides Statt, dass die Dissertation von mir selbständig und ohne unzulässige fremde Hilfe unter Beachtung der „Grundsätze zur Sicherung guter wissenschaftlicher Praxis an der Heinrich-Heine-Universität Düsseldorf“ erstellt worden ist.
Weiterhin erkläre ich, dass ich diese Dissertation keiner anderen Fakultät bereits vorgelegt habe und ich bisher keinerlei erfolglose oder erfolgreiche Promotionsversuche unternommen habe. Darüberhinaus ist mir bekannt, dass jedweder Betrugsversuch zum Nichtbestehen oder Aberkennung der Prüfungsleistung führen kann.

Datum, Ort	Unterschrift